

BIOMEDICAL AND COOLING APPLICATIONS OF MICRO FLOWS

MUHSİNCAN ŞEŞEN

Submitted to the Graduate School of Engineering and Natural Sciences
in partial fulfillment of
the requirements for the degree of
Master of Science

SABANCI UNIVERSITY

BIOMEDICAL AND COOLING APPLICATIONS OF MICRO FLOWS

APPROVED BY:

Dr. Ali Koşar

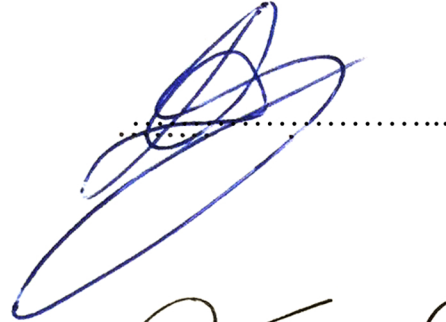


(Thesis Supervisor)

Dr. Serhat Yeşilyurt



Dr. Devrim Gözüaçık



Dr. Kürşat Şendur



Dr. Alpay Taralp



DATE OF APPROVAL: 21/07/2011

© MUHSİNCAN ŞEŞEN 2011

ALL RIGHTS RESERVED

BIOMEDICAL AND COOLING APPLICATIONS OF MICRO FLOWS

Muhsincan Şeşen

Mechatronics Engineering, M.Sc. Thesis, 2011

Thesis Supervisor: Dr. Ali KOŞAR

Keywords: Hydrodynamic cavitation, biomedical treatment, nanostructures, nanofluid, heat sink.

ABSTRACT

Micro flows find applications in a variety of topics covering biomedical, cooling, electronics and MEMS (micro-electro-mechanical-systems) applications. In this work, the destructive effects of hydrodynamic cavitation for biomedical treatment, heat transfer enhancement with nanostructures and nanofluids for small scale cooling applications were investigated.

The research performed in this study includes results from bubbly cavitation experiments and findings showing the destructive effects of bubbly cavitating flow on selected solid specimens, live cells and proteins. Our results showed that cavitation could induce damage both on chalk pieces (and possibly kidney stones) and leukemia/lymphoma cells while the secondary structure content, the hydrodynamic diameter and enzymatic activity of lysozyme were unaffected by cavitation.

For the purpose of making compact and efficient heat exchangers, heat transfer enhancement with nanostructures could be considered as a futuristic candidate. Thus, heat transfer characteristics of nanostructured plates, on which an array of vertical and tilted copper nanorods with an average diameter ranging from 100 to 150 nm and length 500 to 600 nm are integrated to a planar copper thin film coated silicon wafer surface, were compared to planar copper thin film coated silicon wafer surfaces via three different heat transfer techniques (pool boiling, forced convection and jet impingement).

Three different heat sinks were developed for this purpose. Surface temperatures were measured and heat transfer coefficients were calculated for the designed heat sinks and an average of 22% single-phase heat transfer enhancement was realized with the nanostructured plates.

A miniature heat transfer enhancement system is also developed based on the actuation of magnetic nanoparticles dispersed in a base fluid (water). The ferromagnetic particles within the pool were actuated with the magnetic stirrers and this resulted in an average heat transfer enhancement of 37.5% compared to the stationary fluid.

In the light of the performed studies, hydrodynamic cavitation was shown to be a strong heat-free and energy efficient future alternative to ultrasonic cavitation which is being extensively used in biomedical treatment. Also nanostructured surfaces and magnetically actuated nanofluids were proven to contribute to heat transfer enhancement significantly.

MİKRO AKIŞLARIN BİOMEDİKAL VE SOĞUTMA UYGULAMALARI

Muhsincan Şeşen

Mekatronik Mühendisliği, Yüksek Lisans Tezi, 2011

Tez Danışmanı: Dr. Ali KOŞAR

Anahtar Kelimeler: Hidrodinamik kavitasyon, biomedical tedavi, nanoyapılar, nanosıvı, ısı eşanjörü.

ÖZET

Mikro akışlar; biyomedikal, soğutma, elektronik ve mikro-elektro-mekanik-sistemler (MEMS) gibi çeşitli konularda uygulamalara sahiptir. Bu çalışmada; küçük ölçekli soğutma uygulamaları için nanoyapıların ve nanosıvıların ısı transferine katkısı ve biyomedikal tedavi için hidrodinamik kavitasyonun yıkıcı etkileri araştırılmıştır.

Bu araştırma çalışmasında; seçilen katı örnekler, canlı hücreler ve protein üzerinde kabarcıklı kavitasyon akışının yıkıcı etkilerini gösteren deneyler ve bunlara ait bulguların sonuçları verilmiştir. Çalışmanın sonuçları; kavitasyonun tebeşir parçaları (ve muhtemelen böbrek taşları) ve lösemi/lenfoma hücrelerinin hasar görmesine neden olabildiğini göstermiştir ve aynı koşullarda Lizozom'ların ikincil yapı içeriğinin, hidrodinamik çapının ve enzimatik aktivitesinin kabarcıklı kavitasyon tarafından etkilenmemiş olduğunu göstermiştir.

Kompakt ve verimli ısı eşanjörleri yapma amacı için; nanoyapılar ile ısı transferi geliştirme, fütüristik bir aday olarak düşünülebilir. Böylece; çeşitli ısı transfer teknikleri, ısı transferi geliştirmesinde ortalama çapı 100-150 nm ve uzunluğu 500-600 nm olan bakır nanoçubukların bakır ince film kaplamalı silikon yarıiletken levhaya entegre edilmesiyle üretilen nanoyapıların etkilerini karakterize etmek için kullanılmıştır. Üç farklı ısı transferi tekniği (havuzda kaynama, zorunlu konvektif ve jet çarpma) ile elde edilen sonuçlar düz bir silikon taban üzerine biriktirilmiş bakır ince filmlilik plakalar ile karşılaştırılmıştır.

Bu amaç uğruna 3 farklı ısı eşanjörü geliştirilmiştir. Yüzey sıcaklıkları ölçülmüş ve ısı transferi katsayıları hesaplanmıştır. Tek-fazlı deneylerde ortalama %22 ısı transferi iyileştirilmesi elde edilmiştir.

Minyatür bir ısı transferi iyileştirme sistemi daha tasarlanmıştır. Manyetik nanoparçacıkların hareketine dayalı soğutma sistemindeki bu nanoparçacıklar bir baz

sıvı (su) içinde süspansiyon olarak hazırlanmıştır. Havuz içinde ferromanyetik partiküller manyetik karıştırıcı ile harekete geçirilmiştir ve sabit nanosıvı ile karşılaştırılmıştır. Manyetik parçaların hareketlendirilmesiyle ortalama %37.5 ısı transferi iyileştirmesi elde edilmiştir.

Bu çalışmalar sonucunda, hidrodinamik kavitasyonun ileride ultrasonik kavitasyon'a ısı üretimi olmayan ve enerji tasarruflu bir alternatif sunabileceği gösterilmiştir. Ayrıca, nanoyapıların ve manyetik alanla hareketlendirilen nanosıvıların ısı transferini büyük ölçüde iyileştirdiği gösterilmiştir.

ACKNOWLEDGEMENTS

I wish to express my sense of gratitude to Dr. Ali KOŞAR for his boundless guidance and advices during my study, and for the fruitful long discussions we had together with him even during his intensive working hours. I am very lucky to have worked with him.

I would also like to thank our collaborators that have rendered this work possible: Dr. Devrim Gözüaçık, Dr. Özlem Oral, Zeynep Itah, Dr. Alpay Taralp, Dr. Burcu Kaplan Türköz, Anastassia Zakhariouta and Dr. Kürşat Şendur from Sabancı University; Dr. Tansel Karabacak and Wisam Khudhayer from University of Arkansas at Little Rock; Dr. Havva Funda Yağcı Acar from Koç University; Dr. Sinan Ekici from Maltepe University, Dr. Işın Doğan Ekici from Yeditepe University and Dr. M. Pınar Mengüç from Özyeğin University.

I am also grateful to my thesis committee members Dr. Serhat Yeşilyurt, Dr. Alpay Taralp, Dr. Devrim Gözüaçık and Dr. Kürşat Şendur for giving their valuable time commenting on my thesis and their valuable ideas during my study in this university.

I would like to express my thanks to my lab colleagues and lab officers for their superior support and friendship.

This study was supported by Sabancı University Internal Research Grant, IACF09-00642.

Finally, I would like to thank to my family and friends for their love and patience.

TABLE OF CONTENTS

ABSTRACT.....	iv
ÖZET	vi
ACKNOWLEDGEMENTS.....	viii
TABLE OF CONTENTS.....	ix
LIST OF FIGURES	xi
LIST OF TABLES.....	xiii
NOMENCLATURE	xiv
1 INTRODUCTION	1
1.1 Biomedical Application of Hydrodynamic Cavitation	1
1.1.1 Overview on Cavitation Inception.....	1
1.1.2 Theory of Cavitation.....	2
1.1.3 Literature Survey on Cavitation for Cancer Treatment.....	5
1.1.4 Literature Survey on Cavitation Effects on Proteins	7
1.2 Nanostructures for Heat Transfer Enhancement	8
1.2.1 Motivation of Heat Transfer Enhancement with Nanostructures.....	8
1.2.2 Literature Survey on Pool Boiling.....	9
1.2.3 Literature Survey on Forced Convection	10
1.2.4 Literature Survey on Jet Impingement	11
1.3 Nanofluids for Heat Transfer Enhancement	12
1.3.1 Motivation of Heat Transfer Enhancement with Nanofluid.....	12
1.3.2 Literature Survey on Nanofluids	13
2 EXPERIMENTAL.....	14
2.1 Experimental Setup and Procedure for Hydrodynamic Cavitation.....	14
2.1.1 Experimental Setup to Generate Bubbly Cavitation	14
2.1.2 Chalk (Gypsum) As a Model of Kidney Stones.....	16
2.1.3 Cancerous Cell Culture for Cavitation Experiments	17
2.1.4 Cell Death Analysis	17
2.1.5 Protein Sample Preparation	18
2.1.6 Protein CD Measurements.....	18
2.1.7 Protein Dynamic Light Scattering (DLS) Measurements	19
2.1.8 Protein Activity Assays	19
2.1.9 Protein UV Spectroscopy	19
2.1.10 Protein Electrophoresis	20
2.2 Overview on Nanostructured Plates.....	20
2.3 Experimental Setup for Pool Boiling Study.....	23
2.4 Experimental Setup for Forced Convection Study.....	24
2.5 Experimental Setup for Jet Impingement Study	26
2.6 Overview on Nanofluids and Their Preparation Techniques.....	28
2.7 Experimental Setup for Nanofluid Actuation Study	29
2.8 Data Reduction.....	31
2.8.1 Data Reduction of Forced Convection Study.....	31
2.8.2 Data Reduction of Jet Impingement Study.....	32
2.8.3 Data Reduction of Nanofluid Actuation Study	34

2.9	Uncertainty Analyses	34
3	RESULTS AND DISCUSSION	37
3.1	Results and Discussion of Hydrodynamic Cavitation Study	37
3.1.1	Results and Discussion of Chalk Experiments	37
3.1.2	Results and Discussion of Cancerous Cells Experiments	38
3.1.3	Results and Discussion of Protein Experiments	43
3.2	Results and Discussion of Nanostructured Heat Sinks	48
3.2.1	Results and Discussion of Pool Boiling Study	48
3.2.2	Results and Discussion of Forced Convection Study	51
3.2.3	Results and Discussion of Jet Impingement Study	53
3.3	Results and Discussion of Nanofluid Actuation Study	57
4	CONCLUSION	61
4.1	Conclusion of Hydrodynamic Cavitation Study	61
4.1.1	Conclusion of Hydrodynamic Cavitation Application to Chalk and Cancerous Cells	61
4.1.2	Conclusion of Hydrodynamic Cavitation Application to Protein	62
4.2	Conclusions of Nanostructured Heat Sinks	62
4.2.1	Conclusion of Pool Boiling Study	62
4.2.2	Conclusion of Forced Convection Study	63
4.2.3	Conclusion of Jet Impingement Study	63
4.3	Conclusion of Nanofluid Actuation Study	64
	REFERENCES	65

LIST OF FIGURES

Figure 1.1. Cavitation on the tip of a propeller blade [4](a) and cavitation damage [5](b).	1
Figure 1.2. Hydrodynamic Pressure Grade Lines (HGL).	3
Figure 1.3. A typical supercavitating flow pattern [9].	4
Figure 1.4. Microchannel configuration with the orifice throat, inlet and exit area.	5
Figure 2.1. (a) Experimental apparatus. (b) Schematic of exposure of bubbly cavitation.	15
Figure 2.2. Picture of the experimental apparatus.	15
Figure 2.3. A schematic of the glancing angle deposition (GLAD) technique used for the fabrication of vertical and tilted copper nanorod arrays.	21
Figure 2.4. Top and cross-section scanning electron microscopy (SEM) views of (a) flat Cu thin film, (b) vertical GLAD Cu nanorods, and (c) tilted GLAD Cu nanorods.	22
Figure 2.5. Experimental setup for pool boiling.	23
Figure 2.6. Experimental setup for forced convection.	25
Figure 2.7. Cooling device exploded view.	26
Figure 2.8. Experimental setup for jet impingement.	26
Figure 2.9. Cross section view of the heated base showing thermocouple locations. ...	27
Figure 2.10. Experimental setup for nanofluid actuation.	30
Figure 2.11. (a) Pool Boiling Device and Thermocouples (b).	31
Figure 3.1. (a) Penetration depth data [d in μm]. (b) Dependence of material removed from chalk on microprobe to specimen distance and time of exposure [mass in mg]. (c) Erosion on chalk surface after exposure to bubbly cavitation.	38
Figure 3.2. Outlet flow rate versus inlet pressure.	39
Figure 3.3. SEM images of (a) an unexposed chalk surface and (b) an exposed chalk surface after exposure to bubbly cavitation.	39
Figure 3.4. Cell death of Jurkat T cells following exposure to liquid flow without cavitation for indicated durations. Cells were further grown in fresh culture medium. Cell viability was determined by trypan blue exclusion at 0, 16, and 24 h after exposure. Data are shown as mean \pm S.D. (n = 5).	40
Figure 3.5. Cell viability of (a) Jurkat T cells and (b) U-937 cells. Following exposure to bubbly cavitation for indicated durations (cavitation exposure time Cont (0 min), 0.5, 1, 2, 3, and 5 min.), cells were immediately tested [(harvesting time 0 h) or further grown in fresh culture medium for 16 or 24 h (harvesting time 16 or 24 h)]. Cell viability was determined by trypan blue exclusion tests of cells. Data are shown as mean \pm S.D. (n = 5, Student t-test, *P < 0.01).	41
Figure 3.6. Cells were treated (cavitation +) or not (cavitation -) with bubbly cavitation under an inlet pressure of 950 kPa for 5 min. Unexposed control Jurkat [(a) and (c)] and U-937 [(e) and (g)] cells or 5-min cavitation-exposed Jurkat [(b) and (d)] and U-937 [(f) and (h)] cells were harvested immediately (0 h) or after 24 h of culture (24 h). Arrowheads point out to some of the blue and dead cells (scale bars, 100 μm).	42
Figure 3.7. 12% SDS-PAGE analysis of control and hydrodynamically treated lysozyme samples subjected to hydrodynamic flow (a) at a C_i value of 7.6. Lanes: 1: MW markers, arrow indicates 15 kDa band, 2: control, 3-7: 7.5 min-17.5 min treatments sampled at 2.5 min intervals (b) at a C_i value of 0.93. Lanes: 1: MW markers, arrow	

indicates 15 kDa band, 2:control, 3-7: 3 min-7 min treatments sampled at 1 min time intervals. 2.2 µg of protein was loaded to each well	43
Figure 3.8. Secondary structure content of lysozyme subjected to hydrodynamic treatment (a) at a C_i value of 0.93 (b) at a C_i value of 7.6 for the times indicated.	44
Figure 3.9. Average hydrodynamic diameter of lysozyme (a) subjected to hydrodynamic treatment at a C_i value of 0.93 for the times indicated (b) of non-treated control lysozyme samples at concentrations corresponding to samples subjected to hydrodynamic treatment at C_i value of 0.93 for the times indicated (c) subjected to hydrodynamic treatment at a C_i value of 7.6 for the times indicated (d) subjected to hydrodynamic treatment at a C_i value of 7.6 for the times indicated, before and after 30 s ultrasound treatment.	45
Figure 3.10. Relative activity of lysozyme (a) subjected to hydrodynamic treatment at a C_i value of 0.93 for the times indicated (b) subjected to hydrodynamic treatment at a C_i value of 7.6 for the times indicated (c) subjected to hydrodynamic treatment at a C_i value of 7.6, before and after 30 s ultrasound treatment.....	46
Figure 3.11. Superimposed two phase (a) and single phase (b) heat flux plotted against surface temperature for water. Heat transfer coefficient versus heat flux (c) for two phase region.Schematic of heat removal from the system (d).	49
Figure 3.12. Superimposed two phase (a) and single phase (b) heat flux plotted against surface temperature for ethanol. Heat transfer coefficient versus heat flux (c) for two phase region.	50
Figure 3.13. Heat transfer coefficient versus heat flux is plotted with $23 < Re < 30$	51
Figure 3.14. Heat transfer coefficient versus heat flux is plotted with $38 < Re < 46$	51
Figure 3.15. Heat transfer coefficient versus heat flux is plotted with $54 < Re < 62$	52
Figure 3.16. Heat transfer coefficient versus heat flux is plotted with $64 < Re < 76$	52
Figure 3.17. (a) Heat transfer coefficient versus heat flux plotted at a constant volumetric flow rate of 107.5 ml/min and (b) Heat flux versus surface temperature plotted at a constant volumetric flow rate of 107.5 ml/min.	53
Figure 3.18. (a) Heat transfer coefficient versus heat flux plotted at a constant volumetric flow rate of 144.5 ml/min and (b) Heat flux versus surface temperature plotted at a constant volumetric flow rate of 144.5 ml/min.	54
Figure 3.19. (a) Heat transfer coefficient versus heat flux plotted at a constant volumetric flow rate of 181.5 ml/min and (b) Heat flux versus surface temperature plotted at a constant volumetric flow rate of 181.5 ml/min.	55
Figure 3.20. Nusselt number versus heat flux plotted at a constant volumetric flow rate of (a) 107.5 ml/min, (b) 144.5ml/min and (c) 181.5ml/min.	56
Figure 3.21. Heat Flux vs. Surface Temperature.	58
Figure 3.22. Heat Transfer Enhancement Mechanism.	58
Figure 3.23. Heat Transfer Coefficient vs. Heat Flux.	59
Figure 3.24. Heat Transfer Enhancement Ratio.	59

LIST OF TABLES

Table 2.1. Material Properties of Chalk (Gypsum) [124, 155] and Some Common Kidney Stones [122].	16
Table 2.2. Nanofluid properties.	29
Table 2.3. Uncertainties in jet impingement study	35
Table 2.4. Uncertainties in nanofluid actuation study	35
Table 2.5. Uncertainties in pool boiling study	35
Table 2.6. Uncertainties in forced convection study	36

NOMENCLATURE

P_1	Local static pressure at point 1
P_2	Local static pressure at point 2
V_1	Fluid Velocity at point 1
V_2	Fluid Velocity at point 2
P_∞	Pressure at the exit
P_v	Vapor pressure of the fluid
C_i	Cavitation number
R_{max}	Maximum bubble radius
V_{th}	Flow Velocity
q''	Heat flux
P	Power
h	Heat transfer coefficient
T_s	Surface temperature
T_{avg}	Average fluid temperature
T_{exit}	Exit fluid temperature
T_i	Inlet fluid temperature
\dot{m}	Mass flow rate
c_p	Specific heat at constant pressure
Q_{loss}	Thermal and electrical power loss
T_{th}	Thermocouple temperature reading
R_{tot}	Total thermal resistance
Nu	Nusselt Number
N	Number of impinging jets

d_i	Inside diameter
k	Thermal conductivity
u	Fluid velocity
\dot{Q}	Volumetric flow rate
A_c	Cross-sectional area
Re_j	Jet Reynolds number

Greek Symbols

ρ	Density
ν	Kinematic viscosity

1 INTRODUCTION

1.1 Biomedical Application of Hydrodynamic Cavitation

1.1.1 Overview on Cavitation Inception

Hydrodynamic cavitation is a progressive cycle of vaporization, bubble generation, and bubble implosion. This cycle arises in a running liquid as a result of a decrease and consequent increase in local pressure. Hydrodynamic cavitation is initiated with local static pressure reduction below a critical pressure value, the saturated vapor pressure of the liquid in the case of no impurities in the liquid and the surface. Its effects on many types of turbo machinery have been investigated by numerous researchers summarized in standard multiphase flow textbooks [1-3]. It is known that every hydraulic device is susceptible to the damage caused by cavitation once the appropriate cavitating flow conditions occur. In most cases, hydrodynamic cavitation is not desired, since it limits the performance of a fluidic system, causes catastrophic damage and flow choking, generates acoustic noise, and lowers efficiency [1]. Due to its consequences and its destructive nature, cavitation and the energy associated with it constitute an important research subject, especially when these unwanted properties are used for therapeutic applications.

Reynolds was one of the first researchers who focused on the subject of cavitation by trying to explain the unusual behavior of ship propellers, which were vulnerable to damage because of their high rotational speeds (Figure 1.1 [4, 5]). What Reynolds achieved was to explain the phenomenon in terms of the possible creation of

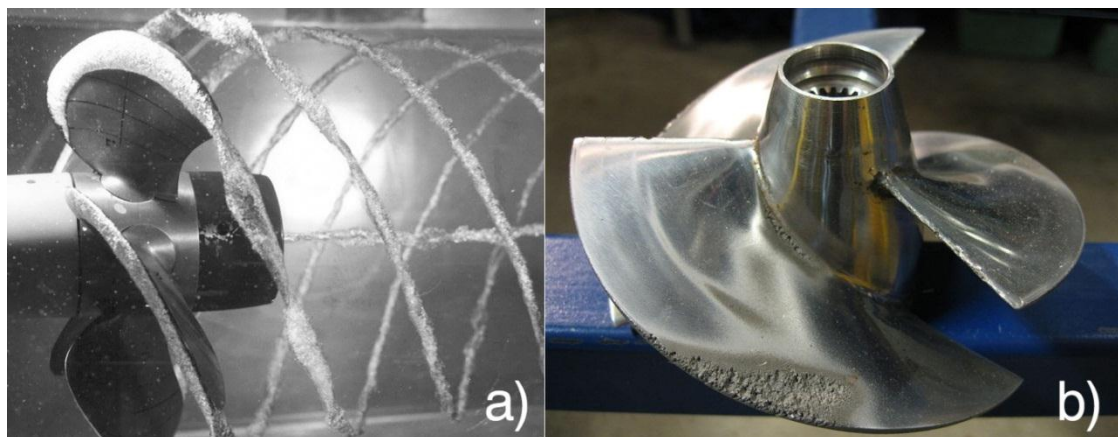


Figure 1.1. Cavitation on the tip of a propeller blade [4](a) and cavitation damage [5](b).

air bubbles near the propeller blades. In general, we understand hydrodynamic cavitation as the phenomenon of formation and growth of vapor or air pockets in fluid flows as a result of local static pressure reduction below a critical value. Cavitation bubbles collapse due to rapid successive reduction and increase in local static pressure and this leads to a high energy outcome, thereby generating highly localized, large amplitude shock waves [1, 2].

1.1.2 Theory of Cavitation

Cavitation generally occurs as a result of vaporization, followed by bubble generation and bubble implosion. Such cavitating flows could be initiated using a successful microchannel and microorifice design. In one configuration used to invoke cavitation, a pressurized liquid is forced past a narrow orifice, which is fixed to the end of a probe lying submerged in a fluid tank [6]. Along the inner surface of the orifice, the sudden decrease in the local static pressure below a critical value initiates bubble formation and cavitation. Upon exiting the micro-orifice and entering a bulk liquid under atmospheric pressure, the bubbles suddenly implode in response to the increase of local pressure.

In contrast to macro scale applications, such as in propellers, a microchannel and microorifice design does not involve any moving parts. However, by using the same concept of reducing the static pressure and then releasing the emerging bubble to a higher pressure medium, it is possible to generate cavitation inside a microorifice. As the fluid passes through the orifice throat, the velocity of the fluid increases due to conservation of mass. As a result, local static pressure of the fluid decreases in consistency with the Bernoulli equation (with the assumption of no frictional losses through the orifice and neglecting frictional losses through the orifice). Bernoulli equation can be given as:

$$\frac{P_1}{\rho} + \frac{1}{2}V_1^2 = \frac{P_2}{\rho} + \frac{1}{2}V_2^2 \quad (1)$$

where P_1 , P_2 and V_1 , V_2 are local static pressures and fluid velocities at before the orifice and inside the orifice, consecutively and ρ is the density of the fluid.

Due to the Bernoulli Equation, the reduction in static pressure leads to an acceleration of the fluid and thus to a significant increase in the fluid velocity between

points 1 and 2 (Figure 1.2). The critical location (point 2) where the static pressure drops to its minimum and the velocity rises to its maximum, is termed the Vena Contracta. Beyond this point, the static pressure recovers downstream of the orifice.

Further reduction of the exit pressure results in the static pressure at the Vena Contracta to fall and produces an increase in the discharge velocity (HGL 2), which is directly proportional to the square root of the pressure difference between points 1 and 2. At some critical pressure in the Vena Contracta, the dissolved gas starts diffusing into the nuclei (submicron bubbles) and promotes their growth. The static pressure could be still above the vapor pressure of the liquid. This bubble growth is associated with the gaseous cavitation.

Further reduction in the exit pressure reduces the static pressure at the Vena Contracta down to the vapor pressure of the liquid (HGL 3). Once this physical limit is reached, any attempt to increase the discharge by reducing the exit pressure is futile [7]. This situation is defined as choked flow or choked cavitation where the exit pressure loses its control over the discharge. The micro-orifice produces its maximum discharge under these conditions, and any reduction in the exit pressure only results in the elongation of the vapor cavity (HGL 4, HGL 5), which is characterized as supercavitating flow.

The cavitation number, C_i , is a dimensionless number used for quantifying

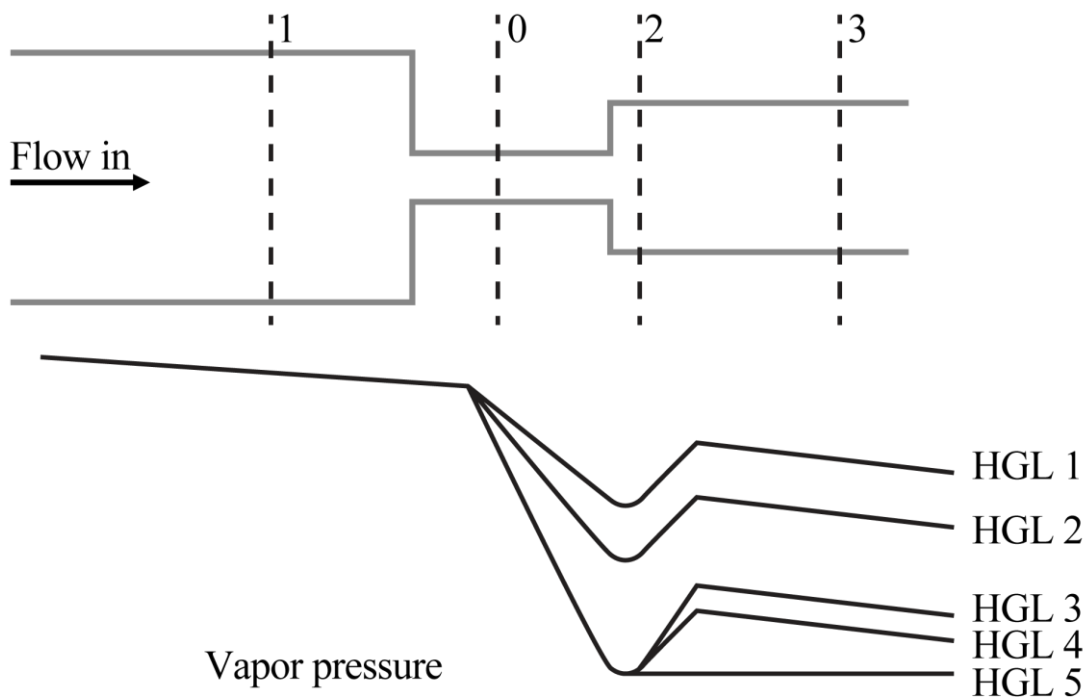


Figure 1.2. Hydrodynamic Pressure Grade Lines (HGL).

similar cavitating conditions and for representing the intensity of cavitation. It can be quantified by the difference between the local static pressure head and vapor pressure head divided by the velocity head. In other words, it is directly proportional to the downstream pressure and inversely proportional to the square of flow velocity near the orifice [8]. The cavitation number is defined as

$$C_i = \frac{P_\infty - P_v}{\frac{1}{2}\rho V^2} \quad (2)$$

where P_∞ is the exit pressure, ρ is the density, P_v is the vapor pressure and V is the flow velocity at the micro-orifice.

A reduction in cavitation number will increase the intensity and the extent of the cavitation. The channel geometry also affects the formation of cavitation. Small cavitation numbers reflect strong cavitation conditions whereas larger numbers specify weakly cavitating and eventually non-cavitating hydrodynamic flow conditions [8]. The cavitation power increases as C_i decreases until a threshold, defined by a minimum C_i value, where a further decrease would prompt the onset of flow choking by bubbles generated inside the channel. It is critical not to reduce the cavitation number too much, since a transition from bubbly cavitation to supercavitation could occur (Figure 1.3 [9]). Supercavitation would be unsuitable for the purpose of the current study, which is to

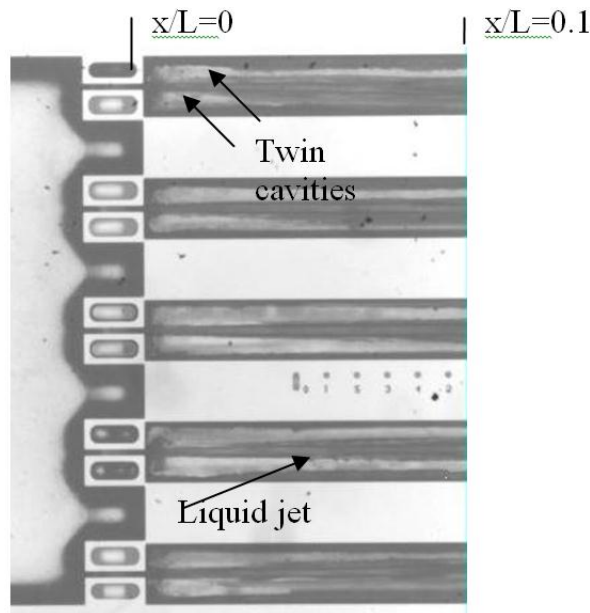


Figure 1.3. A typical supercavitating flow pattern [9].

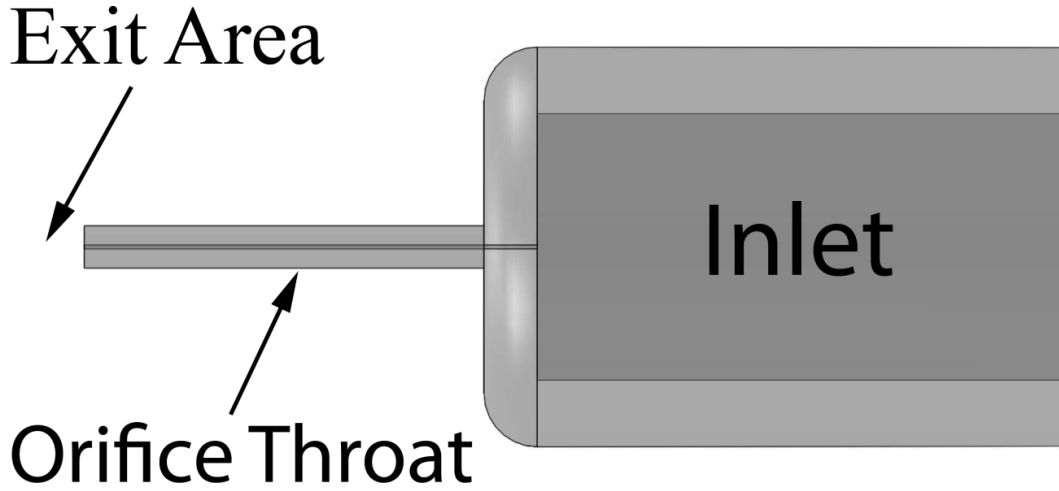


Figure 1.4. Microchannel configuration with the orifice throat, inlet and exit area.

generate continuous bubbly cavitating flow by designing a microfluidic device (bubble generator), and then exposing the emerging bubbles to a small target area and to make observations on the changes in this area.

In Figure 1.4, the microchannel configuration with the short orifice throat and exit area is shown to provide insight into the cavitating system. The bubble implosion caused by hydrodynamic bubbly cavitation is highly destructive on targeted surfaces. Assuming an isobaric bubble collapse, the bubble energy E_b available for each implosion is equal to the work W done by the liquid on the bubble during its collapse, which is obtained by multiplying the pressure head by the initial maximum bubble volume [10]:

$$E_b = W = \frac{4}{3}\pi R_{max}^3(p_\infty - p_v) \quad (3)$$

where P_∞ is the exit pressure, R_{max} is the maximum bubble radius and P_v is the vapor pressure. Thus, if they could be fine controlled, they could be utilized for a variety of treatments, such as destroying kidney stones or killing cancer cells.

1.1.3 Literature Survey on Cavitation for Cancer Treatment

There are two main sources for creating cavitating flow: hydrodynamic and ultrasonic sources. The use of ultrasonic cavitation in treatment of cancerous tissues has been investigated by various researchers [3, 11-14]. As a result, ultrasonic sources have been the most popular means of generating cavitation in laboratory scale studies and,

lately, it has been widely used in clinical practice. Therefore, numerous applications of ultrasonic cavitation (including biomedical applications) do exist [11, 12].

Ultrasonic cavitation is a noninvasive treatment, where some difficulties are faced in targeting the precise location (kidney stone and abnormal tissue) of the treatment. To provide a better targeting, phased array probes are currently being employed [15-22]. A phased array probe consists of many small ultrasonic elements, each of which can be pulsed individually. By varying the timing, a pattern of constructive interference could be obtained so that a beam, which can be steered electronically, could be generated at a set angle. The resulting beam could be directed through the tissue or object being treated. Nevertheless, heat produced by ultrasound is responsible for some of the side effects produced by this treatment. These side effects include local pain, fistula formation, stress urinary incontinence, and erectile dysfunction resulting from various degrees of nerve and tissue damage [23]. Therefore, damage to tissue outside the target area is considered as a major drawback [24]. Moreover, the ultrasound treatment should not be applied over certain body parts, such as eyes and female breasts, and critical locations, such as certain bone fractures and skin wounds [23].

To reduce the side effects, a newly developed ultrasound cavitation therapy method called “histotripsy” was introduced. Histotripsy uses bursts of ultrasound to destroy tissue by cavitation; therefore, microbubbles rather than thermal mechanisms are responsible for its therapeutic effects [25-32].

In addition, ultrasonic cavitation applications have suffered from several shortcomings on industrial-scale applications due to high-frequency ultrasound usage. Research efforts to decrease the threshold of cavitation are present in the literature. The use of microdroplets of various contents [33], xanthene dyes [34], solid nanoparticles [35], bifrequency excitation [36, 37], and the local introduction of shock-wave-generated bubbles [38] are some examples for reducing the threshold of cavitation.

Another ultrasound-based method called lithotripsy (shock wave lithotripsy) is a noninvasive technique, which offers important advantages for the treatment of renal and ureteral stones [39]. It is the most common treatment for solitary, uncomplicated, and small upper urinary tract calculi [40]. Success rate in shock-wave lithotripsy can be increased by providing treatment at a slow shock-wave rate. However, some stone types (e.g., brushite, calcium oxalate monohydrate, and cysteine stones) could be resistant to this treatment [41-44]. Stone breakage with lithotripsy is not always complete and patients are exposed to re-treatment or an additional clinical procedure to remove

residual fragments. Lithotripsy treatment is limited to a maximum stone burden of around 2.5 cm, since renal anatomy could pose a barrier to the clearance of the stone debris [45]. Reports describe unexpected and serious adverse effects of lithotripsy [46-48]. For example, shock-wave treatment can rupture blood vessels, and can cause severe acute renal injury.

Hydrodynamic cavitation is another candidate with a cost-effective and energy-efficient solution [49-51] for biomedical treatment. With the emergence of microfluidics, hydrodynamic cavitation has been considered as an important alternative to ultrasonic cavitation over the last decade. Pioneering studies on hydrodynamic cavitation in microchannels have been successful in showing the unique properties of cavitating flow at the microscale [7,9 52-54]. Bubbles generated by hydrodynamic cavitation are highly destructive on the applied surface; therefore, this technique can be used efficiently as a minimally invasive surgical technique to destroy urinary stones. With an appropriate delivery system such as an endoscopic catheter, bubbles produced by cavitating flow could be targeted to the desired spot precisely so that the destructive nature of bubbly cavitating flows could be used for abnormal tissue ablation (e.g., benign prostate hyperplasia (BPH) or tumor ablation).

In this study, the aim is to explore the feasibility of this alternative treatment method. For this, destructive effects of hydrodynamic cavitation are investigated and checked for controllability and success in the aforementioned targeting, which would confirm its suitability for biomedical treatments.

1.1.4 Literature Survey on Cavitation Effects on Proteins

Hydrodynamic flow processes, specifically hydrodynamic cavitation in micro-orifices, describes a promising alternative to ultrasonic cavitation in the treatment of certain pathological conditions. Unlike ultrasonic cavitation, which is characterized by a relatively large cavitation volume and uniform spatial power distribution, hydrodynamic cavitation permits the honed, local cavitation of a target region at potentially much higher power levels [8]. In view that cavitation can mechanically disrupt hard and soft materials, its prospect as an alternative therapy for kidney stones and prostate diseases is currently being assessed [55].

In assessing its prospect as a therapeutic technique, one disadvantage of hydrodynamic cavitation over traditional sonication-based methods is the obvious

inconvenience brought about by the physically invasive nature of the probe. Other concerns, however, are related to more subtle, adverse consequences that might follow the localized cavitation of tissue at high power levels. The mechanically disruptive effect of hydrodynamic cavitation has been recently established on whole cells [55] but no work has addressed potential risks at the level of cellular components. Hence, the possibility cannot be overlooked that certain environmental factors related to cavitation might prompt protein conformational changes, protein aggregation, and even misfolding as well as potentially dangerous globular-to-fibrous phase transitions [56, 57]. To date, a handful of work related to protein cavitation has reported definite structural and chemical changes in soluble model proteins [58, 59]. However, as these protein investigations were limited to sonication for extended periods, a knowledge base to appreciate the consequences of hydrodynamic cavitation was clearly lacking. It is hoped that this in vitro study might prompt sufficient visibility and effort to assess the impact of hydrodynamic cavitation-based therapies on endogenous proteins. Such insight should prove useful, particularly in light of the regenerative role played by proteins localized at sites of injury or incision.

In this work, the protein model lysozyme was chosen in view of its large knowledge base and ease of characterization [60]. Acetate-buffered solutions at pH 4.8 were subjected to hydrodynamic flow conditions at two C_i values, and aliquots were withdrawn at different times and subjected to analysis.

1.2 Nanostructures for Heat Transfer Enhancement

1.2.1 Motivation of Heat Transfer Enhancement with Nanostructures

With the miniaturization of microprocessors and microchips, an increasing trend in their power density is inevitable. As a result, there is an urgent need for micro heat sinks with low thermal resistance. Besides electronics cooling, micro heat sink technology also finds applications in microreactors, micropropulsion, biotechnology, fuel cells and air conditioning.

In the design processes of many mechanical and chemical devices one of the key issues of saving energies and achieving compact designs is the enhancement of heat transfer [61]. As heat transfer is enhanced, the cooling process becomes more efficient. In the design of heat exchangers for spacecrafts, automobiles, MEMS devices and

micro-processors, it is crucial that the heat exchanger is kept compact and lightweight [62]. For the purpose of making compact and efficient heat exchangers, heat transfer enhancement with nanostructures could be considered as a futuristic candidate.

Recently, nanostructured surfaces have been utilized to achieve high heat transfer performance due to their enhanced heat transfer area and positive effect on heat transfer coefficients with diminishing length scales [63-66]. In order to keep up with the miniaturization process, heat transfer and fluid flow at micro and nano scales have been rigorously studied in the literature to achieve higher heat removal capabilities [67-69]. Moreover, nanostructures also provide additional active nucleate sites so that they could promote nucleate heat transfer in boiling [70].

1.2.2 Literature Survey on Pool Boiling

The applications of nanostructured surfaces in boiling mainly focus on pool boiling. Recent results of pool boiling on nanofluids [66, 71-76] and nanostructured surfaces [70, 77-80] have shown significant heat transfer enhancement compared to plain surface and unseeded liquids, respectively. The investigators working on pool boiling with nanofluids detected nanoparticle coating on their heater surface, which modified the surface characteristics [66, 70-75]. They could visualize the increase in surface roughness with nanoparticle surface coating and the decrease in contact angle (thus the increase in wettability), both of which contributed to enhance critical heat flux (CHF). By this way, researchers were able to obtain high CHF values using pure water on nanoparticle coated surfaces. Significant increases in heat transfer coefficients and the CHF, and dramatic reductions in boiling inception temperatures have been reported by independent research groups dealing with nanostructured surfaces and nanofluids in pool boiling [66, 70-79]. However these studies generally lack a controlled method of nanostructured coating that limits the fundamental understanding of heat-transfer mechanisms in nanoscale as well as applications of such approaches in cooling systems.

With this motivation, a unique method of nanostructured coating for micro-cooling systems is presented, with capability of producing nano-features of various shapes, dimensions and material types. Recently, preliminary tests on a copper nanorod array coated pool boiler were presented and obtained boiling curves were compared to the ones from a conventional planar copper thin film surface configuration [80]. In this work, these studies were extended using two kinds of working fluid, namely water and

ethanol. Convective heat transfer coefficients for both of these fluids having different thermo-physical properties have been calculated and plotted with the input heat flux. The potential use of such a compact nanostructured pool boiler having no pumping and moving components in microscale cooling applications was exploited (up to about 10 W/cm²) and promising results were obtained.

1.2.3 Literature Survey on Forced Convection

Recently, many studies have been going on for enhancing convective heat transfer by enlarging the transfer surface using extended surfaces like fins and ribs [61, 81-83]. These modifications enlarge the heat transfer surface area and provide high heat transfer rates but their drawback is increased friction factor and unwanted pressure drops. Using pin-fin structures causes pressure losses which is a significant problem in many thermo-fluid applications and designs [61]. Such pressure losses occur because of the additional flow resistance imposed by pin-fins.

To achieve positive effects on heat transfer coefficients with diminishing length scale and high heat transfer performance due to enhanced heat transfer area, nanostructured surfaces have been used in more recent studies [63, 70]. The main focus of these studies was utilizing nanostructured surfaces for improving boiling heat transfer. Different from the state of the art, this work utilizes nanostructures in a forced convective heat transfer scheme so that their potential could be exploited from a different perspective.

For this purpose, this article proposes a nanostructured plate, which comprised of vertical copper nanorods of length ~600nm and average diameter ~150nm with an average gap among the nanorods ranging from ~50 to 100nm are integrated to copper thin film (50 nm thick) deposited on silicon substrate with a thickness of 400 μm, to enhance heat transfer via single-phase flow in a rectangular channel. Heat transfer coefficients of the system were reduced for a constant heat flux scenario up to 6.5W/cm² and it has been shown that the nanostructured plate enhances heat transfer significantly because of the large surface area of nanorods available for heat transfer, and thus heat removal takes place more effectively. The advantage of such a system is that it does not cause any significant extra pressure drop and thus does not raise friction factor. Pin-fin geometry imposed by nanorods on the plate (integrated to the channel wall) is on the nanoscale so that the friction forces induce minor pressure losses.

1.2.4 Literature Survey on Jet Impingement

In terms of the capability of providing high heat transfer rates, jet impingement is one of the most efficient cooling mechanisms. Jet impingement cooling not only offers high heat transfer rates but also has the benefit of removing all thermal interface resistances between the surface and the cooling fluid [84]. In a wide range of industrial applications such as annealing of metals [85], cooling of gas turbine blades [86], cooling in grinding processes [87], and cooling of photovoltaic cells [88] jet impingement cooling became a preferential method for the heat transfer community. For instance, in gas turbine applications, this cooling method has been used for a long time in order to assure durability during long operating intervals [85]. Moreover, impingement systems play an important role in micro scale applications such as cooling of electronic components, microprocessors, and MEMS (micro-electro-mechanical-systems) devices [84].

Flow and heat transfer characteristics of multiple impinging jets can differ substantially from those of single jets depending mainly on geometrical conditions. If there are more jets in the array and the individual jet diameter is smaller, the heat transfer rates will be higher [84]. Multiple jet flows interact with each other so that employing jet arrays becomes considerably complex or even erroneous compared to single jet configurations. While heat transfer rates for single jets can be functionally expressed by relatively simple power-functions of Reynolds (Re) and Prandtl (Pr) numbers, correlations for heat transfer rates for multiple jets require the consideration of a number of additional characteristic numbers such as nozzle to surface distance and nozzle spacing [89]. Heat transfer in jet impingement systems is greatly influenced by nozzle geometry. In previous studies reported in the literature, for a constant Reynolds number, it was found that decreasing the jet diameter yields higher stagnation and average heat transfer coefficients [90-92]. This can be attributed to the higher jet velocities created by the smaller nozzles [85].

The thermal properties of two types of nanostructured plates based on vertical and tilted copper nanorods fabricated by glancing angle deposition (GLAD) technique [93-95] were investigated and their effect on the performance of heat removal is compared to that obtained using a plain plate coated with flat Cu thin film. In addition, multiple impinging jets were used instead of a single jet where heat transfer under an impinging

jet is very high in the stagnation zone but decreases quickly away from the jet [84]. Employed multiple jet arrays increase the number of available stagnation zones, and thus, they enhance the heat transfer from the impingement surface. This study reveals the advantages of using nanostructured surfaces and multiple impinging jets in microscale cooling. Moreover, there is little information and studies concerning the heat transfer performance of the nanostructured surfaces with tilted nanorods. It has been reported that nanostructures enhance the heat transfer performance in boiling applications by decreasing the contact angle of the liquid and therefore enhancing wettability [70]. However, there is a lack of knowledge concerning their performances and their configuration effects in jet impingement cooling systems. This study is also meant to display the effect of the orientation of nanostructures (tilted and vertical nanorods) on heat transfer during jet impingement.

1.3 Nanofluids for Heat Transfer Enhancement

1.3.1 Motivation of Heat Transfer Enhancement with Nanofluid

Most of the micro/nano devices tend to shrink in size while the escalation in their power densities becomes inevitable every day. This trend asks for an urgent need for heat transfer enhancement because these devices find applications in many important areas including electronics, microreactors, micropropulsion, biotechnology, fuel cells and air conditioning as well as in new emerging areas such as heat-assisted magnetic recording (HAMR) [96, 97] and the cooling mechanisms required in future thermo photovoltaic cells based on near-field radiative heat transfer principles [98-104].

In order to keep up with the miniaturization process heat transfer and fluid flow at micro and nano scale have been rigorously studied in the literature to achieve higher heat removal capabilities [67-69]. Various researchers have shown that, in general, nanofluids offer better heat transfer characteristics compared to their base fluids [105-107]. One of the reasons for that is the improved thermal conductivity due to existence of high conductivity nanoparticles dispersed in the base fluid. It has also been shown that Brownian diffusion (the random motion of nanoparticles within the base fluid) which results from continuous collision between nanoparticles and the molecules of the base fluid and thermophoresis (diffusion of particles under the effect of a temperature gradient) greatly contribute to heat transfer enhancement in nanofluids [108, 109].

1.3.2 Literature Survey on Nanofluids

Heat transfer experiments have been focused on mainly three techniques; utilization of porous-layer coatings, nanofluids and nanostructures. Heat transfer surfaces have been treated with porous-layer coatings for the enhancement of pool boiling [74, 110] and, recently, nanostructured surfaces have been utilized to achieve high heat transfer performance with enhanced heat transfer area and positive effect on heat transfer coefficients with diminishing length scale [63, 70]. Moreover, nanostructures and porous layer coatings also provide additional active nucleate sites so that they promote nucleate heat transfer in boiling. Similarly, micro-machined structures have also been studied to enhance heat transfer from surfaces in pool boiling [79, 111].

Nanofluids can be considered to be the next-generation heat transfer fluids as they offer exciting new possibilities to enhance heat transfer performance compared to pure liquids [112]. Nanofluids have been used not only since their thermal conductivities are higher compared to their base agents but also the random movement and dispersion effect of the nanoparticles have proven to augment heat transfer significantly [113]. They have usually been used for deposition of nanoparticles on pool surfaces to promote heat transfer by creating roughness and active nucleate sites [72, 73, 75-78, 114]. Different from the state of art, nanofluids containing magnetic nanoparticles are utilized in this study to remove heat from excessive heat generating surfaces. Magnetic nanoparticles are actuated and utilized as heat transporters so that the system could be operated more effectively.

The actuation of nanofluids containing magnetic nanoparticles has recently been investigated in the literature [115-119]. Such fluids were used to design various pumps that do not contaminate the running fluid. Highly controllable nanofluid flows on the order of tens of microliters per second were achieved [115-118]. Motivated by the results in the above mentioned studies, the aim of this paper is to propose a magnetic nanofluid actuation for thermal management applications in microscale. Pioneering experiments were conducted and surface temperatures were obtained from miniature pool containing nanofluid actuated by magnetic stirrers. The potential for such compact pool systems in the use in microscale cooling applications was exploited in this study.

2 EXPERIMENTAL

2.1 Experimental Setup and Procedure for Hydrodynamic Cavitation

2.1.1 Experimental Setup to Generate Bubbly Cavitation

A schematic of the experimental apparatus is shown in Figure 2.1. Sequential images of bubble growth and collapse were captured by a Nikon SMZ 1500 stereoscopic zoom microscope and Unibrain Fire-i 400 CCD camera unit. The volumetric flow rates were measured with a flow meter.

Cavitation is generated by a microorifice, which is a plain microchannel of inner diameter 147 μm , which is suitable for both cavitation inception at moderate inlet pressures and visualization, and is connected to the external tubing. The tubing material is polyether ether ketone, which is an organic polymer thermoplastic used in various engineering and medical applications such as medical implants. The material involves a sheet of protection and has high resistance to corrosion; thus, it can be used in biomedical applications that require sterile environments and equipment. The tubing substrate is precisely laser drilled to the desired inner diameters for the experiments. A representative image of the experiment is depicted in Figure 2.2. The test setup consists of an air compressor, a high pressure tank, a filter, a pressure gauge, tubing, flow meter, and a fine-control valve. The tank was used as a container for deionized (DI) water, and the compressor/nitrogen tank was connected to the tank in order to maintain input pressure. The filter was employed to prevent the flow of any particle larger than 15 μm to the system.

The tests were conducted by applying different inlet pressure values. The maximum pressure applied at the inlet was 10 atm, while the outlet pressure was set constant to 1 atm during tests to better simulate the case for in vivo biomedical applications. The flow rate was controlled with a fine-metering valve. Various inlet pressure values were applied during the tests in order to observe the result at increasing pressure differences until bubbly cavitating flow pattern is obtained. To be reproducible, each experiment was repeated for five times.

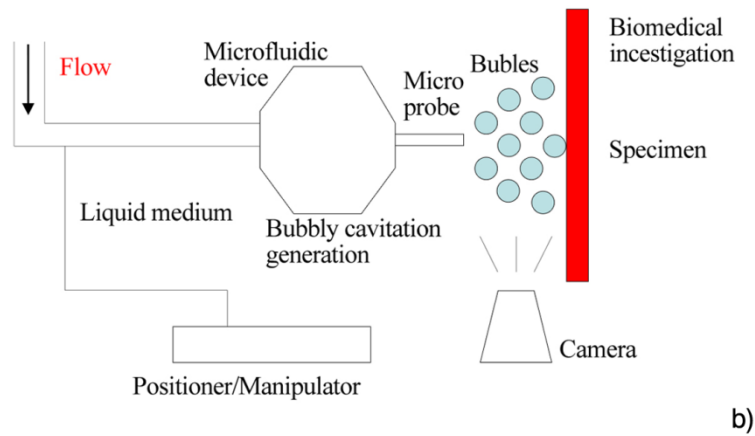
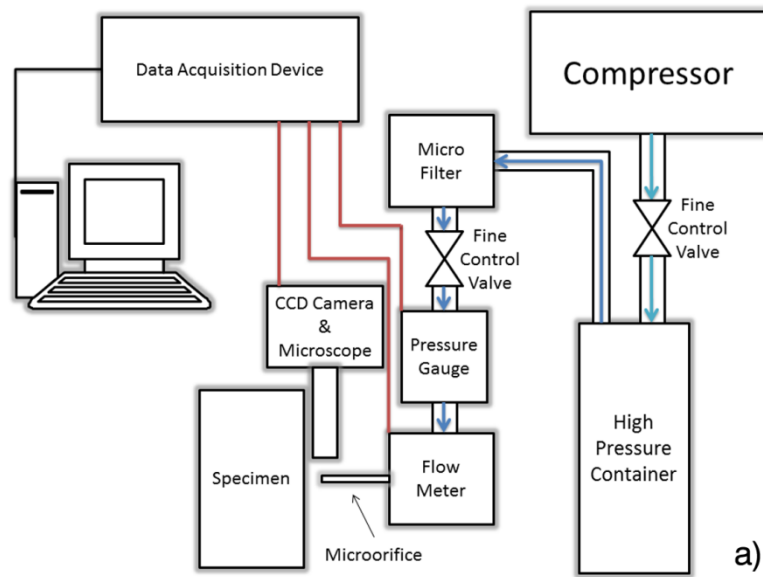


Figure 2.1. (a) Experimental apparatus. (b) Schematic of exposure of bubbly cavitation.



Figure 2.2. Picture of the experimental apparatus.

Examination of bubble sizes in DI water without a specimen resulted in occurrences of bubble diameters of 60–340 μm recorded by the CCD camera (Unibrain Fire-I with a frame rate of 30 f/s) at the exit of the microorifice. The diameters of most of the bubbles were less than 150 μm due to channel diameter, but some bubbles merged at the exit thereby yielding bigger bubbles of diameter greater than 150 μm . The uncertainties in pressure and flow rate measurements were $\pm 0.5\%$ (of entire range) and $\pm 1\%$ (of measured value), while the uncertainty in the inner diameter measurement was $\pm 2 \mu\text{m}$.

2.1.2 Chalk (Gypsum) As a Model of Kidney Stones

To assess a possible use of bubbly cavitation on kidney stones, experiments were conducted. For this purpose, chalk (gypsum) was employed as a material with similar properties to some kidney stones (see Table 2.1). Natural urinary stones are heterogeneous in size, shape, internal structure, mineral composition, material properties, and fragility to treatments [120]. Since natural stones show significant variations with respect to their properties (see Table 2.1), they are rarely used during optimizations aiming at determining the performance of experimental treatments [121]. Instead, some investigators have developed a variety of artificial models or phantom stones to be utilized in renal calculi experiments [122, 123]. Chalk and artificial stones provided important research tools before applying the methods on natural urinary stones

Table 2.1. Material Properties of Chalk (Gypsum) [124, 155] and Some Common Kidney Stones [122].

Properties	Chalk (Gypsum)	Kidney Stones				
Chemical Composition	Calcium sulfate dihydrate	Calcium oxalate monohydrate	Brushite (95% calcium phosphate, 5% calcium oxalate)	Uric Acid	Amino Acid Cysteine	Magnesium ammonium phosphate (90%) Calcium apatite (10%)
Density (g/cm^3)	2.32	2.038	2.157	1.546	1.624	1.587
Young's Modulus (GPa)	10.8	24.51	19.50	9.20	20.07	10.52
Shear Modulus (GPa)	7.47	9.20	7.20	3.30	7.33	4.24
Poisson's Ratio	0.34	0.33	0.36	0.39	0.37	0.24

and usage in the clinics (e.g., lithotripsy or ultrasonic cavitation). Chalk (gypsum and calcium sulfate dihydrate) has been widely used in such investigations by several researchers [124, 125].

The depth of penetration was measured after placing the piece of chalk 1–2 mm downstream just in front of the outlet. All consecutive test runs were made under the same working conditions.

2.1.3 Cancerous Cell Culture for Cavitation Experiments

The same experimental method and apparatus were used to initiate bubbly cavitation for the experiments on cells. Jurkat, acute T-cell leukemia, and myelomonocytic U937 human histiocytic lymphoma cell lines were chosen as cancer models because they grow well in suspension, and they are easy to manipulate.

Jurkat and U937 were obtained from the American-type culture collection. These cells were cultured in RPMI- 1640 medium containing 10% fetal bovine serum, 2-mM L-glutamine, 100- μ g penicillin/100-U streptomycin, 55- μ M β -mercaptoethanol at 37 °C in a humid 5% CO₂–95% air environment. Medium was replaced every 2–3 days.

For the time-dependent treatments, the cells were cultured in 75-cm² flasks and maintained at a cell concentration of 1×10^6 cells/mL. All equipment were sterilized with 70% ethanol and then washed with a sterile physiological solution (phosphate buffered saline, PBS). PBS was used as a liquid environment to produce cavitation. Cells were exposed to bubbly cavitation under an inlet pressure of about 950 kPa (inlet pressure was increased until a cavitating flow pattern was obtained) for 0.5, 1, 2, 3, and 5 min, while the outlet pressure (pressure in the solution) was kept at atmospheric pressure.

2.1.4 Cell Death Analysis

Jurkat and U-937 cells were exposed to hydrodynamically produced bubbly cavitation and then centrifuged at 300 \times g for 5 min, washed and transferred to a fresh culture medium. They were then evaluated for cell death (0 h) or incubated for 16 or 24 h. As a cavitation control, PBS of a comparable flow rate was applied on cells using a larger channel (3 mm diameter) that did not create cavitation. During the experiments, control cells were treated in the same way as their counterparts exposed to cavitation.

Cells were harvested at the indicated time points and death was concomitantly assessed using the trypan blue exclusion technique. Estimation of viability by trypan blue exclusion relies on the loss in membrane integrity (a late event in cell death) that is determined by the uptake of a trypan blue dye to which cells are normally impermeable.

2.1.5 Protein Sample Preparation

Hen Egg-White (HEW) lysozyme (Sigma), 1.5 g, was dissolved in 7.5 mL of buffer A (10 mM sodium acetate, 100 mM KCl, pH 4.8) and centrifuged at 5400 g (15 min, +4 °C).

The supernatant of this solution (6 mL) was subjected to hydrodynamic flow at two C_i values (7.6 versus 0.93) in order to assess, respectively, the potential effects of non-cavitating versus cavitating flow at 25°C. The pressurized fluid exiting the probe orifice was the same composition as buffer A. Samples subjected to hydrodynamic cavitation were withdrawn (2 mL) every minute, whereas samples subjected to non-cavitating hydrodynamic flow were withdrawn (2 mL) every 2.5 minutes. After accumulating a total volume of 50 mL (i.e., corresponding to a 2-minute time point in the former case and a 5-minute time point in the latter case), the content of the tank was decanted. Cavitation was resumed as described above using 6 mL of the decanted solution. The above process was repeated until the effective protein concentration had dropped to approximately 0.4 mg/mL.

Control samples were prepared by appropriately diluting untreated lysozyme solutions in Buffer A. Concentration was determined spectroscopically using the established extinction coefficient of lysozyme ($2.64 \text{ mL mg}^{-1} \text{ cm}^{-1}$) [126].

2.1.6 Protein CD Measurements

Circular Dichroism measurements were performed using a JASCO J-810 model CD Spectropolarimeter (Jasco International, Tokyo, Japan).

Far-UV spectra (200-260 nm) were acquired at 298 K with the instrument configured in continuous scan mode (scan rate 50 nm/min; 3 scans/sample; 2 s response; 1 nm band width; 300 μl samples; 1 mm path length). Data was expressed as ellipticity ($\text{deg cm}^2 \text{ dmol}^{-1}$) on the basis of protein concentration (mg/ml) as well as mean residue ellipticity (MRE) [127]. The far-UV CD spectra were de-convoluted using

CDNN and DICROPROT software in order to determine the percentages of secondary structure elements [128, 129].

2.1.7 Protein Dynamic Light Scattering (DLS) Measurements

Changes of protein hydrodynamic diameter were recorded using a Nano ZS model Malvern Instruments Zetasizer, and quantified using Zetasizer software [130]. Following withdrawal, the protein samples were equilibrated at room temperature and their scattering intensities were quantified at 542 nm. The DLS measurements were compared against non-treated control samples prepared at the same concentration.

2.1.8 Protein Activity Assays

Cell viability measurements were performed in order to identify any correlation between changes of hydrodynamic diameter and bioactivity. *Micrococcus luteus* (ATCC 4698) cells were grown in Trypticase Soy Agar (ATCC Medium 18) medium. This assay is based on the disruption of cell wall peptidoglycans, resulting in lysis of the bacteria and loss of optical density. In a typical assay, hydrodynamically treated as well as control samples were diluted to a concentration of 0.4 mg/ml. For each sample, an aliquot (100 μ l) was transferred to 900 μ l of cell suspension with an optical density of 0.6A (450 nm). Changes of optical density were recorded at each 15-second time interval. The average activity of each sample was calculated by averaging every 15-second measurement acquired over the first 3 minutes. The average activity of samples treated at C_i values of 7.6 and 0.93 were compared against the non-treated control.

2.1.9 Protein UV Spectroscopy

The UV spectra of hydrodynamically treated and control samples were measured using a NanoDrop ND-1000 spectrophotometer. The absorbance measured at 280 nm was used to quantify, whereas the absorbance profile beyond 300 nm was used to rule out the presence of aggregates [131].

2.1.10 Protein Electrophoresis

12% SDS-polyacrylamide gels were prepared according to the method of Laemmli [132]. Samples of equal protein concentration were combined with SDS denaturing/reducing buffer, boiled at 95 °C (3 min), and loaded (10 µl) into the wells. The samples were migrated at a current of 20mA for 70 minutes. The proteins were visualized using Coomassie blue.

2.2 Overview on Nanostructured Plates

GLAD (Glancing Angle Deposition) technique is a self-assembly growth technique that can provide a novel capability for growing 3D nanostructure arrays with interesting material properties such as high electrical/thermal conductivity and also reduced oxidation compared to the polycrystalline films [93-95, 133-135]. It offers a simple, single-step, cost- and time-efficient method to fabricate nanostructured arrays of various elemental materials as well as alloys and oxides. The GLAD technique uses the “shadowing effect” which is a “physical self-assembly” process, through which some of the obliquely incident atoms may not reach certain points on the substrate due to the concurrent growth of parallel structures. Due to the statistical fluctuations in the growth and effect of initial substrate surface roughness, some rods grow faster in the vertical direction. These longer nanorods capture the incident atoms, while the shorter rods get shadowed and cannot grow anymore. This leads to the formation of isolated nanostructures. In addition, nanostructures with different shapes such as vertical tilted, helical, or zigzag geometries can be obtained by introducing a substrate rotation around the surface normal axis. The shadowing effect, and therefore shapes and sizes of nanostructured arrays of GLAD, can be controlled by adjusting the deposition rate, incidence angle, substrate rotation speed, working gas pressure, substrate temperature, and the initial surface topography of the substrate.

The schematic of the custom-made GLAD experimental setup in the present study is shown in Figure 2.3. For the fabrication of vertically aligned and tilted Cu nanorod arrays, the DC magnetron sputter GLAD technique is employed. Cu nanorods were deposited on the native oxide p-Si (100) substrates (2 cm²) coated with a 50 nm thick flat Cu film using a 99.9% pure Cu cathode (diameter about 7.6 cm). The substrates

were mounted on the sample holder located at a distance of about 12 cm from the cathode.

For GLAD growth, the substrate was tilted so that the angle θ between the surface normal of the target and the surface normal of the substrate is 87° . The substrate was attached to a stepper motor and rotated at a speed of 2 rpm for growing vertical nanorods, while the substrate was not rotated for the deposition of tilted nanorods. The depositions were performed under a base pressure of 6.5×10^{-7} Torr, which was achieved by utilizing a turbo-molecular pump backed by a mechanical pump. During Cu deposition experiments, the power was 200 W with an ultrapure Ar working gas pressure of 2.5 mTorr. The deposition time of GLAD Cu nanorods was 60 min. For comparison purposes, conventional smooth Cu thin film samples (i.e. “plain surface” configuration) were also prepared by normal incidence deposition ($\theta = 0^\circ$) with a substrate rotation of 2 rpm. Deposition rate of the vertical nanorods was measured utilizing quartz crystal microbalance (Inficon- Q-pod QCM monitor, crystal: 6 MHz gold coated standard quartz) measurements and cross-sectional scanning electron microscopy (SEM) image analysis to be about 8.6 nm/min. The SEM unit (FESEM-6330F, JEOL Ltd, Tokyo, Japan) was used to study the morphology of the deposited nanorods.

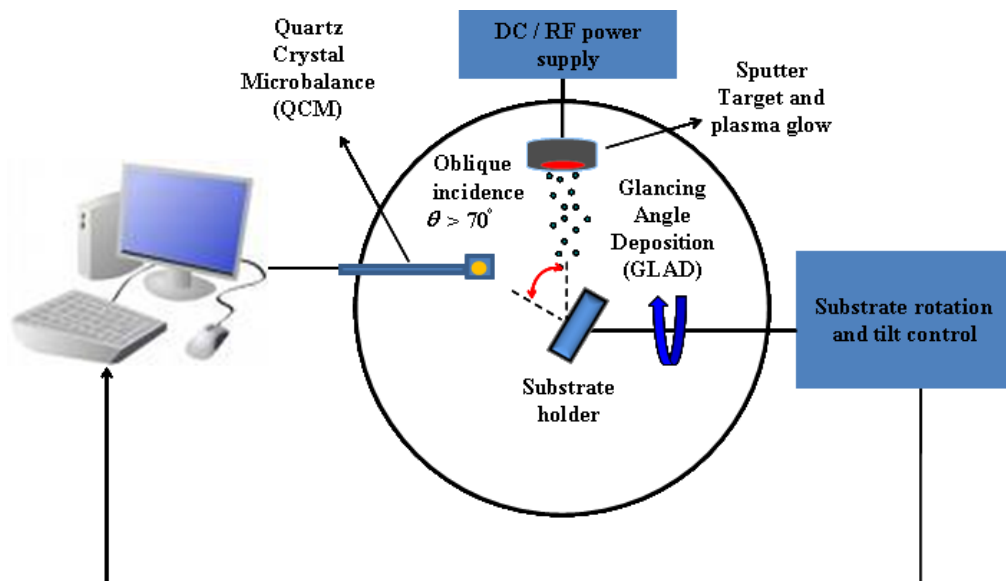


Figure 2.3. A schematic of the glancing angle deposition (GLAD) technique used for the fabrication of vertical and tilted copper nanorod arrays.

The top and side view SEM images of vertical Cu nanorods are shown in Figure 2.4(b) in which an isolated columnar morphology can be seen. However, for the conventional Cu film deposited at normal incidence, its surface was observed to be flat as indicated by the SEM image (Figure 2.4(a)). As can be seen from Figure 2.4(b), the top of the vertical nanorods has a pyramidal shape with four facets, which indicates that an individual nanorod has a single crystal structure. This observation was confirmed by previous studies [136-139] which reported that individual metallic nanorods fabricated by GLAD are typically single crystal. Single crystal rods do not have any interior grain boundaries and have faceted sharp tips. This property will allow reduced surface oxidation, which can greatly increase the thermal conductivity, robustness, and

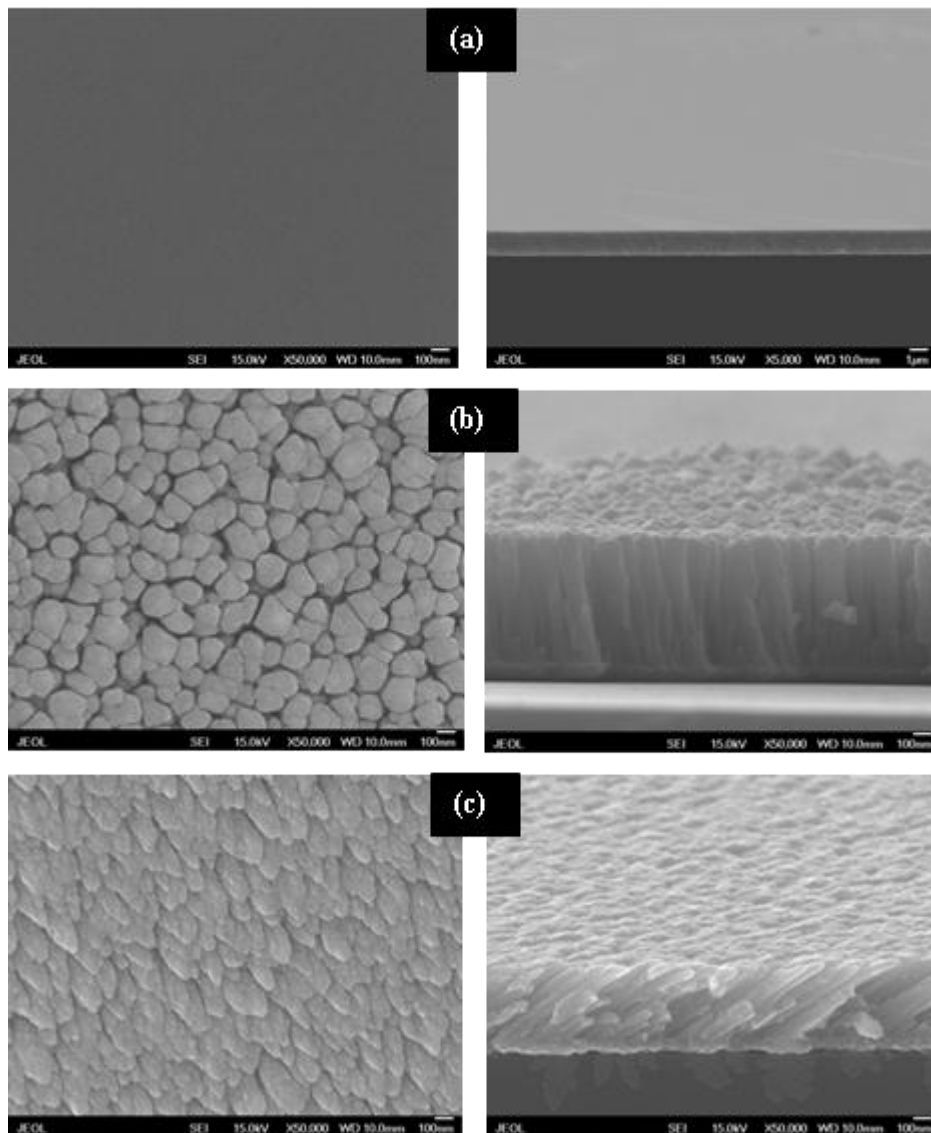


Figure 2.4. Top and cross-section scanning electron microscopy (SEM) views of (a) flat Cu thin film, (b) vertical GLAD Cu nanorods, and (c) tilted GLAD Cu nanorods.

resistance to oxidation-degradation of our nanorods in the present study. The tilted Cu nanorods deposited in the absence of substrate rotation have flat tops tilted towards the flux direction as shown in Figure 2.4(c). In addition, the slanted Cu nanorods also have a faceted top; however, many fibrous structures are present along its sidewalls in contrast to the smooth sides of the vertical Cu nanorods, indicating that the tilted Cu nanorods are not single crystal.

At early stages of GLAD growth, the number density of the nanorods was larger, and the resulting nanorods had diameters as small as about 5-10 nm. As they grew longer and some of them stopped growing, due to the shadowing effect, their diameter grew up to about 100 nm (used in pool boiling and jet impingement studies) and 150nm (used in forced convection study). The average height of the individual rod was measured to be about 600 nm (used in jet impingement and forced convection studies) and 500nm (used in pool boiling study). The average gap among the nanorods also changed with their length from 5-10 nm up to 50-100 and 20-50 nm for vertical and tilted Cu nanorods, respectively, at later stages.

2.3 Experimental Setup for Pool Boiling Study

The experimental setup for the heat transfer characterization is illustrated in Figure 2.5. Aluminum base has air gaps on four sides to enhance heat transfer with minimum loss from the heater placed beneath the aluminum block. A container made of Plexiglas

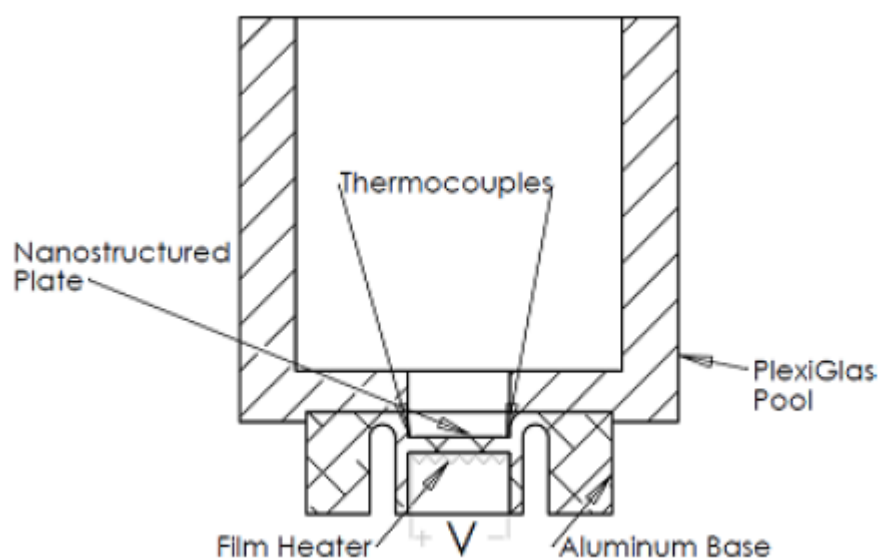


Figure 2.5. Experimental setup for pool boiling.

is closely fitted on top of the aluminum block to create the desired pool for the pool boiling experiments on the nanostructured plate. The heat generated by the film miniature heater is delivered to the nanostructured plate of size $1.7 \text{ cm} \times 1.5 \text{ cm}$ through the base. It provides constant heat flux to the system with constant voltage applied from the electrodes of the film heater. The heat flux values are calculated with the division of the wattage readings from the power supply by the tabulated heater active surface area. Heat losses are obtained from commercial software simulation and were found to be minor compared to electrical power since the system is compact and isolated during experiments. Water/ethanol is filled to the pool separately and all the results are recorded for steady-state surface temperatures. Thermocouples are placed near the nanostructured plate at different places for the accurate measurement of the surface temperature and an almost uniform temperature profile was observed.

After the experimental setup is prepared as explained, the surface temperature readings are recorded as a function of the input voltage and passing current through the heaters by the readings from the power supply. The effective areas of the heaters are tabulated within the manufacturer's guide and their values are extracted from there. These values are used to calculate the constant heat flux input to the system. At certain values of the constant heat flux, steady-state surface temperature values are recorded by the thermocouples until boiling started (referred to as single phase) and during boiling (referred to as two phase). The experiment is conducted first without the nanostructured plate to clearly account for the positive effects of the nanostructured plate.

2.4 Experimental Setup for Forced Convection Study

The experimental setup is demonstrated in Figure 2.6. The cooling device is shown in Figure 2.7. This heat transfer equipment has an aluminum base of dimensions $25\text{mm} \times 60\text{mm} \times 5\text{mm}$. The base is made of aluminum for its high machinability and thermal conductivity. On top of the aluminum base, the nanostructured plate is placed and the top side is sealed with a Plexiglas top which has poor thermal conductivity in order to minimize heat losses. Therefore, the resulting structure could be also regarded as an isolated rectangular channel heated from its lower surface. There is an inlet and an outlet port of the channel drilled into the Plexiglas top from which water could be pressurized. A miniature film-heater is placed underneath the base in order to simulate heat generated by any device like a micro-processor or a MEMS device. The heater is

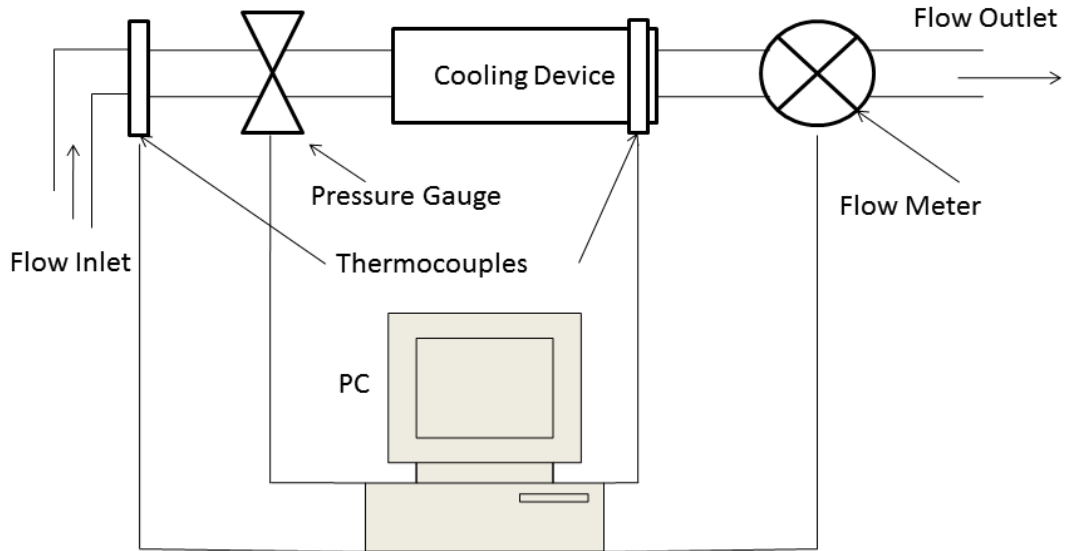


Figure 2.6. Experimental setup for forced convection.

treated with thermal grease and sealed to the base with an Aluminum cap. The whole setup is then sealed to avoid any leakages.

The heat generated by the miniature film-heater is delivered to the nanostructured plate over which water flows in a rectangular channel for cooling. The heater provides constant heat flux to the system since constant voltage is applied from the ends of the film heater. Water is driven through a precisely controlled micro gear pump and surface temperatures are obtained along with constant heat flux applied to the system. Pressure drop across the system is also determined experimentally using a pressure gauge at the inlet and assuming outlet to be atmospheric. Flow rates are deduced using a flow meter integrated to the system. Thermocouples are placed on the surface of the heater and to the inlet for accurate measurement of the fluid and surface temperatures. Experimental data is gathered under steady state conditions and pressure drop, heat flux and surface temperatures are acquired through the data acquisition devices. These data points are then exported to MATLAB and MS Visual Studio for further analysis. Data points for the plain surface configuration and the nanostructured plate configuration are compared in terms of heat transfer coefficients and flow velocities.

After the experimental setup is prepared as explained, the surface and inlet temperatures are measured as a function of the input power data gathered from the readings of the power supply and this operation is carried out for various flow rates. The data collected through the above mentioned procedure is then compared to the setup with nanostructured plate instead of the plain one in order to account for the potential positive effects of the nanostructured plate. The effective areas of the heaters are

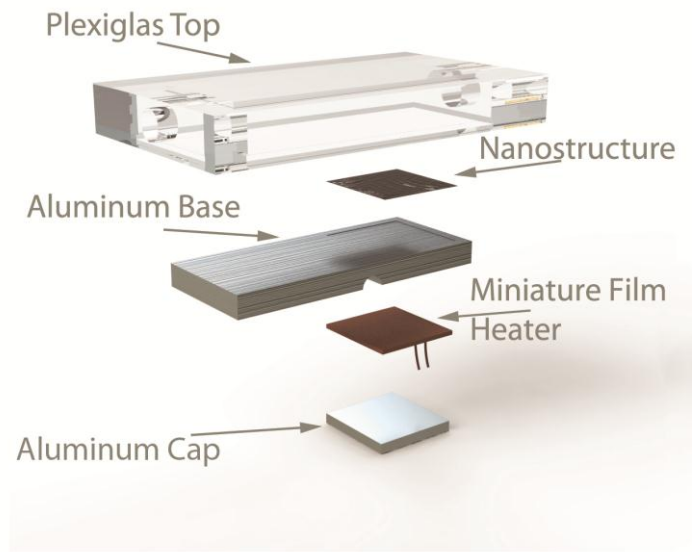


Figure 2.7. Cooling device exploded view.

tabulated in the manufacturer’s guide, from which their values are extracted. These values are used to analytically calculate the constant heat flux input to the system.

2.5 Experimental Setup for Jet Impingement Study

The main components constituting the cooling system are an aluminum base with 4 cartridge heaters, a nanostructured plate placed on top of it, four microchannels

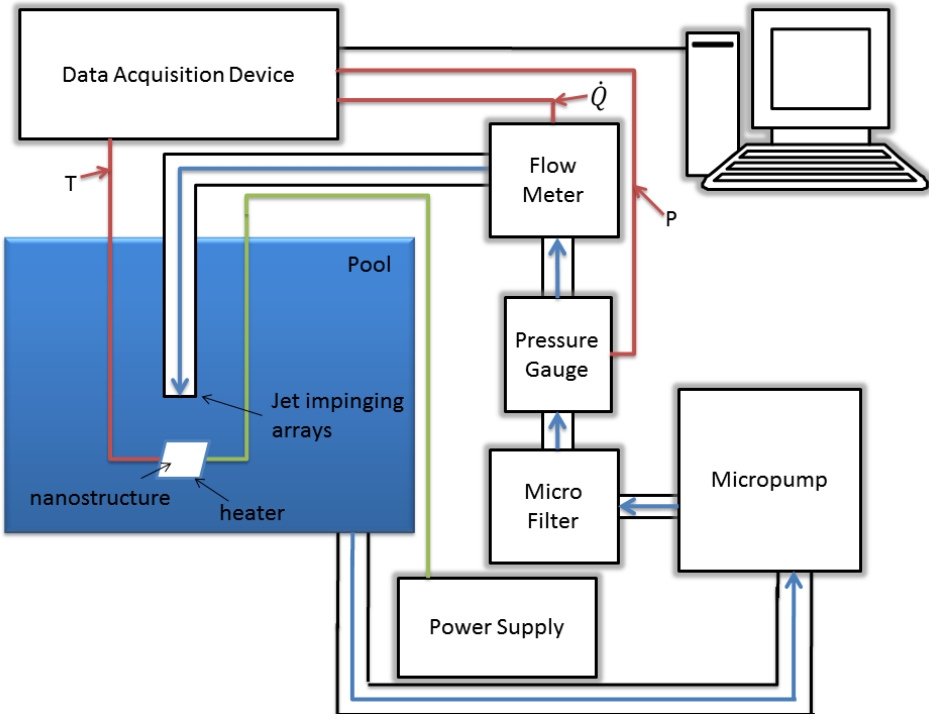


Figure 2.8. Experimental setup for jet impingement.

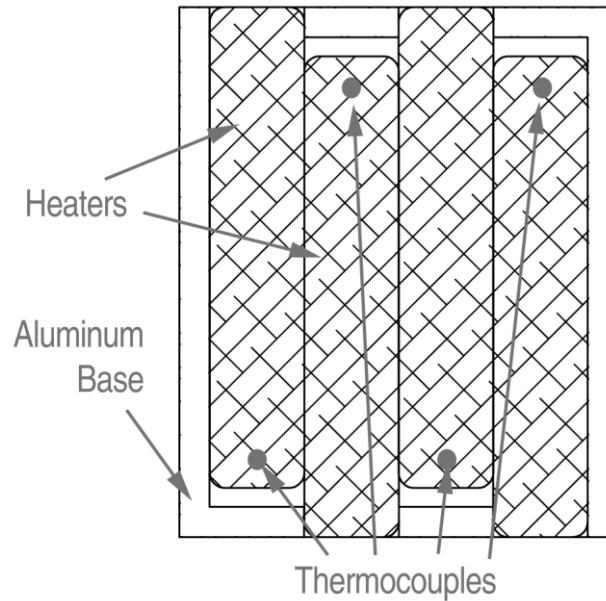


Figure 2.9. Cross section view of the heated base showing thermocouple locations.

generating the impinging jets over the tested samples, and thin (76 μm thick) sensitive thermocouples as shown in Figure 2.8.

The aluminum base of dimensions 35mmx30mmx10mm houses four built-in cartridge heaters of diameter 6.25 mm and of length 31.75 mm which are treated with a high duty thermal grease and sealed to the base with an aluminum cap in order to enhance heat transfer rate and minimize heat losses. Four thermocouples are also treated with high duty thermal grease and attached in the gaps between each cartridge heater and the inner surface of the aluminum base as shown in Figure 2.9. The heaters provide constant heat flux to the system, simulating the heat generated by microchips/microprocessors. The nanostructured copper plates as well as the comparison Cu thin film sample of dimensions 35mmx30mm are placed on the aluminum base. The plate is also treated with high quality thermal grease to improve the efficiency of the cooling process by enhancing the heat transfer rate. The whole setup is carefully sealed to prevent any leakages.

Impinging jets are targeted to the tested surface to remove the unwanted heat away from the plate effectively. The impinging jets are provided by four microchannels of inner diameter 584 μm that are connected to the experimental setup using a CONAX multiple element high pressure sealing and have a distance of 1.5mm to the plate. DI-water is driven into the channels using a HNP Mikrosysteme micro gear pump that can be precisely tuned with a controller allowing the conduction of experiments at different

steady flow rates. Cole Parmer flow meter integrated to the system is used to measure the volumetric flow rate through the jets. To determine the pressure drop across the setup, Omega pressure gauge is attached to the inlet. Four thermocouples placed on the surface of each rod heater are used to acquire accurate steady surface temperature data (Figure 2.9).

Data is gathered through data acquisition system (NI-SCXI 1000). Data acquisition system records 100 data points per second at 100Hz sampling rate. 12000 temperature data points were averaged for each steady state heat flux condition. These data points are then exported through data acquisition software LABVIEW after averaging via MS Visual Studio and MATLAB software once steady state conditions are reached.

After the experimental setup is prepared as explained, the surface temperatures are measured as a function of the input power data gathered from the readings of the power supply. This procedure is carried out at various flow rates, which are adjusted in the inlet region of the setup. In addition to the measurements of flow rates and power values, inlet temperatures, surface temperatures, pressure drops across the system, and electrical currents flowing through the film heater were also measured with the appropriate sensors (Omega thermocouples, Omega pressure transducer, Agilent voltmeter, Cole Parmer flow meter). This procedure is then executed for the samples of vertical and tilted nanostructured plates as well as for the plain surface plate in order to investigate the potential positive effects of the nanostructured plates on heat transfer.

2.6 Overview on Nanofluids and Their Preparation Techniques

Nanofluids are fluids having suspended nanoparticles of nanometer-size and chemistry (metals, oxides, carbides, nitrides, or nanotubes). It is widely known that iron oxide (Fe_3O_4), the dominant magnetic material, magnetite, in magnetic fluid preparations, can be synthesized through the coprecipitation of Fe (II) and Fe (III) salts by the addition of a base [140]. Such nanofluids can be actuated by the application of a magnetic field. The actuation of these ferromagnetic nanoparticles drives its base liquid's molecules along so that a flow is generated. Motivated by this potential, a nanofluid sample was prepared, namely Dodecanoic Acid (DA) coated Super Paramagnetic Iron Oxide (SPIO-DA). To decrease their viscosities and thus facilitate their motion inside the liquid, nanoparticles of SPIO-DA were coated with lauric acid, which also contributes to the long term stability of the nanofluid. The sizes of the

ferromagnetic nanoparticles in the sample SPIO-DA are 23 nm. Table 2.2 shows some properties of the nanofluid used in this study. Dh-I refers to hydrodynamic diameter measured with Dynamic Light Scattering (DLS) using scattered light intensity and Dh-N uses DLS with numerical averaging.

FeCl₂ and FeCl₃ salts (Fe⁺³/Fe⁺² mole fraction) are dissolved in deoxygenated water, then DA is added. The mixture is heated under nitrogen to 85°C and ammonium hydroxide is added to the mixture. Color of the solution turned to brown-black immediately. The formulations are given in Table 1. The mixture is heated for 30 minutes and cooled down to room temperature. Mixture is then placed atop a magnet, which generates a magnetic field of 0.3 T(tesla) and decanted to remove precipitates if any. Excessive coating materials are removed with pure water using ultrafiltration tubes. The entire volume is replaced with pure water three times. Long term stability tests were conducted and the nanofluid has proven to be highly stable for at least 6 months on shelf without precipitation.

2.7 Experimental Setup for Nanofluid Actuation Study

The experimental setup is demonstrated in Figure 2.11. The pool has an outside diameter of 31.8 mm, an inside diameter of 25.8 mm and a height of 12 mm (Figure 2.11). The pool is made of Aluminum for its machinability and high thermal conductivity. A miniature film-heater is placed underneath the pool in order to simulate unwanted heat generated by any device. The heater is treated with high quality thermal grease and sealed to the base with an Aluminum cap through 16 M2.5 bolts. The whole setup is then placed between two magnetic stirrers (Figure 2.10). The magnetic stirrers

Table 2.2. Nanofluid properties.

ID	SPIO-DA
[Fe] (M)	0.175
Si/Fe (mole %)	1.25
Base/Fe (mole %)	1.5
Dh-I (nm)	23-100
Dh-I washed (nm)	23
Dh-N (nm)	32-100
Dh-N washed(nm)	28

have a motor, on which two permanent magnets are placed. One of the magnetic stirrers is powered so that both magnetic stirrers rotate in unison. The magnetic stirrers generate a rotating magnetic field which is intensified at the middle of the pool. The heat generated by the miniature film-heater is delivered to the pool containing the liquid. It provides constant heat flux to the system since constant voltage is applied from the ends of the film heater. The pool is filled with nanofluid and surface temperatures are obtained along with constant heat flux applied to the system. Thermocouples are placed on the surface of the heater and in the bulk fluid at prescribed locations for accurate measurement of the bulk fluid and surface temperatures (Figure 2.11(b)). Data is gathered through data acquisition system (NI-SCXI 1000). Data acquisition system records 100 data points per second at 100Hz sampling rate. These data points are then exported through data acquisition software LABVIEW for further reduction via MS Visual Studio and MATLAB software.

After the experimental setup is prepared as explained, the rise in temperatures is obtained as a function of the input voltage and current data gathered from the readings of the power supply. The effective area of the pool surface and the power input is used to analytically calculate the constant heat flux input to the system. At certain values of the constant heat flux, steady state surface temperatures are recorded by the thermocouples until boiling started. For each constant heat flux, a minimum of 5000 data points have been averaged to account for possible errors. The pool is filled with the nanofluid and two separate experiments are conducted, one with magnetic stirrers on and one with magnetic stirrers off to emphasize on the positive effects of the magnetic stirrer. The magnetic flux densities of the two magnets attached to the motor of the magnetic stirrer are determined using a magnetometer. The magnetic flux densities were

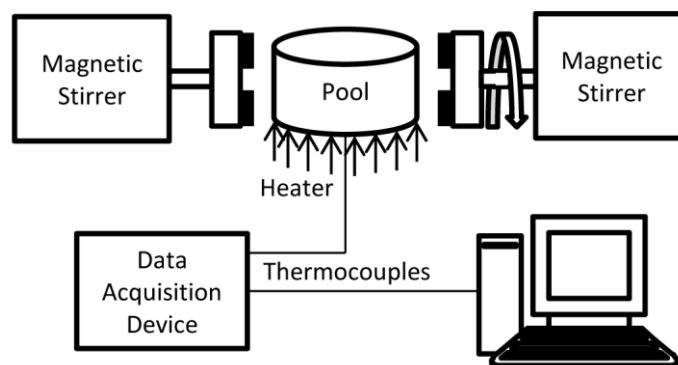


Figure 2.10. Experimental setup for nanofluid actuation.

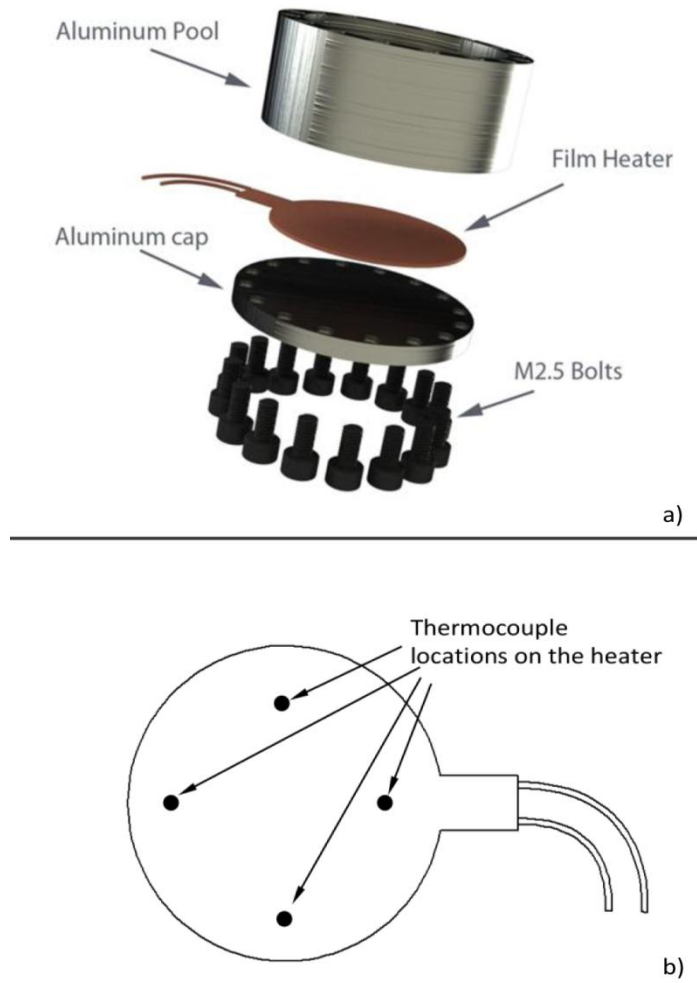


Figure 2.11. (a) Pool Boiling Device and Thermocouples (b).

found to be 116.6 mT on the surface of the magnets and 28.4 mT at the middle of the pool. The magnetic stirrers were rotated at 30 rpm.

2.8 Data Reduction

2.8.1 Data Reduction of Forced Convection Study

Constant heat flux input, q'' , to the system is obtained from

$$q'' = \frac{P - Q_{loss}}{A} \quad (4)$$

where P is the power input (from power supply), Q_{loss} is the electrical and thermal power loss and A is the area of the nanostructured plate. The heat transfer coefficient, h , is then calculated by

$$h = \frac{q''}{T_s - T_{avg}} \quad (5)$$

where T_s is the surface temperature (from thermocouples) and T_{avg} is the average fluid temperature. T_{exit} is determined by

$$T_{exit} = T_i + \frac{P}{\dot{m}c_p} \quad (6)$$

where T_{exit} is the exit fluid temperature, \dot{m} is the mass flow rate of the fluid (from flow meter), T_i is the inlet fluid temperature (from thermocouples) and c_p is the specific heat of water. T_{avg} is extracted from

$$T_{avg} = \frac{T_i + T_{exit}}{2} \quad (7)$$

2.8.2 Data Reduction of Jet Impingement Study

Heat flux provided to the system, q'' , is obtained from

$$q'' = \frac{P - Q_{loss}}{A} \quad (8)$$

where P is the power input (from power supply), Q_{loss} is the thermal and electrical power loss and A is the heated area of the plate. The surface temperatures, T_s , are calculated by considering thermal contact resistances from the thermocouple to the surface of the nanostructured plate.

$$T_s = T_{th} - q'' \cdot R_{tot} \quad (9)$$

where T_{th} is the thermocouple temperature reading and R_{tot} is the total thermal resistance from the thermocouples to the surface of the nanostructured plate (analytical).

The heat transfer coefficient, h , is then calculated by

$$h = \frac{q''}{T_s - T_i} \quad (10)$$

where T_s is the surface temperature and T_i is the inlet fluid temperature. Nusselt number, Nu , is extracted from

$$Nu = \frac{h \cdot N \cdot d_i}{k} \quad (11)$$

where d_i is the inside diameter of each nozzle and N is the number of jets, k is the thermal conductivity of the fluid. The velocity, u , is expressed as

$$u = \frac{\dot{Q}}{A_c} \quad (12)$$

where \dot{Q} is the flow rate of the water (from flow meter) and A_c is the total cross-sectional area of nozzles. Jet Reynolds number, Re_j , is given as

$$Re_j = \frac{u \cdot d_i}{\nu} \quad (13)$$

where ν is the kinematic viscosity of the working fluid.

2.8.3 Data Reduction of Nanofluid Actuation Study

Constant heat flux input, q'' , to the system is obtained from

$$q'' = \frac{P - Q_{loss}}{A} \quad (14)$$

where P is the power input (from power supply), Q_{loss} is the thermal and electrical power loss and A is the effective area of pool surface. The surface temperatures are reduced via considering thermal contact resistances from the thermocouples to the surface of the pool by

$$T_s = T_{th} - q'' \cdot R_{tot} \quad (15)$$

where T_{th} is the averaged thermocouple readings and R_{tot} is the total thermal resistances from the thermocouples to the surface of the pool (analytical). Heat transfer coefficient, h , is extracted from the following expression:

$$h = \frac{q''}{T_s - T_i} \quad (16)$$

where T_i is the ambient temperature.

2.9 Uncertainty Analyses

The uncertainties of the parameters used in all the studies are given in the following tables (Table 2.3, Table 2.4, Table 2.5 and Table 2.6). All measured values are derived from the manufacturer's specification sheet while the uncertainties of the derived parameters are obtained using the propagation of uncertainty method developed by Kline and McClintock [141].

Table 2.3. Uncertainties in jet impingement study

Uncertainty	Error
<i>Power</i>	$\pm 0.15\text{W}$
<i>Nozzle Diameter</i>	$\pm 0.002\text{mm}$
<i>Temperature</i>	$\pm 0.1^\circ\text{C}$
<i>Volumetric Flow Rate</i>	1%
<i>Surface Area</i>	0.09%
<i>Nozzle Area</i>	0.97%
<i>Heat Flux</i>	0.71%
<i>Heat Transfer Coefficient</i>	0.51%
<i>Nusselt Number</i>	0.79%
<i>Flow Velocity</i>	1.39%
<i>Reynolds Number</i>	1.43%

Table 2.5. Uncertainties in nanofluid actuation study

Uncertainty	Error
<i>Thermocouple Reading, T_{th}</i>	$\pm 0.1^\circ\text{C}$
<i>Surface Temperature, T_s</i>	$\pm 0.15^\circ\text{C}$
<i>Power</i>	1%
<i>Area</i>	0.5%
<i>Heat Transfer Coefficient</i>	1.4%

Table 2.4. Uncertainties in pool boiling study

Uncertainty	Error (%)
<i>Resistance</i>	3.12
<i>Power Supply Tracking</i>	0.2
<i>Power Supply Voltage Reading</i>	0.1
<i>Power Supply Current Reading</i>	0.1
<i>Power</i>	0.2032
<i>Thermocouple</i>	$\pm 0.1^\circ\text{C}$

Table 2.6. Uncertainties in forced convection study

Uncertainty	Error (%)
<i>Thermocouple</i>	± 0.27
<i>Power</i>	± 1
<i>Surface Area</i>	± 0.01
<i>Heat Flux</i>	± 0.14
<i>Heat Transfer Coefficient</i>	± 0.52
<i>Flow Rate</i>	± 1

3 RESULTS AND DISCUSSION

3.1 Results and Discussion of Hydrodynamic Cavitation Study

3.1.1 Results and Discussion of Chalk Experiments

During the experiments, in order to measure the penetration effect of cavitation, pieces of chalk were used as specimens. The depths were measured with a microscope after marking the deepest point of the chalk piece without further damaging.

In Figure 3.1(a), the penetration depth is displayed as a function of time. As expected, the penetration in the chalk medium increases with time. It is also evident that the distance between the microprobe and the specimen is an important parameter. The penetration depth is larger for closer distances due to stronger bubble specimen surface interactions. The data for penetration depth were converted to the mass removed by hydrodynamic cavitation assuming the erosion to have a hemispherical shape. This assumption was borne out by observation of the exposed surfaces. The same trends as in Figure 3.1(a) are valid for the dependence of the removed mass on time [see Figure 3.1(b)]. Removal rates of about 40 mg/min and 35 mg/min are achieved for distances of 1 and 2 mm, respectively, between the microprobe and specimen surfaces with a flow rate of 18.2 mL/min.

The flow rate curve with increasing inlet pressure can be seen on Figure 3.2. The flow rate is increased until bubbly cavitating flow conditions are obtained. The cavitation number at cavitation inception was 0.513. The rapid erosion in the specimen's surface proves the effectiveness of the proposed method in kidney stone treatments. A sample of surface erosion caused by bubbly cavitation is shown in Figure 3.1(c). SEM images of unexposed and exposed chalk surfaces are also taken and displayed in Figure 3.3. It could be observed that significant changes on surfaces are present with the exposure of hydrodynamic cavitation. The surfaces become rougher after the exposure to hydrodynamic cavitation [see Figure 3.3(b)] compared to the unexposed surface [see Figure 3.3(a)] as expected. This is due to the interaction between emerging bubbles (from the microprobe) and the chalk surface. As a result, they cause significant erosion and create rough local spots on the surface leading to augmented roughness on chalk surfaces. This finding also implies that the erosion resulting from the exposure to bubbly cavitation is produced by micrometer-size

bubbles rather than the shear effect of the liquid flow. Moreover, the size of the eroded stone debris has been measured, and maximum debris size was found to be 50 μm .

3.1.2 Results and Discussion of Cancerous Cells Experiments

Changes in cell viability and especially induction of apoptosis (a genetically programmed cellular suicide mechanism) have been reported for cancerous human

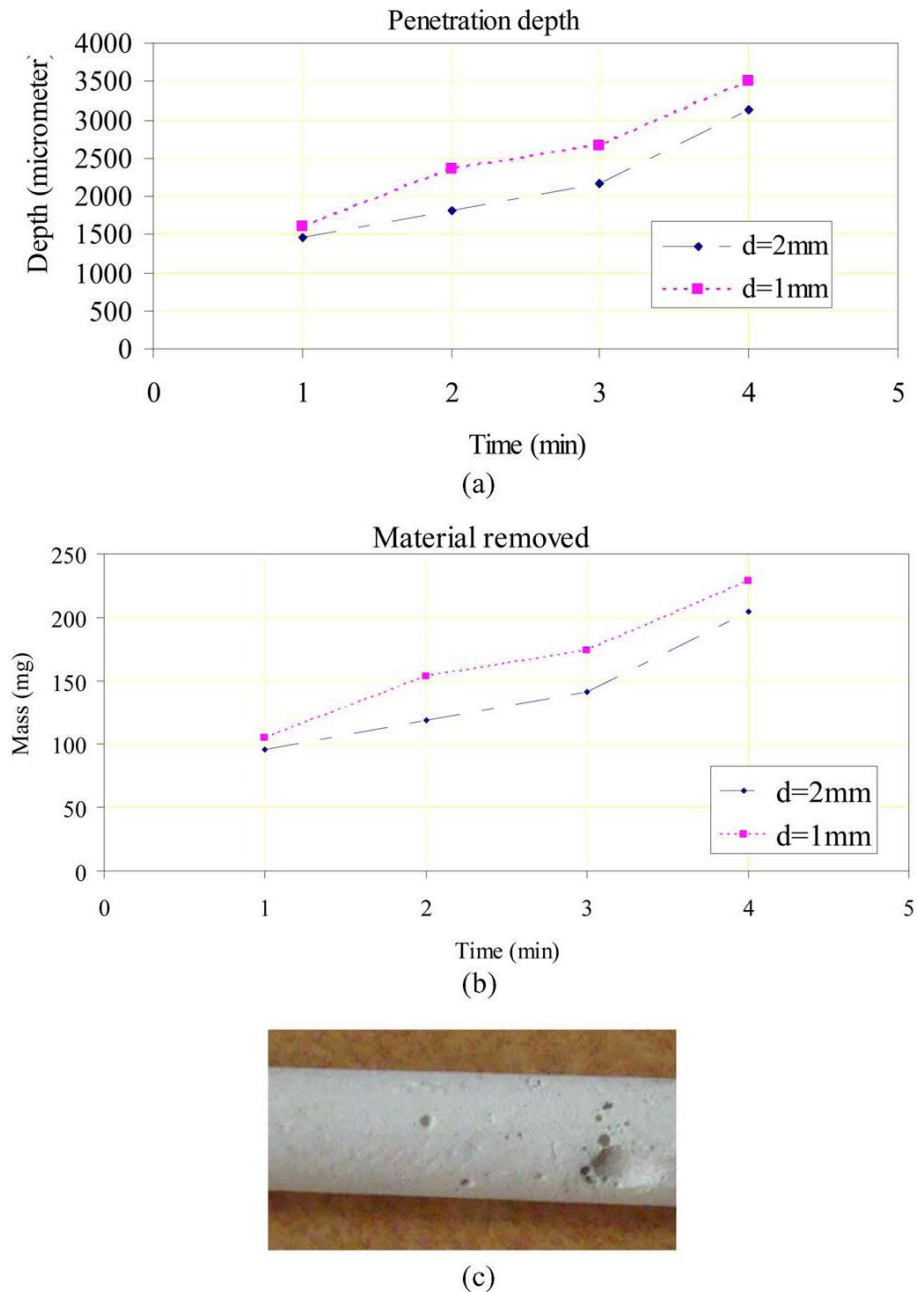


Figure 3.1. (a) Penetration depth data [d in μm]. (b) Dependence of material removed from chalk on microprobe to specimen distance and time of exposure [mass in mg]. (c) Erosion on chalk surface after exposure to bubbly cavitation.

Figure 3.5 and Figure 3.6 show the detrimental effects of bubbly cavitation on cancer cells. Under phase contrast microscope, live cells were observed as white-transparent “balls” [see Figure 3.6(a), (c), (e), and (g)], whereas dead cells are characterized with their blue/dark-blue color due to trypan blue dye uptake [see Figure 3.6(b), (d), (f), and (h)].

When we counted dead cells, we observed that after bubbly cavitation exposure, cancer cells died with two different kinetics: Shortly after exposure, a significant portion of cells lost their membrane integrity, evidenced by trypan blue uptake. The increase in cell death was proportional to the cavitation exposure time (see Figure 3.5, harvesting time 0. Compare cavitation exposure times 0.5, 1, 2, 3, and 5 min). Following 5-min exposure to cavitation, at least half of the Jurkat and U-937 cancer cells were already dead. The late effect on cell survival was evident following 16-h culture of the exposed cells (see Figure 3.5, harvesting time 16 h). At this time point, control cells treated similarly but not exposed to cavitation continued to grow (Cont), but cells that were exposed to cavitation and that had an intact cell membrane at time 0 started to die as well. Cell death was still proportional to the initial cavitation exposure time (see Figure 3.5, harvesting time 16 h, compare cavitation exposure times 0.5, 1, 2,

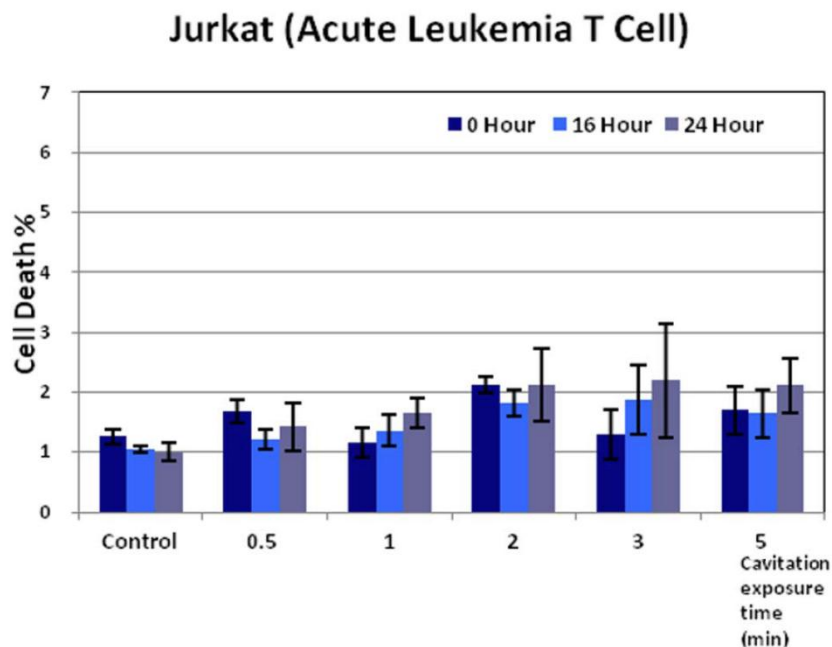


Figure 3.4. Cell death of Jurkat T cells following exposure to liquid flow without cavitation for indicated durations. Cells were further grown in fresh culture medium. Cell viability was determined by trypan blue exclusion at 0, 16, and 24 h after exposure. Data are shown as mean \pm S.D. (n = 5).

3, and 5 min). This late effect was even more prominent after 24 h of culture (see Figure 3.5, harvesting time 24 h). At harvesting time 0 h, 40%–70% and 35%–50% of cells were alive after 3- or 5-min exposure to cavitation, respectively, whereas after 24 h of culture, majority (90%–100%) of cells exposed to 3- or 5-min cavitation were dead (see Figure 3.5, compare harvesting time 0 and 24 h, cavitation exposure times 3 and 5 min). These results showed that the trauma caused by bubbly cavitation on cells might go far beyond an acute damage to cell membrane integrity and be a result of a programmed cell death mechanism (e.g., apoptosis).

A number of stress-inducing environmental factors, including chemicals,

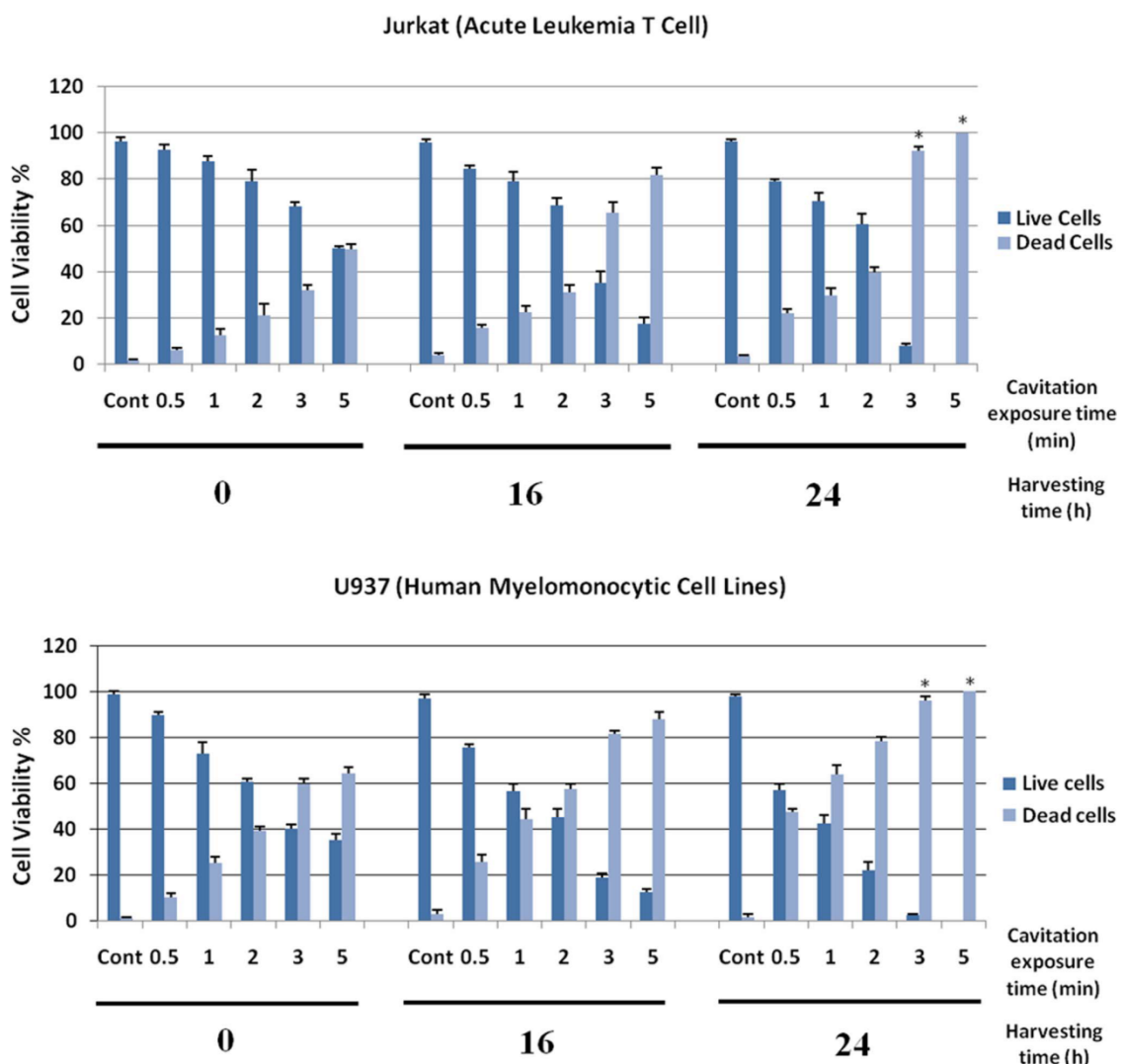


Figure 3.5. Cell viability of (a) Jurkat T cells and (b) U-937 cells. Following exposure to bubbly cavitation for indicated durations (cavitation exposure time Cont (0 min), 0.5, 1, 2, 3, and 5 min.), cells were immediately tested [(harvesting time 0 h) or further grown in fresh culture medium for 16 or 24 h (harvesting time 16 or 24 h)]. Cell viability was determined by trypan blue exclusion tests of cells. Data are shown as mean \pm S.D. (n = 5, Student t-test, *P < 0.01).

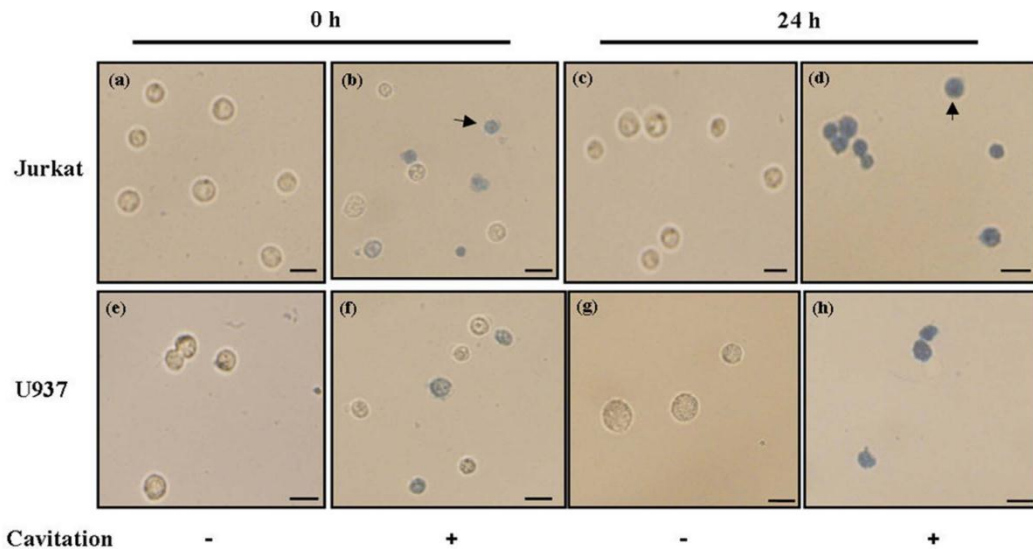


Figure 3.6. Cells were treated (cavitation +) or not (cavitation –) with bubbly cavitation under an inlet pressure of 950 kPa for 5 min. Unexposed control Jurkat [(a) and (c)] and U-937 [(e) and (g)] cells or 5-min cavitation-exposed Jurkat [(b) and (d)] and U-937 [(f) and (h)] cells were harvested immediately (0 h) or after 24 h of culture (24 h). Arrowheads point out to some of the blue and dead cells (scale bars, 100 μ m).

radiation, and changes in the osmotic conditions of the cell, might trigger genetically programmed cell death mechanisms, such as apoptosis. These mechanisms are highly controlled and depend on a cascade of events regulated by various cellular proteins and signaling pathways [143, 144]. Results of our experiments with cells exposed to cavitation strongly suggest that, although the short-term effects of cavitation are reminiscent of an accidental type of cell death called “necrosis,” the late effects might be controlled by a programmed cell death mechanism activated by cavitation forces. Since, tissues are organized structures; a late and programmed cell death wave around the exposed tissue could contribute to the therapeutic effects of bubbly cavitation. Moreover, in live tissues, immune responses generated as a result of the necrosis of cells might affect the final outcome. All these biological effects might be used in favor to increase the therapeutic potential of the proposed method. Therefore, optimization of the time and the strength of cavitation exposure and tests of controlled targeting of the probe should take the early and late effects on cell death and consequent immune responses after cavitation trauma into account.

3.1.3 Results and Discussion of Protein Experiments

Most analyses yielded structural profiles that were virtually identical for lysozyme solutions sampled before and after hydrodynamic treatment. While perhaps unexpected, the observed trend could be construed as having reflected the comparatively higher stability of lysozyme with respect to many other proteins. Of the few structural alterations noted, all were subtle and more importantly, reversible, suggestive of non-covalent changes. The findings differed markedly from literature reports, which documented covalent chemical changes to protein functional groups under the conditions of prolonged acoustic cavitation [58].

The SDS-PAGE molecular weight profile of lysozyme treated at either of the two cavitation numbers (0.93 and 7.6) was identical to the corresponding non-treated controls at every point of the time course (Figure 3.7(a) and (b)). Neither a change of mobility, a reduction of band intensity, a sign of material trapped in the stacking gel, nor any smearing was noted. This finding clearly indicated that peptide bond scission and other potential modes of protein loss were inoperative, despite the localized high temperatures and pressures anticipated by bubble collapse. As well, the UV spectral

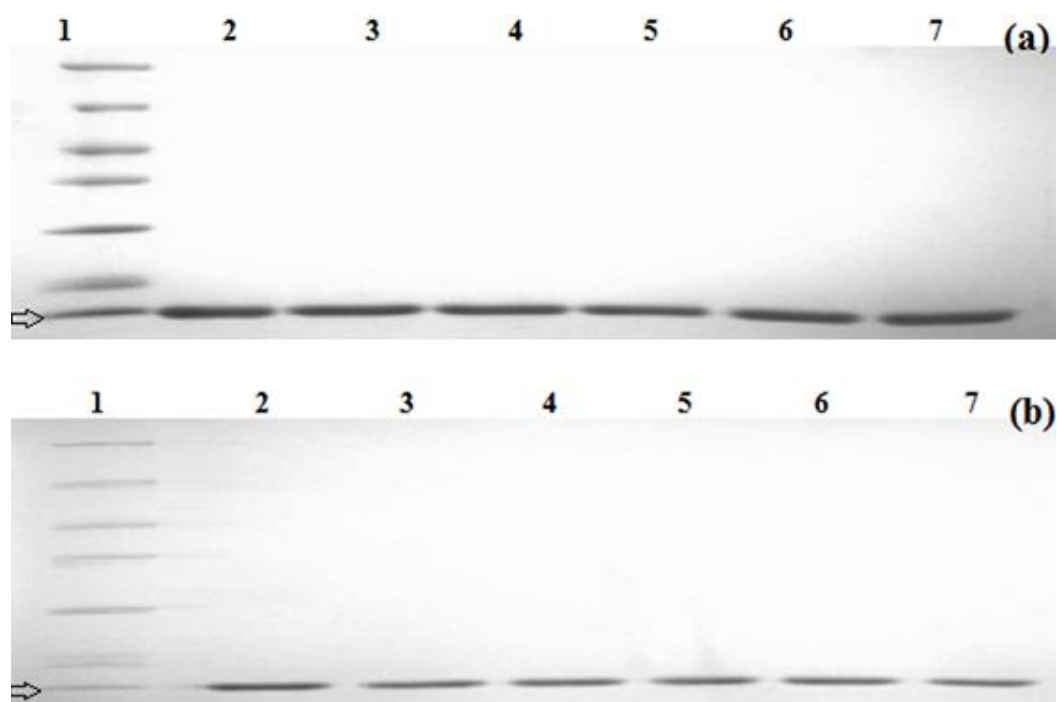


Figure 3.7. 12% SDS-PAGE analysis of control and hydrodynamically treated lysozyme samples subjected to hydrodynamic flow (a) at a C_i value of 7.6. Lanes: 1: MW markers, arrow indicates 15 kDa band, 2: control, 3-7: 7.5 min-17.5 min treatments sampled at 2.5 min intervals (b) at a C_i value of 0.93. Lanes: 1: MW markers, arrow indicates 15 kDa band, 2: control, 3-7: 3 min-7 min treatments sampled at 1 min time intervals. 2.2 μ g of protein was loaded to each well.

profiles of hydrodynamically treated samples and non-treated controls were comparable (results not shown), implying their structural resemblance. Circular dichroism measurements (Figure 3.8(a) and (b)) of lysozyme samples treated at C_i values of 0.93 or 7.6 yielded composite alpha helix and beta sheet structural profiles entirely consistent with the native form of lysozyme. Any observable spectral variations were statistically insignificant. Dynamic light scattering measurements (Figure 3.9(a) and (b)) of protein treated at a C_i value of 0.93 showed no statistically significant variation of

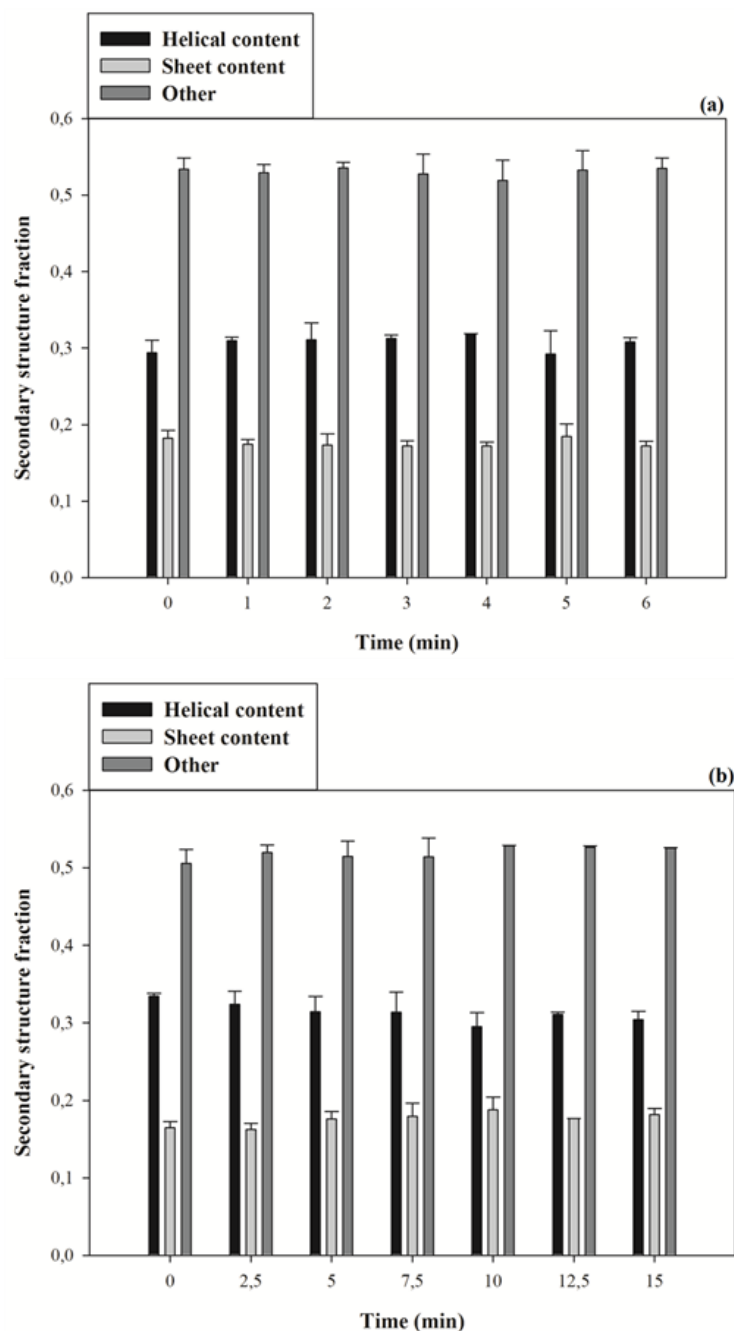


Figure 3.8. Secondary structure content of lysozyme subjected to hydrodynamic treatment (a) at a C_i value of 0.93 (b) at a C_i value of 7.6 for the times indicated.

hydrodynamic diameter over the entire time course of flow treatment. Moreover, samples subjected to this treatment showed no statistically significant digression in bioactivity (Figure 3.10(a)), confirming the integrity of all essential structural elements.

In contrast to the results obtained with C_i equal to 0.93, a decrease of hydrodynamic diameter at a C_i value of 7.6 was noted by dynamic light scattering (Figure 3.9 (c)). This decrease was discernible after 10 minutes (3.6 nm) and readily notable (3.16nm) after 15 minutes of flow treatment. All control samples retained the original hydrodynamic diameter of 3.8 nm. Thermally-induced reversible changes of hydrodynamic diameter and conformation have been previously documented in lysozyme using light scattering [145, 146] and solution X-ray scattering [147]. The bioassay of lysozyme (Figure 3.10(b)) also supported the light scattering results in the sense that the activity of lysozyme had dropped by a statistically significant amount after 15 minutes of flow treatment at a C_i value of 7.6. Most notable, however, was the response of cavitated lysozyme towards ultrasonication. Ultrasonication was applied in

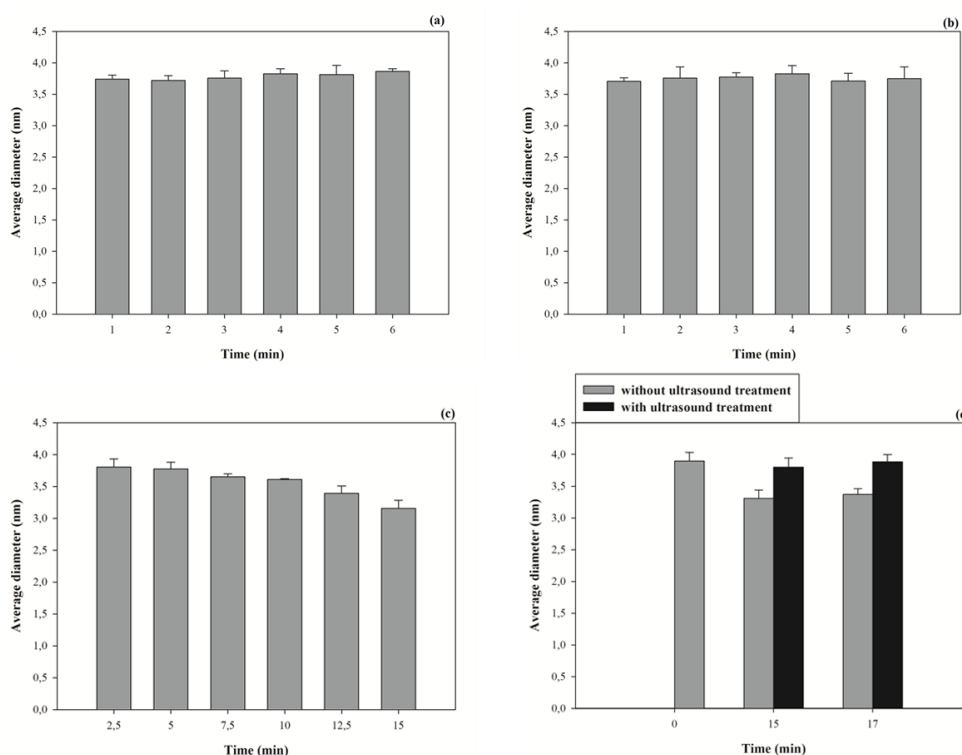


Figure 3.9. Average hydrodynamic diameter of lysozyme (a) subjected to hydrodynamic treatment at a C_i value of 0.93 for the times indicated (b) of non-treated control lysozyme samples at concentrations corresponding to samples subjected to hydrodynamic treatment at C_i value of 0.93 for the times indicated (c) subjected to hydrodynamic treatment at a C_i value of 7.6 for the times indicated (d) subjected to hydrodynamic treatment at a C_i value of 7.6 for the times indicated, before and after 30 s ultrasound treatment.

anticipation that it might provide the necessary energy to prompt the reorganization of structurally-perturbed lysozyme. Remarkably, all observed alterations of hydrodynamic diameter and bioactivity were fully reversed following just 30 s of sonication in an ultrasonic bath (Figure 3.9(d) and Figure 3.10 (c), respectively).

In view of the above results, it followed to reason that lysozyme had experienced a conformational change under non-cavitating hydrodynamic flow conditions, thereafter remaining kinetically trapped in a non-native state. The non-native state (or states) was not elucidated, however, it clearly reflected a subtle conformational change in view that flow-treated lysozyme had only yielded minor alterations to the dynamic light scattering profile and no circular dichroism signature.

It was perhaps counter-intuitive that proteins subjected to the higher energy cavitation process were unaffected to any statistically significant extent, whereas proteins subjected to flow treatment outside the cavitation range experienced noticeable changes to their hydrodynamic diameter and bioactivity. While a confirmable explanation remains outstanding, one hypothesis is that hydrodynamic cavitation, but

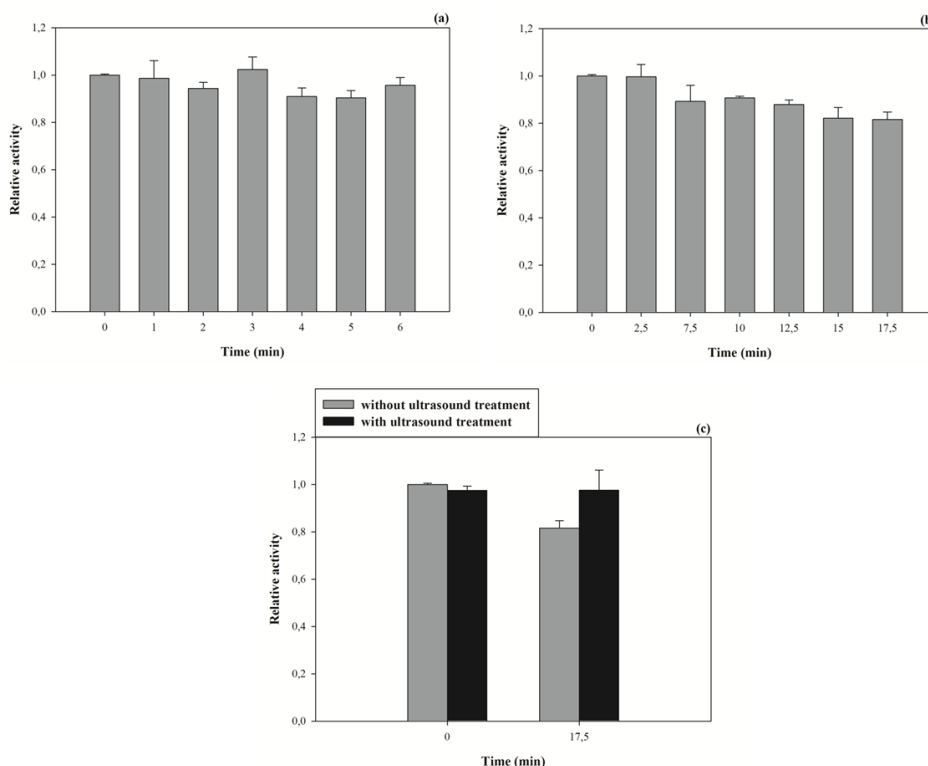


Figure 3.10. Relative activity of lysozyme (a) subjected to hydrodynamic treatment at a C_i value of 0.93 for the times indicated (b) subjected to hydrodynamic treatment at a C_i value of 7.6 for the times indicated (c) subjected to hydrodynamic treatment at a C_i value of 7.6, before and after 30 s ultrasound treatment.

not high shear alone, may have provided the necessary conditions to substantially desolvate the protein, thereby inducing conformational rigidity. Indeed, the notably gassy, bubble-saturated appearance of lysozyme solution under cavitating conditions implied the availability of a large hydrophobic-hydrophilic interfacial area. Studies related to protein foaming have shown that air-water interfaces have the effect of attracting protein and desolvating their hydration shell, with the effect being particularly pronounced along surface-exposed hydrophobic regions [148, 149]. In view of the relatively much larger interfacial area at C_i values of 0.93 compared to 7.6, it is conceivable that a large fraction of lysozyme, under high dilution conditions in particular, would reside at the interface. With sufficient dehydration of the protein surface realized, it follows that lysozyme flow-treated at a C_i value of 0.93 would attain a higher state of rigidity compared to a C_i of 7.6. Proteins manipulated under conditions promoting dehydration and increased conformational rigidity have shown an increased activation barrier, and thus tolerance, to unfolding [150]. In contrast to the cavitation scenario, lysozyme flow-treated outside the cavitation range was perceived to have retained a native-like hydration state. In view of the high conformational flexibility imparted by water, lysozyme could have experienced shear-induced stretching and compression of its structure, thereby assuming one or more new metastable conformations [151]. Once the flow treatment was terminated, the aqueous system did not contain enough energy under ambient conditions to re-equilibrate lysozyme to its native conformation. This view was consistent with the ultrasonication test, which had rapidly restored lysozyme to its native bioactivity and structure. This view was also supported by prior work conducted on lysozyme subjected to different shear rates [152]. In that study, lysozyme was found to have encountered a conformational change, which could, dependent on the conditions, be reversed.

Neither the treatment at $C_i = 0.93$ nor $C_i = 7.6$ was detrimental to the physico-chemistry of lysozyme. The rationale for this claim may be examined below. Evidence showing that lysozyme was neither chemically degraded nor unfolded/misfolded by treatment at $C_i = 0.93$ and evidence showing that lysozyme was neither chemically degraded nor irreversibly unfolded at $C_i = 7.6$:

- 1) SDS-PAGE analyses were performed. No streaking, smearing, or extra bands that could indicate breakdown were observed.

2) DLS analysis of lysozyme subjected to hydrodynamic flow ($C_i = 7.6$ and 0.93) showed no ultra-small particles, which might have indicated peptide fragments in solution.

3) Studies [58] have reported no adverse effect on protein activity until 40 minutes of ultrasonication. Ultrasonication performed on the lysozyme sample (treated previously at $C_i = 7.6$) was limited to only 30s. The activity of lysozyme was fully restored following ultrasonication, indicative of a native structure.

4) The hydrodynamic diameter of lysozyme (treated previously at $C_i = 0.93$) was unchanged, indicating that no dramatic structural change could have taken place. The hydrodynamic diameter of lysozyme (treated previously at $C_i = 7.6$) was reduced, indicative of a more compact structure. Had chemical degradation of the primary structure occurred during hydrodynamic flow, a less compact, more loosely folded structure would have been anticipated (again, DLS showed no evidence of peptide fragments).

All in all, the physico-chemical changes imposed on protein structure upon hydrodynamic treatment describe a very new area of research, which merits further experimentation as well as modeling. While this seminal contribution has documented a decrease of the average hydrodynamic diameter, no information is currently available to rule out the opposite possibility in lysozyme or other test proteins. Further in vitro study is being conducted to ascertain the nature of the conformational change, the role of pH and other environmental factors, and the generality of such changes among different model systems in the protein family. It would stand to reason that in vivo studies could follow.

3.2 Results and Discussion of Nanostructured Heat Sinks

3.2.1 Results and Discussion of Pool Boiling Study

Figure 3.11 and Figure 3.12 show the heat transfer results comparing plain surface to the nanostructured plate using water and ethanol as working fluids, respectively. The effect of the nanostructured plate is clearly observed from the difference in the superimposed graphs. The nanostructured plate increases heat removal rate from the system. It also decreases the boiling inception temperature by $\sim 2^\circ\text{C}$ for both working fluids. The nanorods on the surface of the plate act effectively in the

enhancement of boiling heat transfer. The data presented in Figure 3.11(a) and Figure 3.12(a) shows the superimposed two-phase data from the experiments with and without the nanostructured plate during boiling. These results show that in the boiling region the rise in the surface temperature is suppressed with the application of the nanostructured plate. Boiling heat transfer enhancement of 125% and 110% on average was obtained for water and ethanol, respectively. The reason could be explained by the increase in heat transfer area and the number of active nucleate sites so that more bubbles would emerge during boiling from the nanostructured surface and promote nucleate boiling. Recent studies [70, 153] have shown a significant reduction in the macroscopic water contact angle of some metallic nanorods (such as Pt and Cu), implying the increased wettability because of the enhanced roughness caused by the nanorod structure which, in turn, contributes to enhanced CHF. These effects facilitate enhanced heat removal from the nanostructured surface of the plate and lead to stabilization of the surface temperature (Figure 3.11(d)).

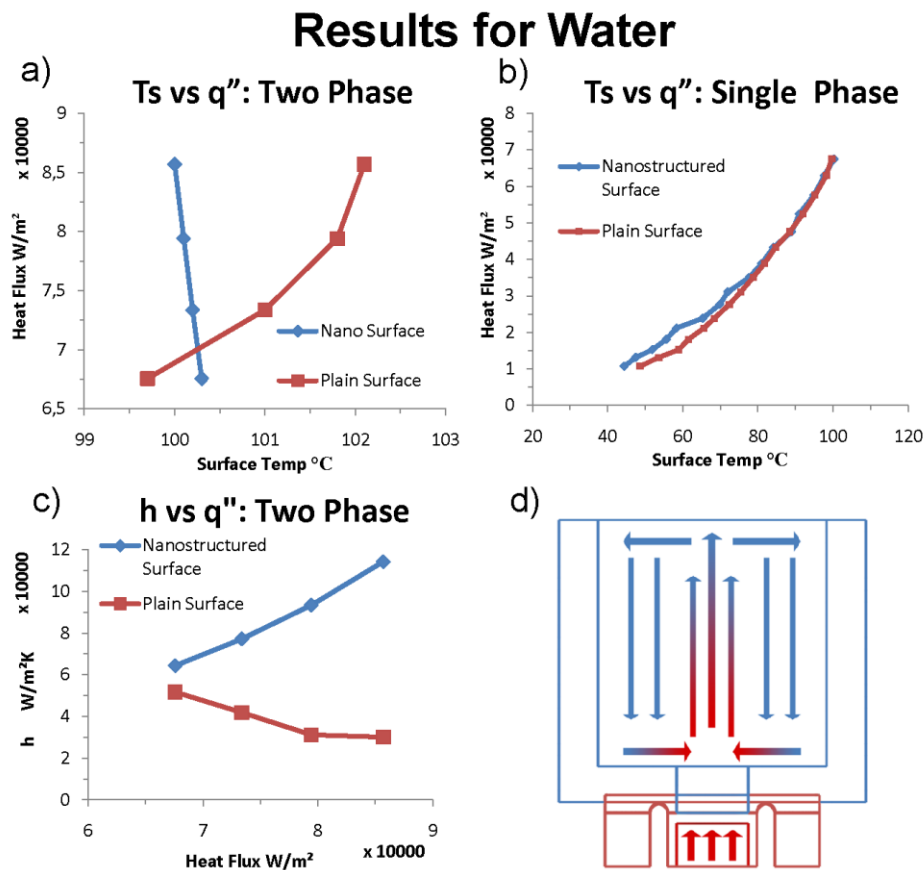


Figure 3.11. Superimposed two phase (a) and single phase (b) heat flux plotted against surface temperature for water. Heat transfer coefficient versus heat flux (c) for two phase region. Schematic of heat removal from the system (d).

Results for Ethanol

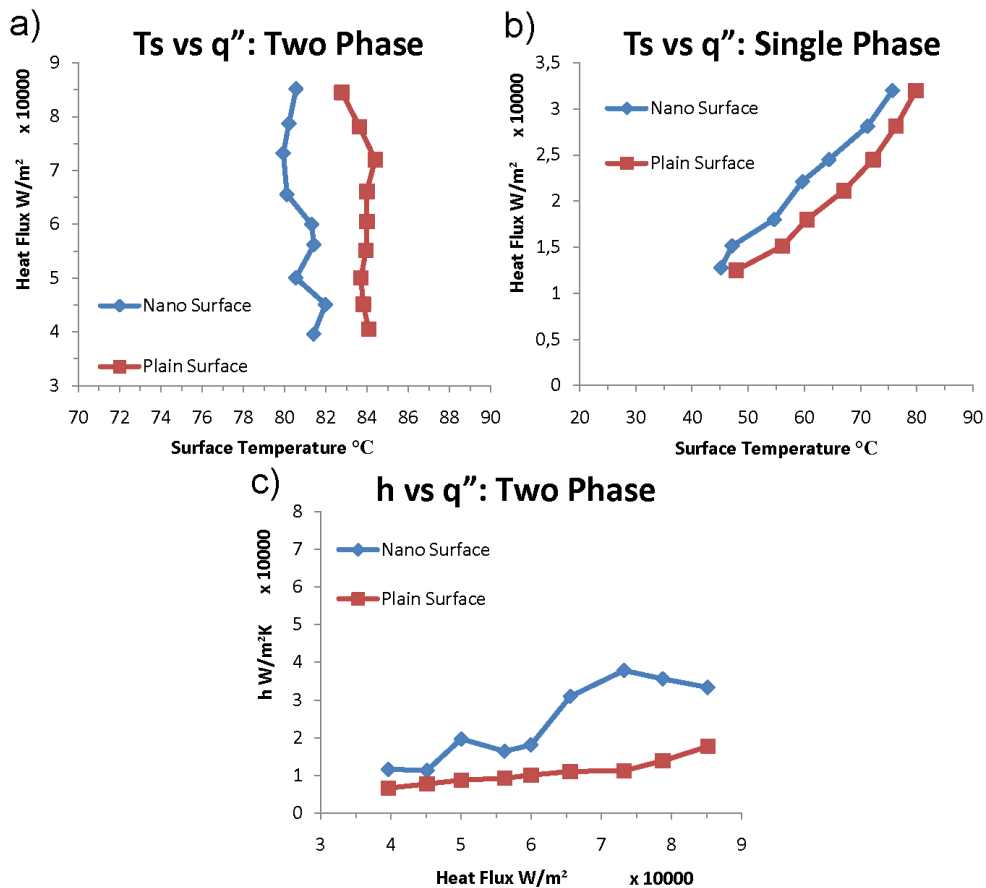


Figure 3.12. Superimposed two phase (a) and single phase (b) heat flux plotted against surface temperature for ethanol. Heat transfer coefficient versus heat flux (c) for two phase region.

Heat removal in the single-phase region is also promoted with the introduction of the nanostructured plate. The single-phase linear slopes are evaluated and 13% decrease in the slope is observed with the nanostructured plate for water. In the case of ethanol, the single-phase results indicate an offset introduced by the nanostructured plate, which, in turn, increases heat removal rate. Thus, even in the single phase the effect of the nanostructured plate is significant because of heat transfer area enhancement (Figure 3.11(b) and Figure 3.12(b)).

During boiling, heat transfer coefficients are deduced from surface temperatures and displayed along with heat flux in Figure 3.11(c) and Figure 3.12(c) for water and ethanol, respectively. The results indicate that the heat transfer coefficient behavior has improved with the nanostructured surface relative to the plain surface configuration. This could be attributed to the reduced wall superheat for boiling inception and promotion of nucleate boiling with nanostructures.

3.2.2 Results and Discussion of Forced Convection Study

Data points for Reynolds number values varying from 23 to 30 are shown in Figure 3.13. Enhanced heat transfer coefficients can be observed from the figure for the cases with the nanostructure. It can be noted that the reduction in the flow rate caused by the nanostructured plate is not significant where all the results correspond to 0.5 psi pressure drop. This is an advantage over pin-fin geometries where the flow rates are reduced much more significantly at constant pressure drop.

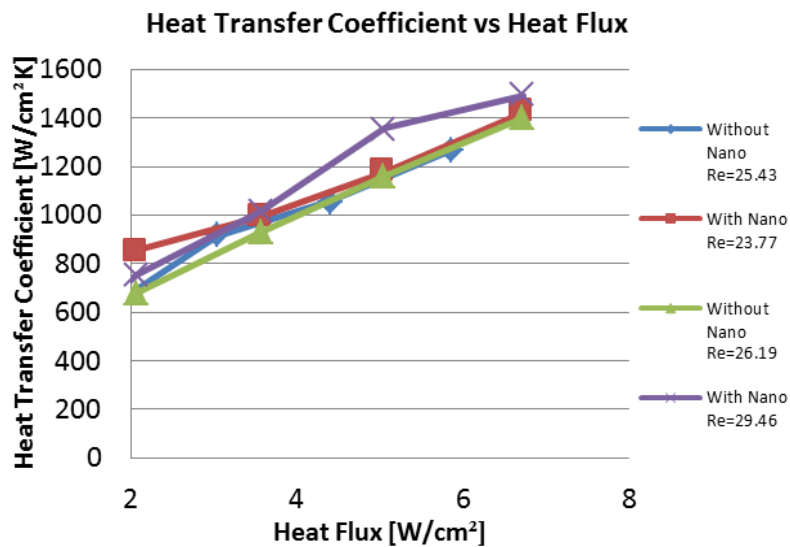


Figure 3.13. Heat transfer coefficient versus heat flux is plotted with $23 < Re < 30$.

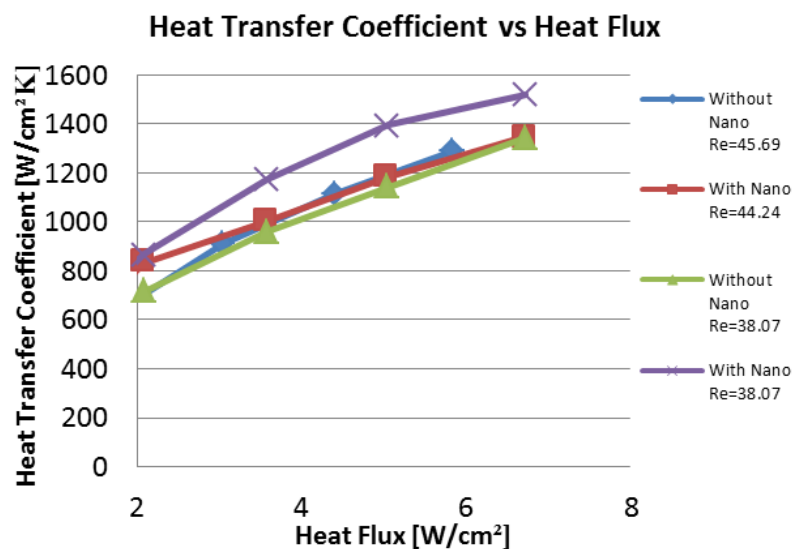


Figure 3.14. Heat transfer coefficient versus heat flux is plotted with $38 < Re < 46$.

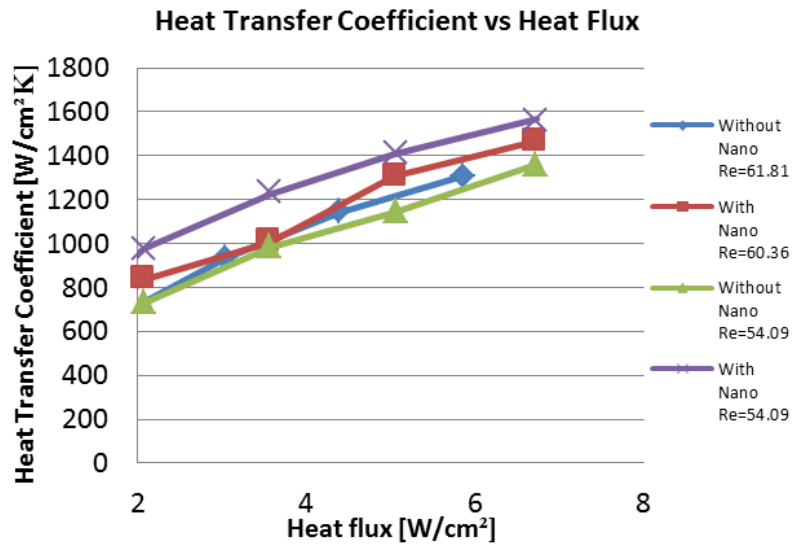


Figure 3.15. Heat transfer coefficient versus heat flux is plotted with $54 < Re < 62$.

The results for constant pressure drop 1.0 psi are quite similar to the results for the 0.5 psi case (Figure 3.14). The flow rate is reduced slightly at the same pressure drop and heat transfer is enhanced. It can be observed that enhancement in the heat transfer coefficient on nanostructured plate compared to the plain surface configuration tends to increase for high heat fluxes in all the results. In other words, cooling enhancement of nanostructured plate is clearer for higher heat fluxes.

As the constant pressure drop is increased further to 1.5psi (Figure 3.15) and 2.0psi (Figure 3.16), the enhancement of the nanostructure becomes more significant.

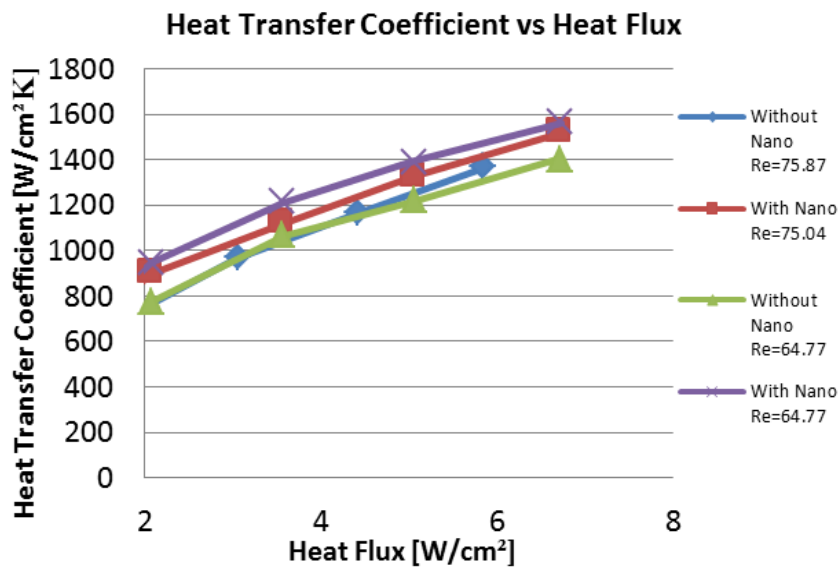


Figure 3.16. Heat transfer coefficient versus heat flux is plotted with $64 < Re < 76$.

The reason for this phenomenon can be explained by the fact that the flow rates are higher. In the case of Cu thin film surface, the reason for lower heat transfer rate compared to nanostructured surfaces is the presence of a thin layer of fluid which acts as a heat transfer resistance, while on nanorods this layer can be easily broken especially at high fluid flow rates. Heat transfer enhancement of 16% on average has been realized with the experimental setup.

3.2.3 Results and Discussion of Jet Impingement Study

The experimental results are obtained as explained in the previous sections. Accordingly, data points for a constant volumetric flow rate of 107.5 ml/min ($Re_j=972.66$) are displayed in Figure 3.17(a) where heat transfer coefficient (h), which quantifies the convective heat transfer capability of a heat sink, is plotted against the heat flux provided from the cylindrical aluminum heaters. As depicted in Figure 3.17(a), heat transfer coefficient values increase with the input heat flux where the experiments are carried out only in the single phase region. This is due to the change in fluid thermophysical properties with temperature (which varies between 30°C-60 °C during the experiments). Enhanced heat transfer coefficients can be observed with the application of the nanostructured plate with vertical nanorods (referred to as “Vertical NR” in the legend), whereas the nanostructured plate with tilted nanorods (referred to as “Tilted NR” in the legend) is proven to be less efficient even than the Cu thin film plate (referred to as “Cu TF” in the legend) implying that the cooling performance of the jet impingement system is not promoted. The enhancement in heat transfer obtained using nanostructured plate with vertical nanorods can be attributed to the secondary flows around the nanorods and the modification of boundary layers developing from the

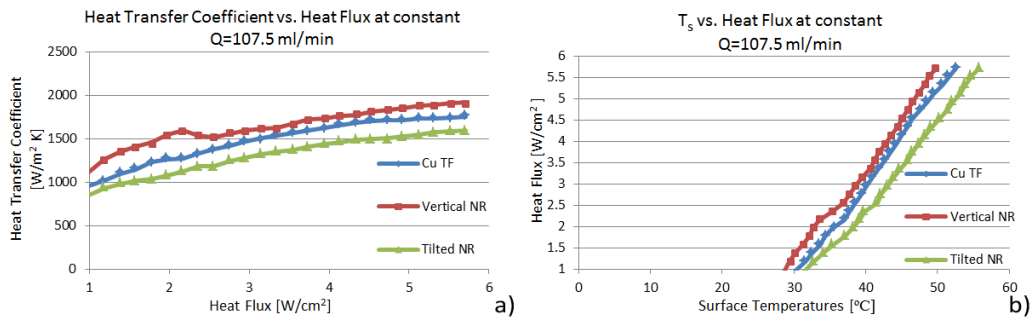


Figure 3.17. (a) Heat transfer coefficient versus heat flux plotted at a constant volumetric flow rate of 107.5 ml/min and (b) Heat flux versus surface temperature plotted at a constant volumetric flow rate of 107.5 ml/min.

heated surface.

Previous works [153] has shown a significant reduction in the macroscopic water contact angle of vertical metallic nanorods, implying the increased wettability because of the enhanced roughness caused by the nanorod structure, which, in turn, contributes to the enhanced heat transfer surface area. Hence, the increased heat transfer surface area available to remove heat from the surface of the base creates a more efficient cooling system. In addition, the nanorods also minimize the heat transfer resistance induced by the presence of a thin layer of the fluid on the subjected surfaces, which can be easily broken on the nanostructured surfaces compared to plain surfaces, thereby further contributing to heat transfer. As explained in the previous SEM images (Figure 2.4(b)), vertical nanorod arrays form a very rough surface increasing the contact area with water and therefore also enhance the heat transfer. Moreover, single crystal structure of individual nanorods is believed to further enhance the heat transfer properties of the nanostructure plate.

On the other hand, the reason for poorer heat transfer performance of the nanostructured plate with tilted nanorods can be attributed to the decreased supply of liquid jets to the base of the plate for the tilted structure, which has smaller gaps compared to the vertical nanorods, where the temperature is at the highest level. This may cause the liquid to be most likely in contact with only the tops of the tilted Cu nanorods which in turn results in poorer heat transfer rate due to the decreased heat transfer surface area and the increased resistance to heat transfer which originated from the air gaps among the tilted nanorods. Moreover, the low heat transfer of tilted nanorods might be also attributed to the non-single crystal property of these nanorods which decreases heat transfer and also enhances the surface oxidation. The surface oxidation can greatly decrease the thermal conductivity and resistance to oxidation

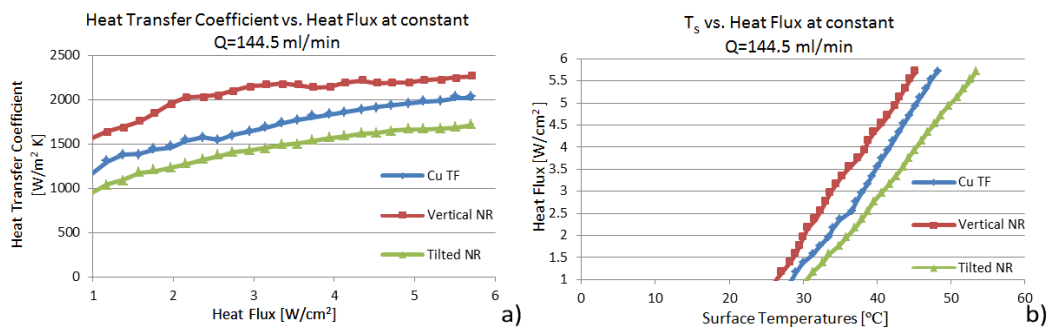


Figure 3.18. (a) Heat transfer coefficient versus heat flux plotted at a constant volumetric flow rate of 144.5 ml/min and (b) Heat flux versus surface temperature plotted at a constant volumetric flow rate of 144.5 ml/min.

degradation of titled nanorods in the present study. However, the vertical nanostructure arrangement with larger gaps allows liquid jet supply to the base, which significantly enhances the liquid-solid contact area and improves the heat transfer.

Surface temperature plotted against heat flux at constant volumetric flow rate of 107.5 ml/min is provided in Figure 3.17(b). As expected, surface temperatures increase linearly with heat flux implying constant heat flux boundary conditions.

The result of the experiments conducted at constant volumetric flow rate of 144.5 ml/min ($Re_j=1307.43$) is depicted in Figure 3.18(a), which follows a similar trend as the lower flow rate. It can be observed that heat transfer coefficients above $2000 \text{ W/m}^2 \text{ K}$ can be achieved at this flow rate, which points out to a further enhancement in heat transfer. It can also be noted that the improvement in the heat transfer coefficient of vertical nanostructured plate compared to the plain surface configuration tends to further increase for higher heat fluxes in all the results. An average enhancement in heat transfer coefficient of 28.9% can be observed in this flow rate, whereas the enhancement obtained with the lower flow rate (107.5 ml/min) was 13.1% on average. Tilted nanorods on the other hand, are still unable to augment heat transfer compared to the flat plate configuration due to the previously discussed reasons. Surface temperature plotted against heat flux at constant volumetric flow rate of 144.5 ml/min is provided in Figure 3.18(b), the surface temperature rises with increasing heat flux similar to the lower flowrate results.

Figure 3.19(a) shows the experimental results of the volumetric flow rate of 181.5 ml/min ($Re_j=1642.21$). Nanostructured plate with vertical nanorods again yields the best results at this flow rate. Further increase in the heat transfer coefficient achievable can be observed with increasing flow rate, which is in total agreement with the lower flowrate results. Average enhancement in heat transfer coefficient of 17.5%

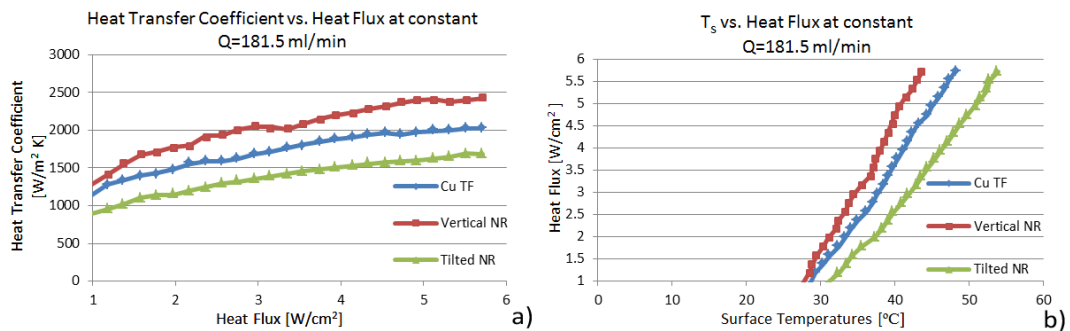


Figure 3.19. (a) Heat transfer coefficient versus heat flux plotted at a constant volumetric flow rate of 181.5 ml/min and (b) Heat flux versus surface temperature plotted at a constant volumetric flow rate of 181.5 ml/min.

has been achieved compared to the plain surface, while the tilted nanorod structure results in the lowest performance similar to the lower flowrate results. Surface

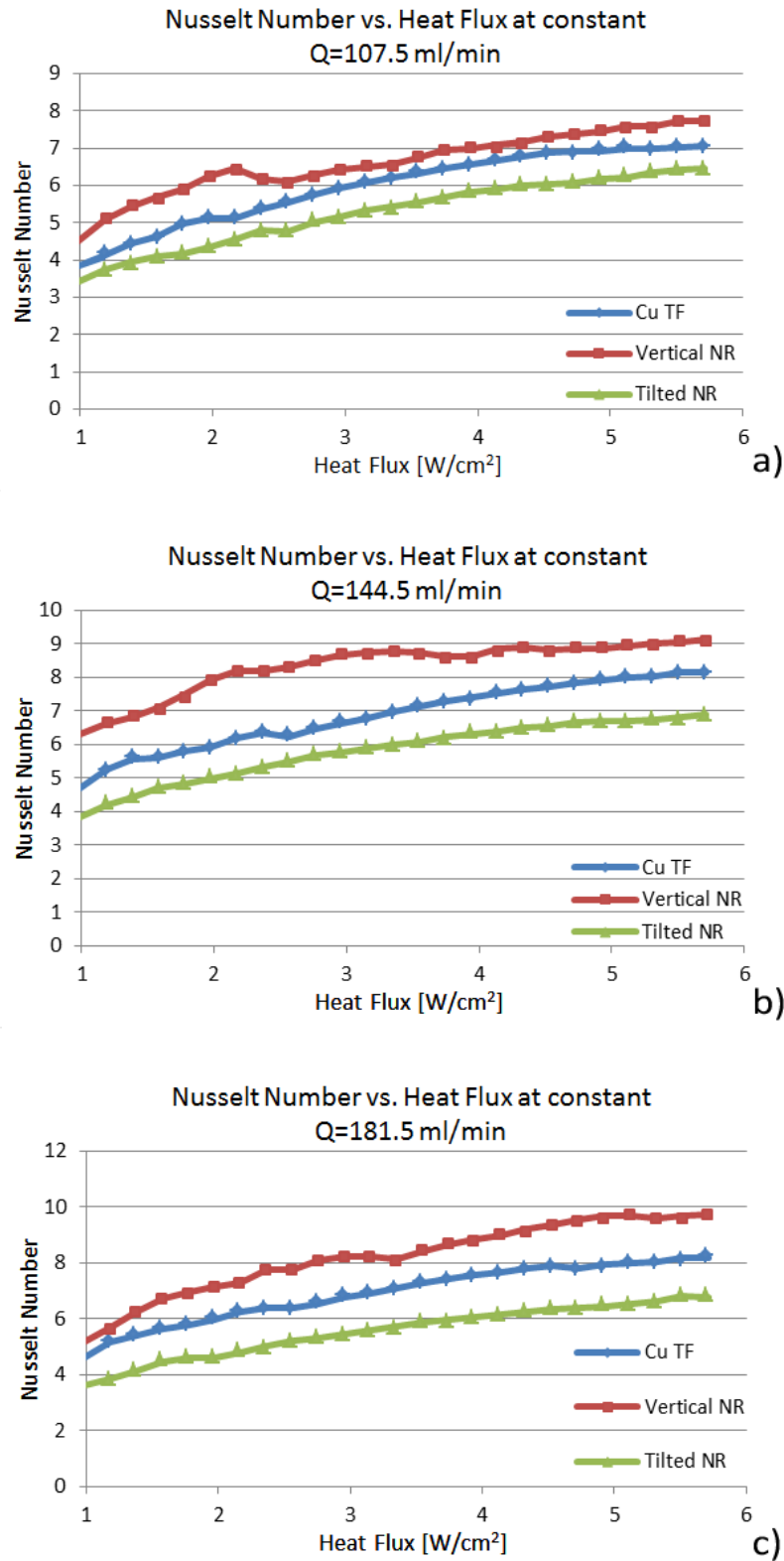


Figure 3.20. Nusselt number versus heat flux plotted at a constant volumetric flow rate of (a) 107.5 ml/min, (b) 144.5ml/min and (c) 181.5ml/min.

temperature plotted against heat flux at constant volumetric flow rate of 181.5 ml/min is provided in Figure 3.19(b).

Nusselt number profiles are displayed in Figure 3.20 for three different flow rates. In these figures, an increase in Nusselt number with the nanostructured plate based on vertical nanorods is apparent. Nusselt numbers are greater for higher flow rates when compared to the lower flow rates at the same heat flux. This result implies that Nusselt number has a strong dependence on Reynolds number, which has been also extensively reported in the literature [154]. It should be noted that Nusselt numbers vary for the same flow rate due to the change in thermophysical properties in the working fluid due to heating. At higher flow rates, Nusselt number values exceeding 8 are observed with the nanostructured surfaces for the proposed cooling device, which is promising.

The enhanced heat transfer performance obtained from the nanostructured surface with vertical nanorods in jet impingement agrees with the previous experimental studies [68] and results on nanostructured surfaces used with other heat transfer modes in the literature [65, 70]. Pool boiling and single phase flow in rectangular channels with nanostructured surfaces were investigated and significant enhancements in heat transfer were reported [63, 64]. Positive effects of the nanostructured surfaces with lightly spaced tilted nanorods have been reported in boiling applications [70], but studies on the performance of such surfaces in jet impingement applications are not present. The experimental studies reported in this article prove that such surfaces with tilted nanorods, when densely packed, fail to enhance heat transfer with jet impingement applications and thus the heat transfer performance of the system is decreased, while their vertical arrangement (orientation) results in the enhanced heat transfer performance.

3.3 Results and Discussion of Nanofluid Actuation Study

The results are obtained from the experiments as explained in the previous sections. Surface temperature data were plotted against heat flux values for the whole experiment (Figure 3.21). It can be observed that the use of magnetically activated nanofluid increases heat removal rate from the system. The surface temperatures have a linear trend with heat flux. The slope of the surface temperature trendline without magnetic stirrer is steeper than the slope of the surface temperature trendline with magnetic

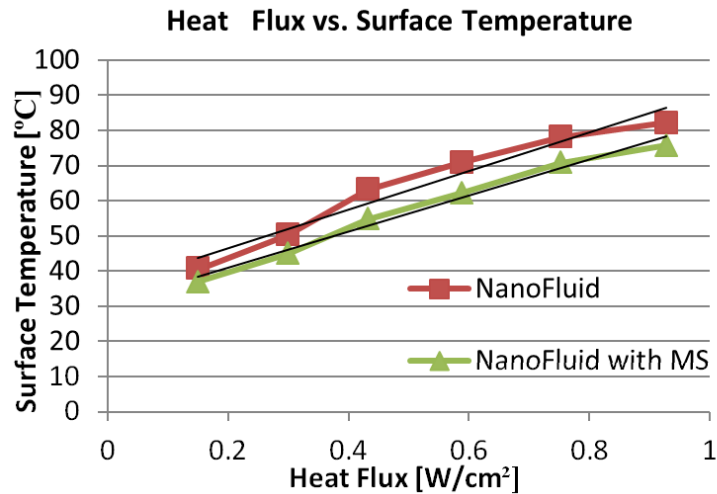


Figure 3.21. Heat Flux vs. Surface Temperature.

stirrer. Thus, heat removal is promoted with the introduction of the nanofluid with ferromagnetic particles subject to the rotating magnetic field generated by the magnetic stirrers. Moreover, the nanofluid provides more mixing in convection mode and increases convection from the surface due to applied rotating magnetic field (Figure 3.22). The iron oxide nanoparticles' motion near the surface and their contact with the heated surface contribute to heat transfer from the heated surface to both the bulk fluid and the nanoparticles themselves. As a result, the magnetic nanoparticles act as heat carriers, absorb more heat from the surface of the plate (Figure 3.22), and further enhance heat transfer, which results in lower surface temperatures at a fixed heat flux with magnetic stirring.

Heat transfer coefficients were found and plotted against heat flux in Figure 3.23. Heat transfer coefficients higher than $200 \text{ W/m}^2\text{K}$ are reached for the nanofluid rotated with magnetic stirrers, while without magnetic stirrers heat transfer coefficients

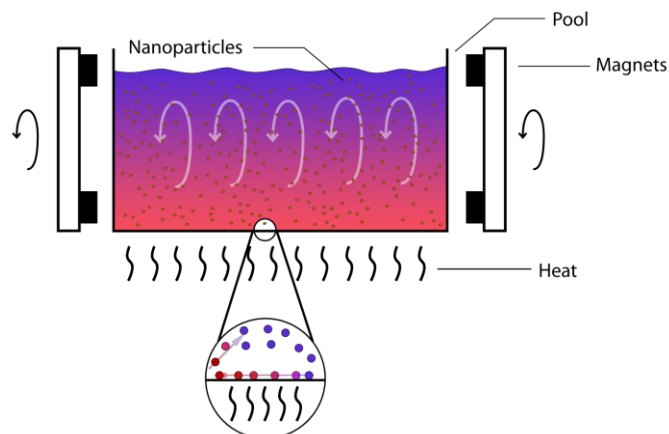


Figure 3.22. Heat Transfer Enhancement Mechanism.

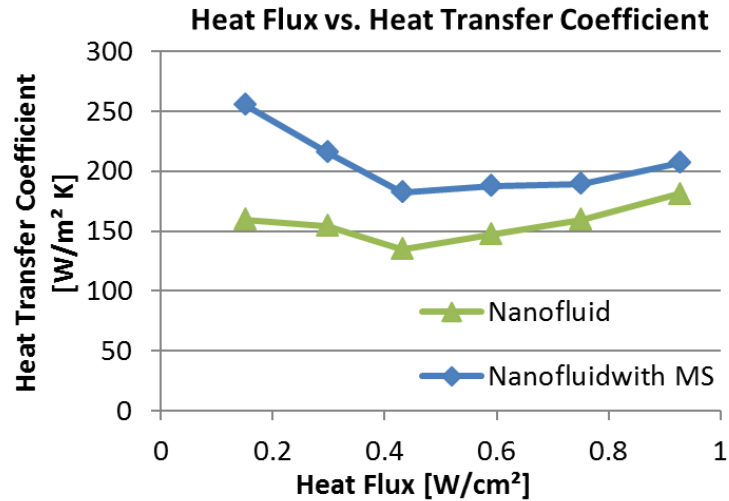


Figure 3.23. Heat Transfer Coefficient vs. Heat Flux.

lower than 200 W/m²K are measured. To better emphasize on the enhancement due to rotating magnetic field, the ratios of heat transfer coefficients of the configuration without magnetic stirrers to heat transfer coefficients of the configuration with magnetic stirrers were displayed for each heat flux value in Figure 3.24. The decrease in the enhancement of heat transfer at elevated heat fluxes could be observed from the graph, while the enhancements are still above 15%. Magnetic stirring enhancement is more significant at lower heat fluxes where convection effects are relatively less dominant due the high viscosity of the fluid at lower temperature. Magnetic stirring is able to actuate the nanofluid within the pool even at lower temperatures thereby augmenting the heat transfer. Convection is intensified at higher heat fluxes due to decreased fluid viscosity and this contributes more to the mixing of the nanofluid within the pool, which is why the enhancement ratio decreases.

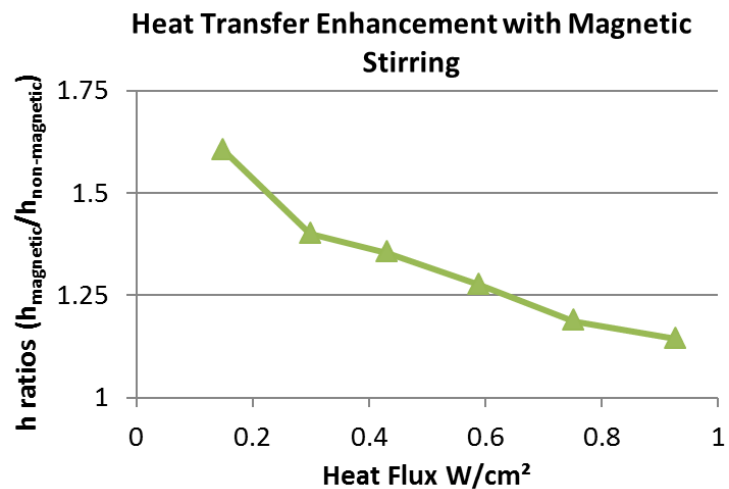


Figure 3.24. Heat Transfer Enhancement Ratio.

Various researchers have shown that, in general, nanofluids offer better heat transfer characteristics compared to their base fluids [105-107]. One of the reasons for that is the improved thermal conductivity due to existence of high conductivity nanoparticles dispersed in the base fluid. It has also been shown that Brownian diffusion (the random motion of nanoparticles within the base fluid) which results from continuous collision between nanoparticles and the molecules of the base fluid and thermophoresis (diffusion of particles under the effect of a temperature gradient) greatly contribute to heat transfer enhancement in nanofluids [108, 109]. In addition to these heat transfer mechanisms, the vibrating and rotating nanoparticles, due to rotating magnetic field, result in an enhanced heat removal from the surface of the pool. In previous studies of the authors [115-118], it was shown that flow velocities greater than 1cm/s were achievable in mini/micro scale at decent magnetic fields ($\sim 0.3\text{mT}$), which are close to those in the current study. This clearly proves the existence of additional contribution of the actuation of magnetic nanoparticles to heat transfer. The nanofluid within the pool acts effectively in the enhancement of heat transfer. The mechanism could be explained by the nanoparticles acting as heat transporters from the surface of the pool to the bulk fluid along with the circulation created within the pool with magnetic field especially at low temperatures (Figure 3.22).

4 CONCLUSION

4.1 Conclusion of Hydrodynamic Cavitation Study

4.1.1 Conclusion of Hydrodynamic Cavitation Application to Chalk and Cancerous Cells

The potential of hydrodynamic cavitation for the use in medical treatment was explored. Two sets of experiments were undertaken, using first the chalk specimens as an artificial kidney stone model and second the cell cultures containing cancerous cells.

Both target materials were exposed to bubbly cavitation hydrodynamically generated by a microorifice, and the changes in the targets were carefully examined. The following conclusions were drawn from the results of the respective experiments.

- 1) The performance of bubbly cavitation has been tested on chalk. Significant decrease in size and rapid erosion on the surface of the material indicated that hydrodynamic cavitation has the potential to lead to an alternative and minimally invasive surgical technique to remove urinary stones.
- 2) The hydrodynamic cavitation system could easily be coupled with an endoscopic system. Due to the small diameter of the cavitating probe (147 μm), a camera and a suction probe could be integrated within conventional endoscopic systems, which have distal ends variable from 3.2–12.8 mm diameter.
- 3) Microscale bubbly cavitation caused cell death in two different cancer cell types in culture. Cell death kinetics depended on the exposure time to cavitation (i.e., death in cells exposed to cavitation for 1 min was less than that in cells exposed for 5 min). Additionally, a dramatic increase in death of cells in culture was observed hours after such exposure. These findings revealed the potential of the use of hydrodynamic bubbly cavitation in abnormal tissue (e.g., BPH or tumors) ablation and treatment.

The results from the experiments demonstrated that hydrodynamic cavitation might be used as a promising alternative to ultrasound methods in order to treat various diseases, such as cancer, BPH, and kidney stone formation. In contrast to some ultrasonic methods, hydrodynamic cavitation offers fine controllability, low power

consumption, heat-free cavitation, and successful targeting. Its destructive effects were tested on chalk and cell cultures. However, further *in vivo* studies (i.e., exposure on dead and live tissues) are needed for better understanding and characterization of the possible outcomes of the proposed method.

4.1.2 Conclusion of Hydrodynamic Cavitation Application to Protein

In this initial study, lysozyme subjected to hydrodynamic flow under cavitating and non-cavitating conditions was assessed via biochemical and biophysical methods. The findings indicated that hydrodynamic cavitation, with C_i set to a value of 0.93, had no statistically significant effect on lysozyme structure and function under the applied experimental conditions. Interestingly, a reversible change of hydrodynamic diameter and bioactivity was noted outside the cavitation regime with C_i set to a value of 7.6. Overall, the results were encouraging in the sense that lysozyme was neither deactivated, nor irreversibly affected in any adverse way. In view that the analysis was primarily phenomenological, it follows to reason that more work is needed to better ascertain the rules that govern protein behavior in high-shear environments, as well as to assess the risks, benefits and feasibility of applying invasive hydrodynamic cavitation to healthcare.

4.2 Conclusions of Nanostructured Heat Sinks

4.2.1 Conclusion of Pool Boiling Study

In conclusion regarding pool boiling enhancement with nanostructures, the results show that glancing angle deposited nanorod arrays can considerably enhance the nucleate boiling and heat transfer properties leading to superior cooling of the underlying plate. The enhancement in heat transfer was significant especially during boiling, where nanostructured surfaces induced heat transfer enhancement of 125% and 110% on average for water and ethanol, respectively. Therefore these nanorod integrated plates offer opportunities for enhanced cooling of various applications such as small electronic devices, microreactors, micropropulsion, biotechnology, fuel cells and air conditioning.

4.2.2 Conclusion of Forced Convection Study

The results gathered from our experimental work indicate the advantageous effects of a nanostructured plate on heat transfer enhancement via a single-phase rectangular channel flow over flat plate. The vertical nanorods integrated to the copper thin film layer on silicon wafer introduce enhanced surface area and does not cause any significant losses in terms of flow rates at a constant pressure drop scenario. With such a compact setup and integrated nanostructures, the cooling system acts more efficiently. An average heat transfer enhancement of 16% was obtained with the experimental setup.

Using such experimental studies, further investigations and models, nanostructures of different nanorod lengths and diameters can be utilized in various cooling applications of small electronic devices, microreactors, micropropulsion, biotechnology, fuel cells and air conditioning.

4.2.3 Conclusion of Jet Impingement Study

The results gathered from our experimental work indicate the advantageous effects of a vertical nanostructured plate on heat transfer enhancement via a single-phase submerged jet impingement cooling device. An average heat transfer enhancement of 28.9% using the nanostructured plate utilizing vertical nanorods has been measured compared to flat plate. The vertical nanorods integrated to the copper thin film layer on silicon wafer introduce enhanced surface area. The nanorods also act as nanoscale pin-fins, which contribute to heat transfer enhancement with secondary flows and changing boundary layers developing from the surface. By using a compact setup with integrated nanostructures, the cooling system acts more efficiently compared to its plain surface counterparts, while the orientation of nanostructures is found to be an important parameter for heat transfer.

In the light of the experimental studies, more in-depth systematic studies to control the length, spacing, orientation and diameter of nanorods are critically important for fundamental understanding of heat transfer occurring from the nanostructured surfaces as well as to clarify the potential benefits/limitations of this technology in various applications such as cooling of small electronic devices like micro reactors, micro propulsion, biotechnology, fuel cells and air conditioning. Moreover, there is a need to

develop empirical correlations for calculating the heat transfer coefficients of the nanostructured surfaces, which can be useful in designing such devices for cooling applications.

4.3 Conclusion of Nanofluid Actuation Study

The results gathered from the experiments indicate the advantageous effects of magnetic nanofluid actuation (using ferromagnetic particles integrated with magnetic stirrer) on heat transfer magnification and flow circulation. With such a compact setup, the magnetic stirrer integrated to this cooling system acts effectively. An average heat transfer coefficient enhancement of 37.5% was achieved with the magnetic actuation with relatively low power consumption. Using experimental results, further investigations and models, nanofluids of ferromagnetic particles can be utilized in various cooling applications of small electronic devices, microreactors, micropropulsion, biotechnology, fuel cells and air conditioning. Further studies could include two-phase pool boiling experiments of various nanofluids with and without a magnetic stirrer and their comparisons amongst themselves and distilled water. The fraction of magnetic nanoparticles inside the nanofluid could also be modified in order to account for its advantageous effects. The magnetic flux densities of the magnets could be modified in order to see its effects on the heat transfer enhancement.

REFERENCES

- [1] C. E. Brennen, *Fundamentals of Multiphase Flow*, New York: Cambridge Univ. Press, 2005.
- [2] C. E. Brennen, *Cavitation and Bubble Dynamics*, London, U.K.: Oxford Univ. Press, 1995.
- [3] C. T. Crowe, *Multiphase Flow Handbook*, Boca Raton, FL: CRC, 2006.
- [4] [Online]. Available: <http://media.photobucket.com/image/cavitation%20propeller/hwsiii3/Tackle%20for%20Sale/Propavitation.jpg>. [Accessed 12 July 2011].
- [5] [Online]. Available: http://getenecon.com/Portals/0/images/800px-Cavitation_Propeller_Damage.jpg. [Accessed 12 July 2011].
- [6] A. Kosar, A. Akbas, O. Sahin, A. Kubilay, O. Oral and D. Gozuacik, "Bubbly Cavitating Flow Generation and Investigation of Its Erosional Nature for Biomedical Applications," in *Proceedings of 2nd Micro and Nano Flows Conference*, West London, UK., 2009.
- [7] C. Mishra and Y. Peles, "Cavitation in Flow through a micro-orifice inside a Silicon microchannel," *Phys. Fluids*, vol. 17, pp. 013601-013615, 2005.
- [8] V. S. Moholkar, P. Senthil Kumar and A. B. Pandit, "Hydrodynamic Cavitation for Sonochemical Effects," *Ultrason. Sonochem.*, vol. 6, no. 1-2, pp. 53-65, 1999.
- [9] B. Schneider, A. Kosar, C. J. Kuo, C. Mishra, G. S. Cole, R. P. Scaringe and Y. Peles, "Cavitation Enhanced Heat Transfer in microchannels," *J. Heat Transfer*, vol. 128, pp. 1293-1301, 2006.
- [10] S. Buogo and G. B. Cannelli, "Implosion of an Underwater Spark-Generated Bubble and Acoustic Energy Evaluation using the Rayleigh Model," *J. Acoust. Soc. Am.*, vol. 111, no. 6, pp. 2594-2600, 2002.
- [11] C. Goldenstedt, D. Melodelima, F. Mithieux, S. Chesnais, Y. Theillere and D. Cathignol, "Cavitation Enhances Treatment Depth When Combined with Thermal Effect using a Plane Ultrasound Transducer: An in vivo study," *Proc. IEEE Ultrason. Symp.*, vol. 1, pp. 709-712, 2004.
- [12] D. Melodelima and D. Cathignol, "Cancer Treatment by Ultrasound: Increasing the Depth of Necrosis," *Appl. Phys. Lett.*, vol. 84, pp. 5365-5367, 2004.
- [13] S. Thüroff, C. Chaussy, G. Vallancien, W. Wieland, H. J. Kiel, A. Le Duc, F. Desgrandchamps, J. De La Rosette and A. Gelet, "High Intensity Focused Ultrasound and Localized Prostate Cancer: Efficacy Results from the European Multicentric Study," *J. Endourol.*, vol. 17, pp. 673-677, 2003.
- [14] G. O. N. Oosterhof, E. B. Comel, G. A. H. J. Smits, F. M. J. Debruyne and J. A. Schalken, "The Influence of High Energy Shock Waves on the Development of Metastasis," *Ultrasound Med. Biol.*, vol. 22, pp. 339-344, 1996.
- [15] H. Wan, P. VanBaren, E. S. Ebbini and C. A. Cain, "Ultrasound Surgery: Comparison of Strategies using Phased Array Systems," *IEEE Trans. Ultrason. Ferroelectr. Freq. Control*, vol. 43, no. 6, pp. 1085-1098, 1996.
- [16] L. R. Gavrilov and J. W. Hand, "Development and Investigation of Ultrasound Linear Phased Arrays for Transrectal Treatment of Prostate," *Ultrason. Sonochem.*, vol. 4, pp. 173-174, 1997.
- [17] J. Tavakkoli, A. Mehta, C. Miller, R. Seip, N. T. Sanghvil, L. Cheng, T. A. Gardner and A. L. Shalhav, "A Laparoscopic HIFU Probe with Integrated Phased Array

- Ultrasound Imaging," in *3rd Int. Symp. Ther. Ultrasound*, Lyon, France, 2003.
- [18] K. Hynynen, G. T. Clement, N. McDannold, N. Vykhodtseva, R. King, P. J. White, S. Vitek and F. A. Jolesz, "500-Element Ultrasound Phased Array System for Noninvasive Focal Surgery of the Brain: A Preliminary Rabbit Study with ex vivo Human Skulls," *Magn. Reson. Med.*, vol. 52, pp. 100-107, 2004.
- [19] K. Y. Saleh and N. B. Smith, "Two-dimensional Ultrasound Phased Array Design for Tissue Ablation for Treatment of Benign Prostatic Hyperplasia," *Int. J. Hyperthermia*, vol. 20, pp. 7-31, 2004.
- [20] K. Y. Saleh and N. B. Smith, "A 63 Element 1.75 dimensional Ultrasound Phased Array for the Treatment of Benign Prostatic Hyperplasia," *Biomed. Eng. Online*, vol. 4, no. 39, 2005.
- [21] D. Melodelima, R. Salomir, C. Mougenot, M. C and C. D., "64-Elements Intraluminal Ultrasound Cylindrical Phased Array for Transesophageal Thermal Ablation under Fast MR Temperature Mapping: An ex vivo study," *Med. Phys.*, vol. 33, pp. 2926-2934, 2006.
- [22] J. F. Bakker, M. M. Paulides, I. M. Obdeijn, G. C. van Rhooon and K. W. A. van Dongen, "An Ultrasound Cylindrical Phased Array for Deep Heating in the Breast: Theoretical Design using Heterogeneous Models," *Phys. Med. Biol.*, vol. 54, pp. 3201-3215, 2009.
- [23] C. R. Merritt, "Ultrasound Safety: What are the Issues?," *Radiology*, vol. 173, pp. 304-306, 1989.
- [24] E. J. Halpern, "High-Intensity Focused Ultrasound Ablation: Will Image-Guided Therapy Replace Conventional Surgery?," *Sci. Pract.*, vol. 235, pp. 345-346, 2005.
- [25] Z. Xu, A. Ludomirsky, L. Y. Eun, T. L. Hall, B. C. Tran, J. B. Fowlkes and C. A. Cain, "Controlled Ultrasound Tissue Erosion," *IEEE Trans. Ultrason. Ferroelectr. Freq. Control*, vol. 51, no. 6, pp. 726-736, 2004.
- [26] J. E. Parsons, C. A. Cain, G. D. Abrams and J. B. Fowlkes, "Pulsed Cavitation Ultrasound Therapy for Controlled Tissue Homogenization," *Ultrasound Med. Biol.*, vol. 32, pp. 115-129, 2006.
- [27] W. W. Roberts, T. L. Hall, K. Ives, J. S. Wolf, J. B. Fowlkes and C. A. Cain, "Pulsed Cavitation Ultrasound: A Noninvasive Technology for Controlled Tissue Ablation (Histotripsy) in the Rabbit Kidney," *J. Urol.*, vol. 175, pp. 734-738, 2006.
- [28] A. M. Lake, T. L. Hall, K. Kieran, J. B. Fowlkes and C. A. R. W. W. Cain, "Histotripsy: Minimally Invasive Technology for Prostatic Tissue Ablation in an in vivo Canine Model," *Urology*, vol. 72, pp. 682-686, 2008.
- [29] K. Kieran, T. L. Hall, J. E. Parsons, J. S. Wolf, J. B. Fowlkes, C. A. Cain and W. W. Roberts, "Refining Histotripsy: Defining the Parameter Space for the Creation of Nonthermal Lesions with High Intensity, Pulsed Focused Ultrasound of the in vitro Kidney," *J. Urol.*, vol. 178, pp. 672-676, 2007.
- [30] Z. Xu, M. Raghavan, T. L. Hall, M. A. Mycek, J. B. Fowlkes and C. A. Cain, "Evolution of Bubble Clouds Induced by Pulsed Cavitation Ultrasound Therapy-Histotripsy," *IEEE Trans. Ultrason. Ferroelectr. Freq. Control*, vol. 55, no. 5, pp. 1122-1132, 2008.
- [31] T. Y. Wang, Z. Xu, F. Winterroth, T. L. Hall, E. D. Rothman, J. B. Fowlkes, W. W. Roberts and C. A. Cain, "Quantitative Ultrasound Backscatter for Pulsed Cavitation Ultrasound Therapy-Histotripsy," *IEEE Trans. Ultrason. Ferroelectr. Freq. Control*, vol. 56, no. 5, pp. 995-1005, 2009.
- [32] Z. Xu, G. Owens, D. Gordon, C. A. Cain and A. Ludomirsky, "Non-invasive

- Creation of an Atrial Septal Defect by Histotripsy in a Canine Model," *Circulation*, vol. 121, pp. 742-749, 2010.
- [33] T. Giesecke and K. Hynynen, "Ultrasound- Mediated Cavitation Thresholds of Liquid Perfluorocarbon Droplets in vitro," *Ultrasound Med. Biol.*, vol. 29, pp. 1359-1365, 2003.
- [34] K. Kawabata and S. Umemura, "Xanthene Dyes for Reducing Acoustic Cavitation Threshold in Aqueous Solution," *Ultrasonics*, vol. 35, pp. 469-474, 1997.
- [35] V. Larina, B. M. Evers, T. V. Ashitkov, C. Bartels, K. V. Larin and R. O. Esenaliev, "Enhancement of Drug Delivery in Tumors by Using Interaction of Nanoparticles with Ultrasound Radiation," *Technol. Cancer Res. Treat.*, vol. 4, pp. 217-226, 2005.
- [36] B. Gilles, J. C. Bera, J. L. Mestas and D. Cathignol, "Reduction of Ultrasound Inertial Cavitation Threshold Using Bifrequency Excitation," *Appl. Phys. Lett.*, vol. 89, no. 9, pp. 094106-1-094106-3, 2006.
- [37] I. Saletes, B. Gilles and J. C. Bera, "Promoting Inertial Cavitation by Nonlinear Frequency Mixing in a Bifrequency Focused Ultrasound Beam," *Ultrasonics*, vol. 51, pp. 94-101, 2011.
- [38] W. S. Chen, T. J. Matula, A. A. Brayman and L. A. Crum, "A Comparison of the Fragmentation Thresholds and Inertial Cavitation Doses of Different Ultrasound Contrast Agents," *J. Acoust. Soc. Amer.*, vol. 113, pp. 643-651, 2003.
- [39] J. E. Lingeman, J. Woods, P. D. Toth, A. P. Evan and J. A. McAteer, "The Role of Lithotripsy and its Side Effects," *J. Urol.*, vol. 141, pp. 793-797, 1989.
- [40] J. E. Lingeman, J. A. McAteer, E. Gnessin and A. P. Evan, "Shock Wave Lithotripsy: Advances in Technology and Technique," *Nat. Rev. Urol.*, vol. 6, pp. 660-670, 2009.
- [41] S. P. Dretler, "Stone Fragility-A new Therapeutic Distinction," *J. Urol.*, vol. 139, pp. 1124-1127, 1988.
- [42] L. W. Klee, C. G. Brito and J. E. Lingeman, "The Clinical Implications of Brushite Calculi," *J. Urol.*, vol. 145, pp. 715-718, 1991.
- [43] P. Zhong, C. J. Chuong and G. M. Preminger, "Characterization of Fracture Toughness of Renal Calculi using Microindentation Technique," *J. Mater. Sci. Lett.*, vol. 12, pp. 1460-1462, 1993.
- [44] S. C. Kim, E. K. Burns, J. E. Lingeman, R. F. Paterson, J. A. McAteer and J. C. Williams Jr., "Cystine Calculi: Correlation of CT-visible Structure, CT number, and Stone Morphology with Fragmentation by Shock Wave Lithotripsy," *Urol. Res.*, vol. 35, pp. 319-324, 2007.
- [45] J. E. Lingeman, B. R. Matlaga and A. P. Evan, "Surgical Management of Upper Urinary Tract Calculi," in *Campbell-Walsh Urology*, 9th ed., Philadelphia, PA, Saunders (an imprint of Elsevier Science), 2006, pp. 1431-1507.
- [46] J. V. Kaude, C. M. Williams, M. R. Millner, K. N. Scott and B. Finlayson, "Renal Morphology and Function Immediately after Extracorporeal Shockwave Lithotripsy," *Amer. J. Roentgenol.*, vol. 145, pp. 305-313, 1985.
- [47] A. P. Evan and J. A. McAteer, "Kidney Stones: Medical and Surgical Management," Philadelphia, PA, Lippincott-Raven, 1996, pp. 549-570.
- [48] J. A. McAteer and A. P. Evan, "The Acute and Long-Term Adverse Effects of Shock Wave Lithotripsy," *Semin. Nephrol.*, vol. 28, pp. 200-213, 2008.
- [49] V. S. Moholkar and A. B. Pandit, "Modeling of Hydrodynamic Cavitation Reactors: A Unified Approach," *Chem. Eng. Sci.*, vol. 56, pp. 6295-6302, 2001.

- [50] V. S. Moholkar and A. B. Pandit, "Numerical Investigations in the Behaviour of one-dimensional Bubbly Flow in Hydrodynamic Cavitation," *Chem. Eng. Sci.*, vol. 56, pp. 1411-1418, 2001.
- [51] S. Arrojo and Y. Benito, "A Theoretical Study of Hydrodynamic Cavitation," *Ultrason. Sonochem.*, vol. 15, pp. 203-211, 2008.
- [52] C. Mishra and Y. Peles, "Flow Visualization of Cavitating Flows through a Rectangular Slot micro-orifice Ingrained in a microchannel," *Phys. Fluids*, vol. 17, pp. 113602-113615, 2005.
- [53] C. Mishra and Y. Peles, "Size Scale Effects on Cavitating Flows through microorifices Entrenched in Rectangular microchannels," *J. Microelectromech. Syst.*, vol. 14, pp. 987-999, 2005.
- [54] C. Mishra and Y. Peles, "An Experimental Investigation of Hydrodynamic Cavitation in micro-venturis," *Phys. Fluids*, vol. 18, pp. 103603-103607, 2006.
- [55] A. Kosar, M. Sesen, Z. Itah, O. Oral and D. Gozuacik, "Bubbly Cavitating Flow Generation and Investigation of Its Erosional Nature for Biomedical Applications," *IEEE Transactions on Biomedical Engineering*, vol. 58, no. 5, pp. 1337-1346, 2011.
- [56] F. E. Cohen and J. W. Kelly, "Therapeutic Approaches to Protein-Misfolding Diseases," *Nature*, vol. 426, pp. 905-909, 2003.
- [57] P. J. Thomasa, B. H. Qua and P. L. Pedersen, "Defective Protein Folding as a Basis of Human Disease," *Trends. Biochem. Sci.*, vol. 20, no. 11, pp. 456-459, 1995.
- [58] C. Marchioni, E. Riccardi, S. Spinelli, F. Dell'Unto, P. Grimaldi, A. Bedini, C. Giliberti, L. Giuliani, R. Palomba and A. CongiuCastellano, "Structural Changes Induced in Proteins by Therapeutic Ultrasounds," *Ultrasonics*, vol. 49, no. 6-7, pp. 569-576, 2009.
- [59] I. Gulseren, D. Güzey, B. D. Bruce and J. Weiss, "Structural and Functional Changes in Ultrasonicated Bovine Serum Albumin Solutions," *Ultrason. Sonochem.*, vol. 14, no. 2, pp. 173-183, 2007.
- [60] P. Jolles, *Lysozymes--Model Enzymes in Biochemistry and Biology*, Basel, Boston: Birkhauser Verlag, 1996.
- [61] T. Kunugi, K. Muko and M. Shibahara, "Ultrahigh Heat Transfer Enhancement using Nano-porous Layer," *Superlattices and Microstructures*, vol. 35, pp. 531-542, 2004.
- [62] K. M. Stone, "Review of Literature on Heat Transfer Enhancement in Compact Heat Exchangers," *ACRC TR-105*, 1996.
- [63] M. Sesen, W. Khudhayer, T. Karabacak and A. Kosar, "A Compact Nanostructure Integrated Pool Boiler for Microscale Cooling Applications," *Micro&Nano Letters*, vol. 5, no. 4, pp. 203-206, 2010.
- [64] M. Sesen, W. Khudhayer, T. Karabacak, A. B. Kosar, B. A. Ahishalioglu and A. Kosar, "A Compact Nanostructure Enhanced Heat Sink with Flow in a Rectangular Channel," in *Proceedings of the ASME 2010 10th Biennial Conference on Engineering Systems Design & Analysis, ESDA2010-25336*, Istanbul, Turkey, 2010.
- [65] H. S. Ahn, V. Sathyamurthi and B. D., "Pool Boiling Experiments on a Nano-Structured Surface," *IEEE Transactions on Components and Packaging Technologies*, vol. 32, no. 1, pp. 156-165, 2009.
- [66] S. Ujereh, T. S. Fisher, I. Mudawar, P. B. Amama and W. Qu, "Enhanced Pool Boiling using Carbon Nanotube Arrays on a Silicon Surface," in *ASME Int. Mechanical Engineering Congress & Exposition*, Orlando, FL, 2005.
- [67] Z. M. Zhang, *Nano/microscale Heat Transfer*, McGraw-Hill, Nanoscience &

Technology Series, 2007.

- [68] K. Kordás, G. Tóth, P. Moilanen, K. M., J. Vähäkangas, A. Uusimäki, R. Vajtaia and A. P. M., "Chip Cooling with Integrated Carbon Nanotube Microfin Architectures," *Applied Physics Letters*, vol. 90, no. 12, pp. 123105/1-123105/3., 2007.
- [69] W. I. Son, J.-H. Hong and J.-M. Hong, "Fabrication of Micro-Heatsink by Nanotemplate Synthesis and its Cooling Characteristics," *Span. Conf. Electron Devices*, Vols. 2-4, pp. 439-442, 2005.
- [70] C. Li, Z. Wang, P.-I. Wang, Y. Peles, N. Koratkar and G. P. Peterson, "Nanostructured Copper Interfaces for Enhanced Boiling," *Small*, vol. 4, no. 8, p. 1084–1088, 2008.
- [71] P. Keblinski, J. A. Eastman and D. G. Cahill, "Nanofluids for Thermal Transport," *Mater. Today*, vol. 8, no. 6, pp. 36-44, 2005.
- [72] I. C. Bang and S. H. Chang, "Boiling Heat Transfer Performance and Phenomena of Al₂O₃–Water Nano-Fluids from a Plain Surface in a Pool," *Int. J. Heat Mass Transfer*, vol. 48, no. 12, p. 2407–2419, 2005.
- [73] P. Vassallo, R. Kumar and S. D'Amico, "Pool Boiling Heat Transfer Experiments in Silica–Water Nano-Fluids," *Int. J. Heat Mass Transfer*, vol. 47, no. 2, p. 407–411, 2004.
- [74] S. Vemuri and K. J. Kim, "Pool Boiling of Saturated FC-72 on Nano-Porous Surface," *Int. Commun. Heat Mass Transf.*, vol. 32, no. 1-2, p. 27–31, 2005.
- [75] D. Milanova and R. Kumar, "Role of Ions in Pool Boiling Heat Transfer of Pure and Silica Nanofluids," *Appl. Phys. Lett.*, vol. 87, no. 23, 2005.
- [76] S. M. You, J. H. Kim and K. H. Kim, "Effect of Nanoparticles on Critical Heat Flux of Water in Pool Boiling Heat Transfer," *Appl. Phys. Lett.*, vol. 83, no. 16, 2003.
- [77] H. Kim, J. Kim and M. Kim, "Experimental Study on CHF Characteristics of Water TiO₂ Nano-Fluids," *Nucl. Eng. Technol.*, vol. 38, no. 1, p. 61–68, 2006.
- [78] S. J. Kim, I. C. Bang, J. Buongiorno and L. W. Hu, "Surface Wettability Change during Pool Boiling of Nanofluids and Its Effect on Critical Heat Flux," *Int. J. Heat Mass Transfer*, vol. 50, no. 19-20, p. 4105–4116, 2007.
- [79] H. Honda, H. Takamatsu and J. J. Wei, "Enhanced Boiling of FC-72 on Silicon Chips with Micro-Pin-Fins and Submicron-Scale Roughness," *J. Heat Transfer*, vol. 124, no. 2, p. 383–390, 2002.
- [80] M. Sesen, W. J. Khudhayer, T. Karabacak and A. Kosar, "A Compact Nanostructure Integrated Pool Boiler for Microscale Cooling Applications," in *ASME Int. Mechanical Engineering Congress & Exposition, IMECE2009–11008*, Orlando, FL, 2009.
- [81] C. Zamfirescu and M. Feidt, "Cascaded Fins for Heat Transfer Enhancement," *Heat Transfer Engineering*, vol. 28, no. 5, pp. 451-459, 2007.
- [82] C. Zamfirescu and A. Bejan, "Constructal Tree-Shaped Two-Phase Flow for Cooling a Surface," *Int. J. of Heat and Mass Transfer*, vol. 46, p. 2785–2797, 2003.
- [83] W. Qu and A. Siu-Ho, "Liquid Single-Phase Flow in an Array of Micro-Pin-Fins," *J. Heat Transfer*, vol. 130, no. 12, pp. 124501-124504, 2008.
- [84] B. Agostini, M. Fabbri, J. E. Park, L. Wojtan, J. R. Thome and B. Michel, "State of the Art of High Heat Flux Cooling Technologies," *Heat Transfer Engineering*, vol. 28, no. 4, pp. 258-281, 2007.
- [85] T. S. O'Donovan and D. B. Murray, "Jet Impingement Heat Transfer - Part 1:

- Analysis of Heat Transfer and Local Velocity Distributions," *International Journal of Heat and Mass Transfer*, vol. 50, pp. 3291-3301, 2007.
- [86] R. Cardenas, P. Mani and V. Narayanan, "Saturated Mini Jet Impingement Boiling," in *Proceedings of ASME 2010 8th International Conference on Nanochannels, Microchannels, and Minichannels, ICNMM2010-30749*, Montreal, Canada, 2010.
- [87] D. Babic, D. B. Murray and A. A. Torrance, "Mist Jet Cooling of Grinding Processes," *Int. J. Mach. Tools Manufact.*, vol. 45, pp. 1171-1177, 2005.
- [88] A. Royne and C. Dey, "Experimental Study of a Jet Impingement Device for Cooling of Photovoltaic Cells Under High Concentration," in *Proceedings of Solar 2004: Life, the Universe and Renewables*, 2004.
- [89] B. Weigand and S. Spring, "Multiple Jet Impingement – A Review," *Int. Symp on Heat Transfer in Gas Turbine Systems*, 2009.
- [90] D. J. Womac, G. Aharoni, S. Ramadhyani and F. P. Incropera, ""Single Phase Liquid Jet Impingement Cooling of Small Heat Sources,"" *Proceedings of the International Heat Transfer Conference*, pp. 149-154, 1990.
- [91] S. V. Garimella and R. A. Rice, "Confined and Submerged Liquid Jet Impingement Heat Transfer," *Journal of Heat Transfer*, vol. 117, pp. 871-877, 1995.
- [92] S. V. Garimella and B. Nenaydykh, "Nozzle-Geometry Effects in Liquid Jet Impingement Heat Transfer," *International Journal of Heat and Mass Transfer*, vol. 39, no. 14, pp. 2915-2923, 1996.
- [93] K. Robbie, G. Beydaghyan, T. Brown, C. Dean, J. Adams and C. Buzea, "Ultrahigh Vacuum Glancing Angle Deposition System for Thin Films with Controlled Three-Dimensional Nanoscale Structure," *Rev. Sci. Instrum.*, vol. 75, no. 4, pp. 1089-1097, 2004.
- [94] T. Karabacak and T.-M. Lu, in *Handbook of Theoretical and Computational Nanotechnology*, M. Rieth and W. Schommers, Eds., Stevenson Ranch, CA, American Scientific Publishers, 2005, p. 729.
- [95] T. Karabacak, G. C. Wang and T.-M. Lu, "Physical Self-Assembly and the Nucleation of 3D Nanostructures by Oblique Angle Deposition," *J. Vac. Sci. Technol. A*, vol. 22, no. 4, pp. 1778-1784, 2004.
- [96] T. McDaniel, W. A. Challener and K. Sendur, "Issues in Heat-Assisted Perpendicular Recording," *IEEE Trans. Mag.*, vol. 39, no. 4, pp. 1972-1979, 2003.
- [97] W. A. Challener, C. Peng, A. V. Itagi, D. Karns, W. Peng, Y. Peng, X. Yang, X. Zhu, N. J. Gokemeijer, Y.-T. Hsia, G. Ju, R. E. Rottmayer, M. A. Seigler and E. C. Gage, "Heat-Assisted Magnetic Recording by a Near-Field Transducer with Efficient Optical Energy Transfer," *Nature Photon.*, vol. 3, pp. 220-224, 2009.
- [98] M. Francoeur and M. P. Menguc, "Role of Fluctuational Electrodynamics Theory in Near-Field Radiative Heat Transfer," *J. Quant. Spectrosc. Radiat. Transfer*, vol. 109, no. 2, pp. 280-293, 2008.
- [99] M. Francoeur, M. P. Menguc and R. Vaillon, "Near-Field Radiative Heat Transfer Enhancement via Surface Phonon-Polaritons Coupling in Thin Films," *Appl. Phys. Lett.*, vol. 93, no. 4, 2008.
- [100] M. Francoeur, M. P. Menguc and R. Vaillon, "Solution of Near-Field Thermal Radiation in One-Dimensional Layered Media using Dyadic Greens Functions and the Scattering Matrix Method," *J. Quant. Spectrosc. Radiat. Transfer*, vol. 110, no. 18, pp. 2002-2018, 2009.
- [101] M. Francoeur, M. P. Menguc and R. Vaillon, "Control of Near-Field Radiative

- Heat Transfer via Surface Phonon–Polariton Coupling in Thin Films," *Applied Physics A*, vol. 103, no. 3, pp. 547-550, 2011.
- [102] K. Sendur and E. Baran, "Near-Field Optical Power Transmission of Dipole Nano-Antennas," *Appl. Phys. B*, vol. 96, no. 2-3, pp. 325-335, 2009.
- [103] K. Sendur and W. Challener, "Near-Field Radiation of Bow-Tie Antennas and Apertures at Optical Frequencies," *J. Microsc.*, vol. 210, no. 3, pp. 279-283, 2003.
- [104] K. Sendur, C. Peng and W. Challener, "Near-Field Radiation from a Ridge Waveguide Transducer in the Vicinity of a Solid Immersion Lens," *Phys. Rev. Lett.*, vol. 94, no. 4, 2005.
- [105] W. Daungthongsuk and S. Wongwises, "A Critical Review of Convective Heat Transfer of Nanofluids," *Renew. Sustain. Energy Rev.*, vol. 11, no. 5, p. 797–817, 2007.
- [106] S. J. Palm, G. Roy and C. T. Nguyen, "Heat Transfer Enhancement with the use of Nanofluids in Radial Flow Cooling Systems Considering Temperature-Dependent Properties," *Applied Thermal Engineering*, vol. 26, no. 17-18, pp. 2209-2218, 2006.
- [107] S. E. B. Ma'ga, C. T. Nguyen, N. Galanis, G. Roy, T. Maré and M. Coqueux, "Heat Transfer Enhancement in Turbulent Tube Flow using Al₂O₃ Nanoparticle Suspension," *Int. J. Num. Methods Heat Fluid Flow*, vol. 16, no. 3, p. 275–292, 2006.
- [108] J. Buongiorno, "Convective Transport in Nanofluids," *J. Heat Transfer*, vol. 128, no. 3, pp. 240-250, 2006.
- [109] S. Kakaç and A. Pramuanjaroenkij, "Review of Convective Heat Transfer Enhancement with Nanofluids," *International Journal of Heat and Mass Transfer*, vol. 52, no. 13-14, p. 3187–3196, 2009.
- [110] S. Liter and M. Kaviany, "Pool-Boiling CHF Enhancement by Modulated Porous-Layer Coating: Theory and Experiment," *Int. J. Heat Mass Transfer*, vol. 44, no. 22, p. 4287–4311, 2001.
- [111] M. Zhang and K. Lian, "Using bulk micromachined structures to enhance pool boiling heat transfer," *Microsystem Technologies*, vol. 14, no. 9-11, pp. 1499-1505, 2007.
- [112] X. Wang and A. S. Mujumdar, "Heat Transfer Characteristics of Nanofluids: A Review," *International Journal of Thermal Sciences*, vol. 46, no. 1, p. 1–19, 2007.
- [113] Y. Xuan and Q. Li, "Heat Transfer Enhancement of Nanofluids," *International Journal of Heat and Fluid Flow*, vol. 21, no. 1, pp. 58-64, 2000.
- [114] H. Kim, J. Kim and M. Kim, "Effect of Nanoparticles on CHF Enhancement in Pool Boiling of Nano-Fluids," *International Journal of Heat and Mass Transfer*, vol. 49, no. 25-26, pp. 5070-5074, 2006.
- [115] A. Bilgin, E. Kurtoğlu, H. C. Erk, M. Sesen, H. F. Yagci-Acar, A. Kubilay and A. Kosar, "Magnetic Nanoparticle Based Nanofluid Actuation with Dynamic Magnetic Fields," in *International Conference on Nanochannels, Microchannels, and Minichannels, ICNMM2011-58222*, Edmonton, Canada, 2011.
- [116] A. Bilgin, E. Kurtoğlu, H. C. Erk, H. F. Yagci-Acar, A. Kubilay and A. Kosar, "A Novel Magnetomechanical Pump to Actuate Ferrofluids in Minichannels," in *Thermal and Materials Nanoscience and Nanotechnology, TMNN-2011/054*, Antalya, Turkey, 2011.
- [117] M. Sesen, S. Ulun, H. C. Su, B. Bahceci, H. F. Yagci-Acar and A. Kosar, "Magnetic Actuation of Nanofluids with Ferromagnetic Particles," in *International Conference on Nanochannels, Microchannels, and Minichannels, ICNMM2010-30728*, Montreal, Canada, 2010.

- [118] E. Kurtoğlu, A. Bilgin, M. Sesen, H. F. Yagci-Acar and A. Kosar, "Implementation of a Simplified Method for Actuation of Ferrofluids," in *3rd Micro and Nano Flows Conference*, Thessaloniki, Greece, 2011.
- [119] L. Mao and H. Koser, "An Integrated MEMS Ferrofluid Pump using Insulated Metal," in *Industrial Electronics Society 31st Annual Conference of IEEE, IECON05*, North Carolina, USA, 2005.
- [120] J. C. Williams Jr., K. C. Saw, R. F. Paterson, E. .. K. Hatt, J. A. McAteer and J. E. Lingeman, "Variability of Renal Stone Fragility in shock wave Lithotripsy," *Urology*, vol. 61, pp. 1092-1096, 2003.
- [121] J. M. Teichman, A. J. Portis, P. P. Cecconi, W. L. Bub, R. C. Endicott, B. Denes, M. S. Pearle and R. V. Clayman, "In vitro Comparison of Shock Wave Lithotripsy Machines," *J. Urol.*, vol. 164, pp. 1259-1264, 2000.
- [122] D. Heimbach, R. Munver, P. Zhong, J. Jacobs, A. Hesse, S. C. Muller and G. M. Preminger, "Acoustic and Mechanical Properties of Artificial Stones in comparison to Natural Kidney Stones," *J. Urol.*, vol. 164, pp. 537-544, 2000.
- [123] R. Bachmann, D. Heimbach, W. Kersjes, D. Jacobs, H. Schild and A. Hesse, "A New Type of Artificial Urinary Calculi: In vitro Study by Spiral CT," *Invest. Radiol.*, vol. 35, pp. 672-675, 2000.
- [124] A. Mota, J. Knap and M. Ortiz, "Three-dimensional Fracture and Fragmentation of Artificial Kidney Stones," *J. Phys. Conf. Ser.*, vol. 46, pp. 299-303, 2006.
- [125] J. A. McAteer, J. C. Williams Jr., R. O. Cleveland, J. V. Cauwelaert, M. R. Bailey, D. A. Lifshitz and A. P. Evan, "Ultracal-30 Gypsum Artificial for Research on the Mechanism of Stone Breakage in Shock Wave Lithotripsy," *J. Urol. Res.*, vol. 33, pp. 429-434, 2005.
- [126] N. C. Pace, F. Vajdos, L. Fee, G. Grimsley and T. Gray, "How to Measure and Predict the Molar Absorption Coefficient of a Protein," *Protein Sci.*, vol. 4, no. 11, pp. 2411-2423, 1995.
- [127] N. J. Greenfield, "Using Circular Dichroism Spectra to Estimate Protein Secondary Structure," *Nat. Protoc.*, vol. 1, no. 6, pp. 2876-2890, 2006.
- [128] G. Bohm, R. Muhr and R. Jaenicke, "Quantitative Analysis of Protein Far UV Circular Dichroism Spectra by Neural Networks," *Protein Eng.*, vol. 5, no. 3, pp. 191-195, 1992.
- [129] G. Deleage and C. Geourjon, "An Interactive Graphic Program for Calculating the Secondary Structure Content of Proteins From Circular Dichroism Spectrum," *Comput. Appl. Biosci.*, vol. 9, no. 2, pp. 197-199, 1993.
- [130] "MalvernZetasizer nano series user manual," MANO 317 Issue 11, Worcestershire: Malvern Instruments Ltd., 2004.
- [131] H. Mach, B. Volkin, C. J. Burke and C. R. Middaugh, "Ultraviolet Absorption Spectroscopy," *Methods. Mol. Biol.*, vol. 40, pp. 91-114, 1995.
- [132] U. K. Laemmli, "Cleavage of Structural Proteins During the Assembly of the Head of Bacteriophage," *Nature*, vol. 227, pp. 680-685, 1970.
- [133] C. Gu and T. Y. Zhang, "Electrochemical Synthesis of Silver Polyhedrons and Dendritic Films with Superhydrophobic Surfaces," *Langmuir*, vol. 24, no. 20, p. 12010-12016, 2008.
- [134] D.-X. Ye, T. Karabacak, R. C. Picu, G.-C. Wang and T.-M. Lu, "Uniform Si Nanostructures Grown by Oblique Angle Deposition with Substrate Swing Rotation," *Nanotechnology*, vol. 16, no. 9, p. 1717-1723, 2005.
- [135] D.-X. Ye, T.-M. Lu and T. Karabacak, "Influence of Nanotips on the

- Hydrophilicity of Metallic Nanorod Surfaces," *Phys. Rev. Lett.*, vol. 100, no. 25, 2008.
- [136] T. Karabacak, J. S. DeLuca, D. Ye, P.-I. Wang, W. G.-C. and L. T.-M., "Low Temperature Melting of Copper Nanorod Arrays," *J. Appl. Phys.*, vol. 99, no. 6, 2006.
- [137] T. Karabacak, P.-I. Wang, G.-C. Wang and T.-M. Lu, "Phase Transformation of Single Crystal β -Tungsten Nanorods at Elevated Temperatures," *Thin Solid Films*, vol. 493, no. 1-2, pp. 293-296, 2005.
- [138] T. Karabacak, P.-I. Wang, G.-C. Wang and T.-M. Lu, "Growth of Single Crystal Tungsten Nanorods by Oblique Angle Sputter Deposition," *Mat. Res. Soc. Symp. Proc.*, vol. 788, p. 75, 2004.
- [139] W. J. Khudhayer, A. U. Shaikh and T. Karabacak, "Platinum Nanorod Arrays with Preferred Morphological and Crystal Properties for Oxygen Reduction Reaction," *Advanced Science Letters*, vol. 4, pp. 1-9, 2011.
- [140] P. Wang, W. Chiu, C. Lee and T. Young, "Synthesis of Iron Oxide/Poly (methyl methacrylate) Composite Latex Particles: Nucleation Mechanism and Morphology," *Journal of Polymer Science: Part A: Polymer Chemistry*, vol. 42, no. 22, p. 5695-5705, 2004.
- [141] S. J. Kline and F. A. McClintock, "Describing Uncertainties in Single-Sample Experiments," in *Mech. Eng. p.3*, 1953.
- [142] L. B. Feril Jr., T. Kondo, Z. Cui, Y. Tabuchi, Q. Zhao, H. Ando, T. Misaki, H. Yoshikawa and S. Umemura, "Apoptosis Induced by the Sonomechanical Effects of Low Intensity Pulsed Ultrasound in a Human Leukemia Cell Line," *Cancer Lett.*, vol. 221, pp. 145-152, 2005.
- [143] D. Gozuacik and A. Kimchi, "Autophagy and Cell Death," *Curr. Topics Dev. Biol.*, vol. 78, pp. 217-245, 2007.
- [144] D. Gozuacik, S. Bialik, T. Raveh, G. Mitou, G. Shohat, H. Sabanay, N. Mizushima, T. Yoshimori and A. Kimchi, "DAP-kinase is a Mediator of Endoplasmic Reticulum Stress-Induced Caspase Activation and Autophagic Cell Death," *Cell Death Differ.*, vol. 15, pp. 1875-1886, 2008.
- [145] A. Bonincontro, E. Bultrini, V. Calandrinib and G. Onorib, "Conformational Changes of Proteins in Aqueous Solution Induced by Temperature in the Pre-Melting Region," *Phys. Chem. Chem. Phys.*, vol. 3, no. 17, pp. 3811-3813, 2001.
- [146] A. S. Parmar and M. Muschol, "Hydration and Hydrodynamic Interactions of Lysozyme: Effects of Chaotropic versus Kosmotropic Ions," *Biophys. J.*, vol. 97, no. 2, pp. 590-598, 2009.
- [147] S. Arai and M. Hirai, "Reversibility and Hierarchy of Thermal Transition of Hen Egg-White Lysozyme Studied by Small-Angle X-Ray Scattering," *Biophys. J.*, vol. 76, no. 4, pp. 2192-2197, 1999.
- [148] A. Oliva, A. F. J. Santovena and M. Llabre's, "Effect of High Shear Rate on Stability of Proteins: Kinetic Study," *J. Pharm. Biomed. Anal.*, vol. 33, no. 2, pp. 145-155, 2003.
- [149] H. Sah, "Stabilization of Proteins Against Methylene Chloride/Water Interface Induced Denaturation and Aggregation," *J. Control. Release.*, vol. 58, no. 2, pp. 143-151, 1999.
- [150] J. L. Schmitke, C. R. Wescott and A. M. Klibanov, "The Mechanistic Dissection of the Plunge in Enzymatic Activity Upon Transition from Water to Anhydrous Solvents," *J. Am. Chem. Soc.*, vol. 118, no. 14, pp. 3360-3365, 1996.

- [151] R. A. S. Hemat, Principles of Orthomolecularism, London: Urotext, 2004.
- [152] L. Ashton, J. Dusting, E. Imomoh, S. Balabani and E. W. Banch, "Shear-Induced Unfolding of Lysozyme Monitored in situ," *Biophys. J.*, vol. 96, no. 10, pp. 4231-4236, 2009.
- [153] W. J. Khudhayer, R. Sharma and T. Karabacak, "Hydrophobic Metallic Nanorods with Teflon Nanopatches," *Nanotechnology*, vol. 20, no. 27, 2009.
- [154] F. P. Incropera and D. P. Dewitt, Fundamentals of Heat and Mass Transfer, 6th ed., Wiley, 2006.
- [155] Y. Fujii and A. M. Nakamura, "Compaction and Fragmentation of Porous Gypsum Targets from Low-Velocity Impacts," *Icarus*, vol. 201, pp. 795-801, 2009.